OPTIMIZING THE FLOW IN A LIQUID SODIUM DYNAMO EXPERIMENT

by

N. Zane Taylor

A dissertation submitted in partial fulfillment of
the requirements for the degree of

Doctor of Philosophy

(Physics)

at the

UNIVERSITY OF WISCONSIN–MADISON

2014

Date of final oral examination: April 21, 2014

The dissertation is approved by the following members of the Final Oral Committee:

Cary Forest, Professor, Physics
Mark Nornberg, Associate Scientist, Physics
Ellen Zweibel, Professor, Astronomy and Physics
Paul Terry, Professor, Physics
John Sarff, Professor, Physics

Abstract

The Madison Dynamo experiment drives a turbulent flow of liquid sodium in a sphere in order to observe a MHD dynamo instability: An exponentially growing magnetic field at the expense of kinetic energy. Initial runs of the experiment observed intermittent bursts of the predicted magnetic mode, but no self-excited field was observed. It was found that turbulent fluctuations were producing large-scale magnetic fields that were a significant fraction of the magnitude of the fields induced by the mean flow. These turbulent-induced fields were solely detrimental, opposing the generation of the magnetic field produced by the mean flow. Baffles and vanes were added to the experiment to optimize the helical pitch of the mean flow and to remove the large-scale detrimental fluctuations. The observed drop in required motor power and a drop in specific measured magnetic response modes gives direct confirmation that these large detrimental eddies have been removed. A probe was developed to characterize the turbulence in the MDE after the baffles were installed and it was determined that the remaining turbulent EMF was mostly acting as an enhanced dissipation to the induced magnetic field. After these modifications, the induced magnetic field produced by the flowing sodium interacting with a seed magnetic field now closely matches laminar predictions. However, no self-excited field has been observed. A velocity inversion technique has been developed that compares internal and external field measurements with a predictive model and determines what the effective mean flow is in the experiment. Results from this velocity inversion give another metric on how optimized the flow profile is and also provide the most robust method of determining how close the experiment is to achieving a dynamo.

ACKNOWLEDGMENTS

There are many people that I would like to acknowledge. First I would like to thank my advisor, Professor Cary Forest for providing me with this opportunity. Without his ingenuity, this experiment, and many others, would not exist. I would also like to thank Roch Kendrick who designed and led the construction of the experiment. Roch tragically passed away early in my graduate career, but I benefitted greatly from Roch's habit of over-engineering everything he put together. The MDE ran incredibly smoothly with no serious breakdowns for years after Roch was gone. I would like to thank Dr. Mark Nornberg who has provided me numerous times with guidance and assistance in my graduate career. I would also like to acknowledge Dr. Erik Spence and Dr. Rob O'Connel for leaving a vast library of code that I used to analyze data and implemented in profile fitting and velocity inversion routines. I would like to thank Elliot Kaplan and Kian Rahbarnia, my fellow grad student and postdoc, for enduring many long data runs lasting into the night. Nick Hahn was an undergraduate student in the engineering department that assisted in creating the CFD geometries used in the FLUENT simulations. Alex Rasmus was a physics undergraduate who put in countless hours helping solder the equatorial hall array and helped with the installation, repair, orienting and maintaining the internal probes. I would like to thank John Wallace for the invaluable engineering support he provided. I would like to thank Mike Clark for his engineering support and turning the baffles I drew up into reality. Finally I would like to thank my family and Cami who provided me with unwavering patience and steadfast support.

TABLE OF CONTENTS

Page

LIST OF TABLES

LIST OF FIGURES

Figure Page

Figure Page

Appendix
Figure

Figure Page

Chapter 1

Introduction

1.1 Source of Magnetic Fields in Nature

The Madison Dynamo Experiment seeks to advance the knowledge of one of the fundamental questions in astrophysics: Where do magnetic fields come from? Many astrophysical bodies observed in nature such as planets, stars and galaxies have magnetic fields. The size and age of these astrophysical bodies (especially planets and stars) eliminates the possibility that the observed magnetic fields are remnants of a primordial field. The observed magnetic fields are produced by magnetohydrodynamic (MHD) dynamos. A dynamo is an instability that converts kinetic energy in a flow to magnetic energy. The dynamo process can be conceptualized by assuming magnetic field lines are frozen into a conductive fluid. When a conductor moves through magnetic field lines, an electromotive force is induced in the conductor which generates currents that cause the magnetic field to be effectively frozen in place in the conductor. An initial seed field applied to a conducting fluid can be amplified by being stretched in the direction of the flow. If the resulting stretched magnetic field is oriented in a certain way, it reinforces the original seed field. If the amplification of the field is sufficient to overcome ohmic losses, then the magnetic field will grow in time.

The earth has a dipolar field that is approximately aligned with the rotation axis, although geological records indicate that the orientation of Earth's field is not constant and flips polarity at irregular intervals. The sun also has a dipolar magnetic field that flips orientation. However, the

sun's dipolar field flips polarity on a very regular 22 year cycle. Flips in the dipole field polarity also correlate to periods of intensified sunspot activity. Therefore, there must be conductive flows in the liquid iron core of the earth and in the electrically conducting plasma of the sun that are conducive to generating and sustaining a magnetic field through a dynamo instability.

Eugene Parker purposed such a flow in a paper published in 1955 [Parker, 1955]. In his paper, Parker presented an $\alpha - \Omega$ dynamo in which differential rotation in the toroidal direction could take an initial, solely poloidally-directed magnetic field and wrap it up in the toroidal direction. This is known as the Ω effect. In addition, that toroidal field in the presence of a helical flow could generate a poloidal field (α effect). It is believed that this is how the dynamo process works in both the earth and the sun. A differentially rotating toroidal flow winds up toroidal field, and then temperature gradients and nuclear decay create convection that causes upwelling flows. The Coriolis force causes these upwelling flows to rotate and become helical. These flows then twist the wound-up toroidal field in the poloidal direction.

1.2 Dynamo Mechanism

Dynamos are magnetohydrodynamic (MHD) instabilities that convert kinetic energy in a flow to magnetic energy. To explain the dynamo process mathematically, we start with Ampere's law, Faraday's law, and Ohm's law in a moving conductor:

$$\nabla \times \mathbf{B} = \mu_0 \mathbf{J} \tag{1.1}$$

$$\nabla \times \mathbf{E} = -\frac{\partial \mathbf{B}}{\partial t} \tag{1.2}$$

$$\mathbf{J} = \sigma(\mathbf{E} + \mathbf{v} \times \mathbf{B}) \tag{1.3}$$

Substituting equation (1.1) and equation (1.2) into the curl of equation (1.3) results in the magnetic induction equation:

$$\frac{\partial \mathbf{B}}{\partial t} = \nabla \times \mathbf{v} \times \mathbf{B} + \frac{1}{\mu_0 \sigma} \nabla^2 \mathbf{B} \tag{1.4}$$

The magnetic induction equation describes the time evolution of a magnetic field in a moving conductor. The second term in the equation is the diffusion term. In the absence of flow, the induction equation reduces to the heat equation and describes how fast the field would decay away. The first term is the advection term. It describes how the flow can interact with the magnetic field to to generate currents. One can imagine that there could exist a flow with the right geometry and with a high enough speed (or low enough resistivity) where the advection term is larger than the diffusion term, resulting in an exponentially growing magnetic field.

1.3 Liquid Metal Dynamo Experiments

In the last few decades, several liquid metal experiments have been constructed to study MHD dynamos in the laboratory. Two experiments that successfully observed a self-excited field were Riga and Karlsruhe. In the Riga experiment, a single impeller drove liquid sodium down a narrow vertical cylinder in a helical flow. The cylinder was nested inside a slightly larger cylinder allowing the flow to exit out the bottom of the inner cylinder return to the top. A stationary volume of sodium sits in secondary outer coaxial cylinder. This experiment observed the generation of self-excited field that matched well with predictions [Gailitis et al., 2000]. The self-excited field was oscillatory and was observed to exponentially grow and saturate. The strength of the saturated field increased with higher rotation rates [Gailitis et al., 2001]. Figure 1.1 shows a schematic of the cylindrical experiment and the measurement of an exponentially growing and saturating self-excited field.

Shortly after the Riga experiment successfully observed a dynamo, the Karlsruhe experiment was also successful [Stieglitz and Mueller, 2000]. In the Karlsruhe experiment, liquid sodium is driven by inductive pumps through a series of pipes with helical baffles all enclosed in a large cylindrical container. The pipes are set up to produce a periodic flow pattern. This type of periodic flow was predicted to produce a growing field [Roberts, 1970]. Shown in Figure 1.2 is a schematic of the Karlsruhe experiment along with a 3-dimentional measurement of the magnetic field at one location. With no field applied (except for the ambient earth field), the helical flow rate was increased until an exponentially growing field was observed at $t = 30$ s.

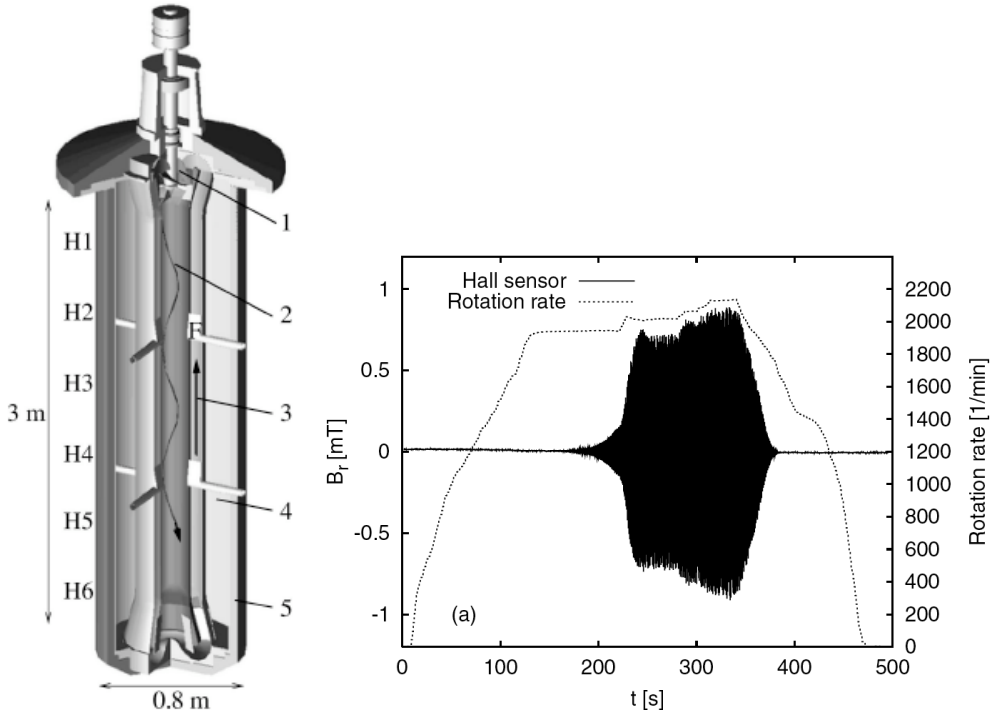

Figure 1.1 (a) The schematic of the Riga dynamo experiment. H1-H7 denote the positions of hall sensors. (b) The measured radial magnetic field from the hall sensor H4 showing self-excitation and saturation when the rotation rate is increased [Gailitis et al., 2001].

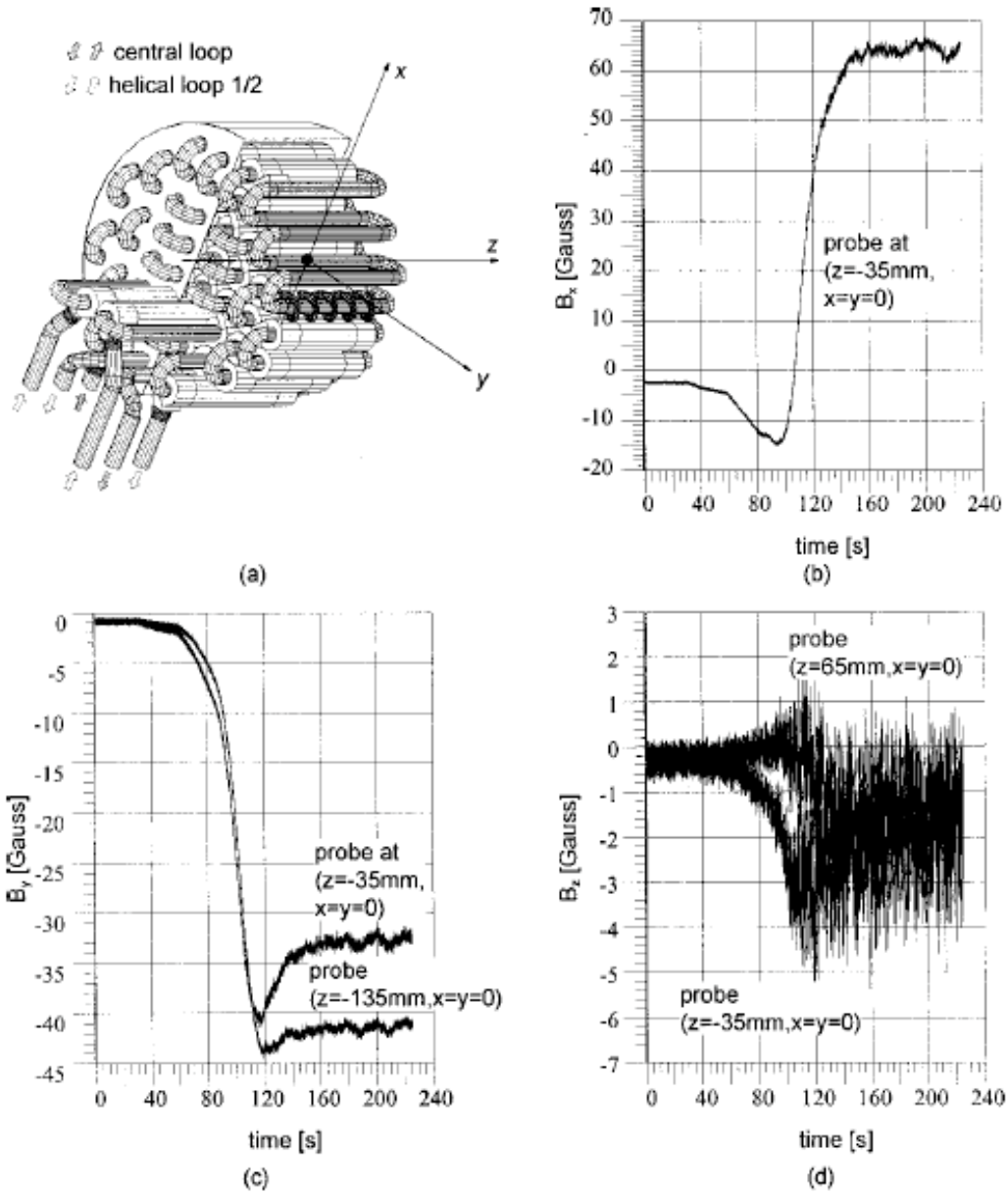

Figure 1.2 (a) Structure of the Karlsruhe dynamo experiment. The helical flow rate in the central loop was increased at $t = 30$ s, and a self excited field was observed by probes located in the inner bore of the experiment. (b) Hall probe measuring $B_x(t)$ (c) Hall probe measuring $B_y(t)$ (d) Hall probe measuring $B_z(t)$ [Stieglitz and Mueller, 2000].

An important take-away from both the Riga and Karlsruhe experiments is that the measured field and onset of the dynamo instability match almost exactly with predictions [Gailitis et al., 2004] [Tilgner, 2002]. Another important point is that both of these experiments impose a scale-separation upon the flow. The flows in both these experiments were highly constrained, forcing the flows to be at a smaller scale than the size of the device. The scale separation minimizes the effect of turbulence. This scale separation also does not accurately reflect flows that produce astrophysical dynamos. Flows in stars and planets occur in an open geometry and with an enormous fluid Reynolds number (Re), where fluctuations make a significant contribution to the generation of system-scale magnetic fields.

After the Riga and Karlsruhe experiments were able to successfully produce an MHD dynamo with constrained essentially laminar flows, a new series of experiments were constructed with more astrophysically relevant open geometries. Included in this next generation of dynamo experiments were the Von Karman Experiment, the Maryland Dynamo Experiment, and the Madison Dynamo Experiment (MDE) [Gailitis et al., 2002]. All of these experiments were built under a similar concept of producing a two-vortex flow of liquid sodium with impellers or disks in an open geometry. This flow profile is predicted to dynamo within experimentally achievable parameters [Dudley and James, 1989] and will be described in greater detail in the next chapter. In these experiments, the lack of constraints, the impeller driving mechanism, and the high fluid Reynolds number (Re) of liquid sodium guaranteed that turbulence would play a much larger role than in the earlier sodium experiments. One question that these experiments sought to address was what role, if any, does turbulence play in governing self-excitation of magnetic fields?

In the initial runs of all three of these experiments, no self-excited dynamo was observed [Nornberg et al., 2006a]. The Maryland Dynamo Experiment, which was very similar in construction to the Madison Dynamo Experiment, was a spherical vessel with a flow driven by two counter-rotating impellers. Maryland observed a highly turbulent response field when their flow was probed with a seed field [Lathrop et al., 2001]. They speculated that the turbulent flow would cause self-excitation in the experiment to be intermittent [Peffley et al., 2000].

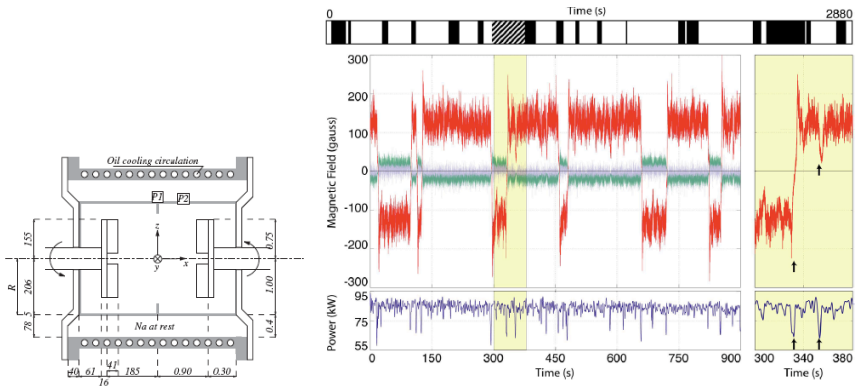

Figure 1.3 (a) A schematic of the Von Karman Sodium experiment. A turbulent flow is driven in the cylindrical vessel by two disks. (b) Non-periodic field reversals were observed when the disks were driven at frequencies F_1=16 Hz, F_2=22 Hz with no applied field, except the ambient earth field. The main component of the self-excited field (red curve) is in the azimuthal direction [Berhanu et al., 2007].

The Von Karman Sodium Experiment (VKS), located at Cadarache, France, is a cylindrical experiment where a two-vortex flow is driven by a pair of disks located at each end of the cylinder. Initial runs of this experiment observed some magnetic field advection, but no self-excited field [Odier et al., 1998]. In later runs of the VKS experiment, the original stainless steel disks were replaced with disks of identical geometry but made of soft iron with a high magnetic permeability. In experiments with the iron disks, a dynamo was observed. [Monchaux et al., 2007]. Experiments were also performed in which the impellers were spun at unbalanced speeds with one hemisphere rotating faster than the other. This flow was also found to dynamo, but interestingly, the direction of the self-excited field flipped in a non-periodic rate [Berhanu et al., 2007] . This is similar to what is observed with the polarity of the Earth's magnetic field. It should be noted that the self-excited magnetic field observed in VKS was directed along the axis of rotation and not perpendicular, as it is predicted by [Dudley and James, 1989]. The role of the ferromagnetic impeller is necessary for the dynamo to be observed in VKS. It is believed that the discontinuity in the magnetic permeability and the presence of turbulent fluctuations on the soft iron disk-sodium interface is the main mechanism driving this axis symmetric dynamo [Giesecke et al., 2010].

1.4 Motivation for the Madison Dynamo Experiment

Although the VKS experiment was able to observe a dynamo in an open geometry, it was only after the addition of soft-iron impellers. The discontinuity in magnetic permeability was required to observe a self-excited field. A dynamo in a simply-connected electrically homogeneous geometry has yet to be demonstrated in a laboratory experiment. As with the VKS and Maryland Dynamo experiments, the Madison Dynamo Experiment produces a turbulent two-vortex flow of liquid sodium. One main question that the MDE sought to answer is what role does MHD turbulence play on determining the threshold for self-excitation? More plainly: is the dynamo enhanced by turbulence, or does it exist in spite of turbulence?

For an MHD dynamo to exist, the flow must have a mechanism for amplification, or stretching, of magnetic field lines. There must also be a mechanism for positive feedback. By twisting and folding the flux tubes back onto themselves, the original field is reinforced. Figure 1.4 shows the predicted growth rate of the magnetic field versus flow speed ($Rm \propto$ flow speed) for a two-vortex flow measured in a water experiment identical in geometry to the MDE. The second figure shows that a dynamo (positive growth rate) is highly sensitive to the pitch of the flow. In order for the two-vortex flow in the MDE to produce a dynamo, it must have the necessary amplification (Rm) and feedback (pitch).

Initial runs of the Madison Dynamo experiment observed a similar result to the Maryland experiment: Intermittent bursts of the expected self-excited mode were observed, but there was very little steady-state field amplification [Nornberg et al., 2006b]. The greater number of diagnostics on the Madison Dynamo experiment allowed for the measurement of the global structure of the response fields. By breaking the response field into spherical modes, it was discovered that the majority of the energy in the response field was mainly dipolar and opposed to the seed field [Spence et al., 2006]. This measured response field was not predicted and could not be explained by the mean flow interacting with the mean field due to the fact it was in violation of Cowlings anti-dynamo theorem [Cowling, 1933]. The turbulent EMF (correlated fluctuations in the velocity and

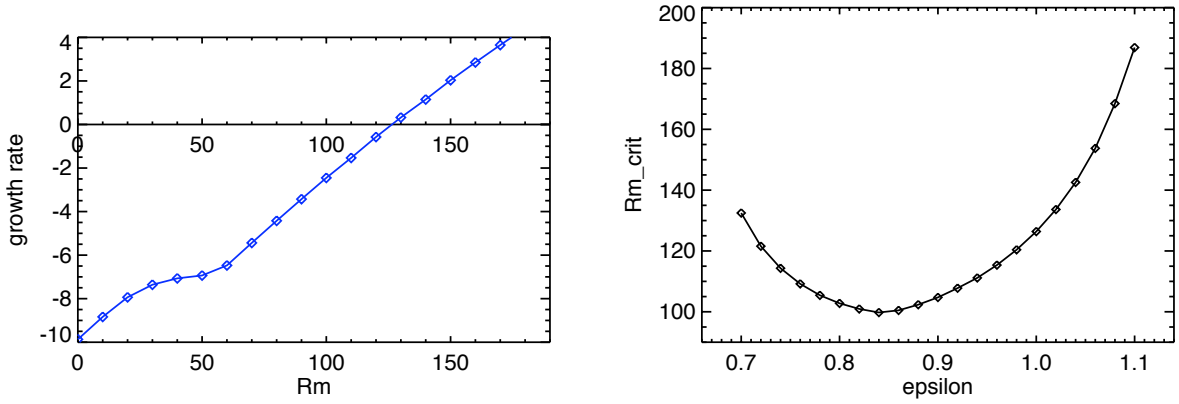

(a) Growth Rate

(b) Critical Rm vs Poloidal Flow Strength

Figure 1.4 (a) The predicted growth rate, in units of $[\tau_\sigma]^{-1}$, of the fasting growing mode for a two vortex flow measured in an identical scale water experiment. τ_σ=$\mu_o \sigma L^2$ is the resistive decay time for the flow. Rm is a dimensionless parameter, which will be defined in the next chapter, related to flow speed. The critical magnetic Reynolds number (Rm_{crit}) is where the growth rate crosses from negative to positive. (b) Rm_{crit} depends on the ratio of poloidal to toroidal flow. Epsilon is a linear adjustment to the amplitude of the poloidal flow.

magnetic field) produced large-scale magnetic fields that were a significant fraction of the magnitude of the fields induced by the mean flow.

By measuring the applied seed field and by getting an approximate measure of the velocity field in an identical scale water experiment, the structure of the turbulent generated fields could be resolved. It was determined that in the Madison Dynamo Experiment, the currents generated by the turbulent EMF generated were producing fields that were solely diamagnetic, opposing the generation of mean magnetic fields in the experiment [Spence et al., 2007].

The first few experimental campaigns of MDE showed that the experiment's open geometry and driving mechanism generated large-scale fluctuations in the flow. With a seed field applied, these turbulent fluctuations produced large-scale magnetic fields that were a significant fraction of the magnitude of the fields induced by the mean flow. The turbulence-induced mean fields were solely detrimental and opposed the generation of the magnetic field produced by the mean flow. Therefore, if a self-excited field is to be observed in the MDE, the dynamo must exist in spite of any turbulence present.

An equatorial baffle was installed in the experiment to modify the flow and remove the largest detrimental fluctuations in the flow. The observed drop in required motor power and a drop in specific measured magnetic response modes gave direct confirmation that these large detrimental eddies had be removed [Kaplan et al., 2011]. A new $\mathbf{V} \times \mathbf{B}$ probe was used to characterize the turbulence in the MDE after the baffle was installed, and it was found that the remaining turbulent EMF was mostly acting as a enhanced dissipation to the induced magnetic field [Rahbarnia, 2012]. The details of these results will be presented in the later chapters of this thesis.

1.5 Thesis Overview

One of the remaining goals of the MDE was to observe a dynamo instability in a turbulent MHD flow. To achieve this goal, modifications to the experiment were performed to reduce the detrimental turbulent fluctuations and to optimize the pitch of the flow. The magnetic diagnostics were upgraded so that when a seed magnetic field was applied the global structure of the induced

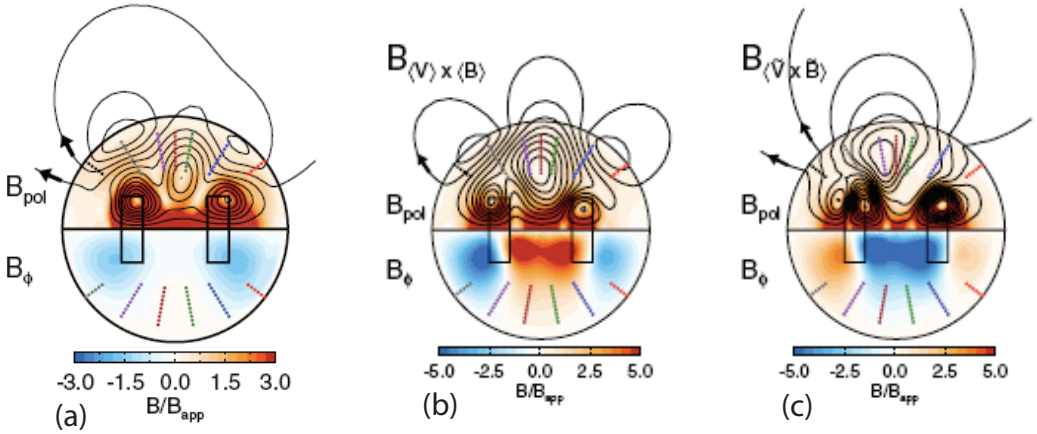

Figure 1.5 (a) The mean magnetic field measured in the Madison Dynamo Experiment. Contours of the toroidal field are shown in the bottom hemisphere and the poloidal field is in the upper hemisphere (contours and field lines). (b) The field that the mean flow in the experiment is predicted to produce. (c) The difference between the measured and predicted magnetic fields is the mean field generated by the turbulent EMF [Spence et al., 2007].

internal magnetic field could be measured. Upgrades in the experiment resulted in a significant amplification of the expected magnetic eigenmode and a corresponding lengthened decay time. Both of these results indicate that the amplification and feedback mechanisms necessary for a dynamo have improved significantly. However, no self-excited field has been observed. Determining how close the flow is to the dynamo threshold is a critical question that is not easily answered. Many MHD dynamo experiments that are in the subcritical regime have difficulty in determining how close to a self-excited field they are.

This thesis demonstrates the metrics used to evaluate different flow configurations, and then, using internal and external field measurements, creates an electrodynamic model that determines what the effective mean flow is in the experiment. Results from this velocity inversion give another metric on how optimized the flow profile is and also provide the most robust method of determining how close the experiment is to achieving a dynamo. The remainder of this thesis is organized as follows:

Chapter 2 establishes the mathematical basis of describing how flows and fields interact in a spherical geometry. A kinematic solver is used to predict the induced fields in the experiment and the critical magnetic Reynolds number required to observe a self-excited field.

Chapter 3 describes the Madison Dynamo Experiment. The key components and operation of the experiment will be discussed, along with the major changes made to optimize the flows. Sections will detail the upgrades made to the magnetic diagnostics, data acquisition, and the series of baffles added to the experiment to optimize the flow.

Chapter 4 will describe the use of a computational fluid dynamics (CFD) code to produce hydrodynamic models of the experiment in order to optimize the flows. The CFD results indicated that the turbulent fluctuations could be reduced and the helicity of the flow modified by the addition of an equatorial baffle and poloidal vanes. Included will be the results from survey of different modeled, measured, and ideal flows and a pitch parameter that shows all two-vortex flows have a consistent optimized pitch.

Chapter 5 will present measurements of the external and internal magnetic fields in the experiment and show the metrics used to determine the performance of the flow. Measured motor power and

the partition of the response external modes into expected and unexpected categories provides a measurement of the turbulence in the flow. The internal and external hall probe arrays are used to reconstruct the internal magnetic fields by fitting the data with spherical harmonics.

Chapter 6 will present efforts to use the measurements of the induced magnetic field to solve for the flows in the experiment through an inversion process. Results from the inversion process allow for the measurement of the flow pitch and to determine how close to self-excitation the flow is.

Chapter 7 will summarize the success of the Madison Dynamo Experiment and discuss future work to be done in laboratory MHD dynamo experiments.

Chapter 2

Kinematic Dynamos

2.1 Magnetic Induction Equation

The purpose of this chapter is to establish the mathematical basis for describing dynamos in a spherical geometry. The magnetic induction equation describes the time evolution of the magnetic field in a flowing conductor. The equation (1.4) can be non-dimensionalised and re-written as:

$$\frac{\partial \mathbf{B}}{\partial \tau} = Rm \nabla \times \mathbf{V} \times \mathbf{B} + \nabla^2 \mathbf{B} \tag{2.1}$$

where $\tau = t/\mu_o \sigma L^2$, $\nabla = L\nabla'$, $V/V' = V_{\max}$, and $Rm = \mu_o \sigma L V_{\max}$. Rm is known as the magnetic Reynolds number. It is a dimensionless number that indicates how efficient the flow is at advecting the magnetic field. Rm is the ratio of advection and dissipation; the two terms in the right hand side of the magnetic induction equation. The larger the magnetic Reynolds number is, the more conducive that flow will be to generating a dynamo.

2.2 Spherical Harmonic Expansion

A convenient way to separate velocity and magnetic fields in a spherical geometry is to split them into toroidal and poloidal harmonics. Due to the properties of magnetic fields ($\nabla \cdot \mathbf{B} = 0$) and because liquid sodium is essentially incompressible ($\nabla \cdot \mathbf{v} = 0$), divergence-free fields can be split into toroidal and poloidal vector fields

$$\mathbf{B} = \mathbf{B}_P + \mathbf{B}_T = \nabla \times \nabla \times (\hat{\mathbf{r}} S) + \nabla \times (\hat{\mathbf{r}} T), \tag{2.2}$$

$$\mathbf{v} = \mathbf{v}_P + \mathbf{v}_T = \nabla \times \nabla \times (\hat{\mathbf{r}} s) + \nabla \times (\hat{\mathbf{r}} t). \tag{2.3}$$

Taking advantage of the spherical geometry, both the toroidal and poloidal functions can be broken into a summation of spherical harmonics with corresponding radial profiles. So, the velocity and magnetic fields can be expressed as

$$\mathbf{B}(r,\theta,\phi) = \nabla\times\nabla\times\sum_{\ell,m} S_l^m(r)Y_l^m(\theta,\phi)\hat{\mathbf{r}} + \nabla\times\sum_{\ell,m} T_l^m(r)Y_l^m(\theta,\phi)\hat{\mathbf{r}}, \tag{2.4}$$

$$\mathbf{v}(r,\theta,\phi) = \nabla\times\nabla\times\sum_{\ell,m} s_l^m(r)Y_l^m(\theta,\phi)\hat{\mathbf{r}} + \nabla\times\sum_{\ell,m} t_l^m(r)Y_l^m(\theta,\phi)\hat{\mathbf{r}}. \tag{2.5}$$

The spherical harmonics are defined as

$$Y_\ell^m(\theta,\phi) = \frac{1}{\sqrt{(1+\delta_{m,0})\pi)}}\sqrt{\frac{2\ell+1}{2}\frac{(\ell-m)!}{(\ell+m)!}}p_\ell^m(\cos\theta)\begin{pmatrix}\sin(m\phi)\\ \cos(m\phi)\end{pmatrix} \tag{2.6}$$

where $p_\ell^m(x)$ is the associated Legendre polynomial. The $1/\sqrt{(1+\delta_{m,0})\pi)}$ is part of the normalization instead of the more standard $1/\sqrt{(2\pi)}$ because of the expansion of the ϕ-component into sines and cosines instead of leaving it as a complex expression.

Evaluating the expansion into spherical harmonics, the magnetic field is given by

$$B_r(r,\theta,\phi) = \sum_\gamma \frac{\ell_\gamma(\ell_\gamma+1)}{r^2}S_\gamma(r)Y_\gamma(\theta,\phi), \tag{2.7}$$

$$B_\theta(r,\theta,\phi) = \sum_\gamma \frac{1}{r}\left(\frac{\partial S_\gamma(r)}{\partial r}\frac{\partial Y_\gamma(\theta,\phi)}{\partial\theta} + \frac{T_\gamma(r)}{\sin(\theta)}\frac{\partial Y_\gamma(\theta,\phi)}{\partial\phi}\right), \tag{2.8}$$

$$B_\phi(r,\theta,\phi) = \sum_\gamma \frac{1}{r}\left(\frac{1}{\sin(\theta)}\frac{\partial S_\gamma(r)}{\partial r}\frac{\partial Y_\gamma(\theta,\phi)}{\partial\phi} - T_\gamma(r)\frac{\partial Y_\gamma(\theta,\phi)}{\partial\theta}\right). \tag{2.9}$$

The velocity field, which will be assumed to be axisymmetric ($m=0$), is given by

$$v_r(r,\theta,\phi) = \sum_\alpha \frac{\ell_\alpha(\ell_\alpha+1)}{r^2}s_\alpha(r)Y_\alpha(\theta,\phi), \tag{2.10}$$

$$v_\theta(r,\theta,\phi) = \sum_\alpha \frac{1}{r}\frac{\partial s_\alpha(r)}{\partial r}\frac{\partial Y_\alpha(\theta,\phi)}{\partial\theta}, \tag{2.11}$$

$$v_\phi(r,\theta,\phi) = -\sum_\alpha \frac{t_\alpha(r)}{r}\frac{\partial Y_\alpha(\theta,\phi)}{\partial\theta}. \tag{2.12}$$

The summation in the expanded velocity and magnetic field shown above is over all valid combinations of ℓ_α, m_α, sine and cosine, for $\ell \geq 0$ and $0 \leq m \leq \ell$.

The expanded magnetic and velocity fields in equation (2.7) and (2.10) can be put back into the magnetic induction equation (2.1). Then, using the orthogonality of spherical harmonics, one can solve for the evolution of individual magnetic modes, yielding

$$\frac{\partial S_\gamma}{\partial t} = \nabla^2_{\ell_\gamma} S_\gamma + \frac{Rm}{r^2} \sum_{\alpha,\beta} [(s_\alpha S_\beta S_\gamma) + (t_\alpha S_\beta S_\gamma) + (s_\alpha T_\beta S_\gamma) + (t_\alpha T_\beta S_\gamma)] \tag{2.13}$$

$$\frac{\partial T_\gamma}{\partial t} = \nabla^2_{\ell_\gamma} T_\gamma + \frac{Rm}{r^2} \sum_{\alpha,\beta} [(s_\alpha S_\beta T_\gamma) + (t_\alpha S_\beta T_\gamma) + (s_\alpha T_\beta T_\gamma) + (t_\alpha T_\beta T_\gamma)] \tag{2.14}$$

where

$$\nabla^2_{\ell_\gamma} = \frac{\partial^2}{\partial r^2} - \frac{\ell_\gamma(\ell_\gamma + 1)}{r^2} \tag{2.15}$$

Again, the summation of α is over all possible combinations of ℓ_α, m_α, sine, and cosine. The first term of equation 2.13 and 2.14 is the dissipation term and the second is the advection term. The individual terms in the advection term with the () brackets containing three profiles represent the interactions between different velocity field modes and seed magnetic field modes to produce a response magnetic field mode. The value of each of these interaction terms depends on the ℓ and m values of α, β, γ and the structure of the radial profiles. It must be noted that (2.13) and (2.14) represent an infinite set of coupled differential equations governing the evolution of $S_\gamma(r)$ and $T_\gamma(r)$. To evaluate these equations, the number of harmonics must be truncated. The three component interaction terms were explored by Bullard and Gellman [Bullard and Gellman, 1954]

and are defined as

$$
\begin{aligned}
(s_\alpha S_\beta S_\gamma) &= \frac{K_{\alpha\beta\gamma}}{N_\gamma}\left[p_\alpha c_\alpha s_\alpha \frac{\partial S_\beta}{\partial r} - p_\beta c_\beta \frac{\partial s_\alpha}{\partial r} S_\beta\right] \\
(s_\alpha S_\beta T_\gamma) &= -\frac{L_{\alpha\beta\gamma}}{N_\gamma}\left[p_\beta\left(\frac{\partial^2 s_\alpha}{\partial r^2} - \frac{2}{r}\frac{\partial s_\alpha}{\partial r}\right)S_\beta - 2\left(c_\gamma \frac{\partial s_\alpha}{\partial r} + \frac{p_\alpha s_\alpha}{r}\right)\frac{\partial S_\beta}{\partial r}\right) + p_\alpha s_\alpha \frac{\partial^2 S_\beta}{\partial r^2}\right] \\
(s_\alpha T_\beta S_\gamma) &= \frac{L_{\alpha\beta\gamma}}{N_\gamma} p_\alpha c_\alpha T_\beta \\
(s_\alpha T_\beta T_\gamma) &= \frac{K_{\alpha\beta\gamma}}{N_\gamma}\left[\left[p_\alpha c_\alpha\left(\frac{\partial s_\alpha}{\partial r} - \frac{2 s_\alpha}{r}\right) + p_\gamma c_\gamma \frac{\partial s_\alpha}{\partial r}\right]T_\beta + p_\alpha c_\alpha s_\alpha \frac{\partial T_\beta}{\partial r}\right] \\
(t_\alpha S_\beta S_\gamma) &= \frac{L_{\alpha\beta\gamma}}{N_\gamma} p_\beta t_\alpha S_\beta \\
(t_\alpha S_\beta T_\gamma) &= -\frac{K_{\alpha\beta\gamma}}{N_\gamma}\left[(p_\gamma c_\gamma + p_\beta c_\beta) t_\alpha \frac{\partial S_\beta}{\partial r} + p_\beta c_\beta\left(\frac{\partial t_\alpha}{\partial r} - \frac{2 t_\alpha}{r}\right)S_\beta\right] \\
(t_\alpha T_\beta S_\gamma) &= 0 \\
(t_\alpha T_\beta T_\gamma) &= \frac{L_{\alpha\beta\gamma}}{N_\gamma} p_\gamma t_\alpha T_\beta
\end{aligned}
$$

where $c_\alpha = (p_\alpha - p_\beta - p_\gamma)/2$ and $N_\alpha = p_\alpha = \ell_\alpha(\ell_\alpha + 1)$. The coefficients $K_{\alpha\beta\gamma}$ and $L_{\alpha\beta\gamma}$ are triple spherical harmonic integrals known as Gaunt and Elsasser integrals respectively. The Gaunt [Gaunt, 1929] integral is given by

$$K_{\alpha\beta\gamma} = \int_0^{2\pi}\int_0^{\pi} Y_\alpha(\theta,\phi) Y_\beta(\theta,\phi) Y_\gamma(\theta,\phi) \sin\theta \mathrm{d}\theta \mathrm{d}\phi \tag{2.16}$$

and the Elsasser [Elsasser, 1946] integrals is given by

$$L_{\alpha\beta\gamma} = \int_0^{2\pi}\int_0^{\pi} Y_\alpha(\theta,\phi)\left(\frac{\partial Y_\beta(\theta,\phi)}{\partial\theta}\frac{\partial Y_\gamma(\theta,\phi)}{\partial\phi} - \frac{\partial Y_\beta(\theta,\phi)}{\partial\phi}\frac{\partial Y_\gamma(\theta,\phi)}{\partial\theta}\right)\sin\theta \mathrm{d}\theta \mathrm{d}\phi. \tag{2.17}$$

There is a set of selection rules that govern which modes can interact with one another. The Gaunt and Elsasser integrals are only non-zero for specific combinations of α, β, and γ(ℓ, m, sine/cosine of each mode). The Gaunt Integrals are non-zero if all of the following requirements are met:

1. $m_\alpha \pm m_\beta \pm m_\gamma = 0$

2. $|\ell_\alpha - \ell_\gamma| \leq \ell_\beta \leq \ell_\alpha + \ell_\gamma$

3. $\ell_\alpha + \ell_\beta + \ell_\gamma$ is even

4. The number of $\cos(m\phi)$ harmonics is odd

The Elsasser Integrals are non-zero if all of the following requirements are met:

1. $m_\alpha \pm m_\beta \pm m_\gamma = 0$

2. $|\ell_\alpha - \ell_\gamma| \leq \ell_\beta \leq \ell_\alpha + \ell_\gamma$

3. $\ell_\alpha + \ell_\beta + \ell_\gamma$ is odd

4. The number of $\cos(m\phi)$ harmonics is even

5. All the harmonics are different

When working with simple flows composed of a few harmonics, the selection rules drastically reduce the number of non-zero interaction terms in equation (2.13) and (2.14).

2.3 Two-Vortex Flows

Dudley and James published a paper in 1989 studying simple flows in a spherical geometry that could generate a dynamo [Dudley and James, 1989]. One of the flows that was predicted to self-excite at the lowest Rm was a t2s2, or two-vortex flow consisting of just one toroidal and one poloidal spherical harmonic with $\ell = 2$, $m = 0$. The radial profiles had the form

$$s_2^0(r) = \epsilon_0 r^2 \sin(\pi r) \tag{2.18}$$

$$t_2^0(r) = r^2 \sin(\pi r). \tag{2.19}$$

Equations (2.18) and (2.19) presented by Dudley and James are in dimensionless units. These profiles are converted to real units so that they can be compared to other profiles presented in this thesis. The poloidal radial profiles are in units of $v \cdot L^2 = m^3/s$ and the toroidal radial profiles are in units of $v \cdot L = m^2/s$. The profiles were normalized with characteristic values of the Madison Dynamo Experiment, where the characteristic velocity is the speed of the tip of the impeller and

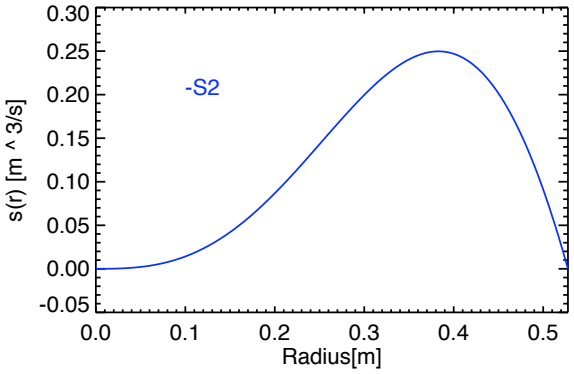

(a) Poloidal Radial Profiles

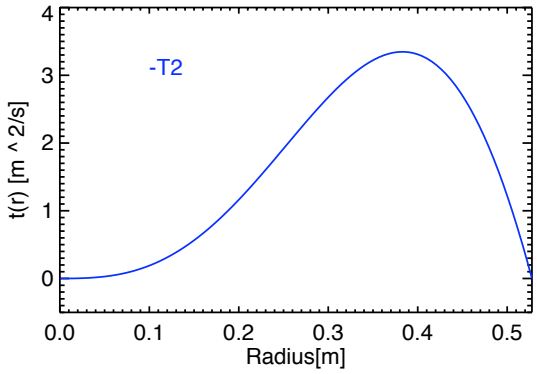

(b) Toroidal Radial Profiles

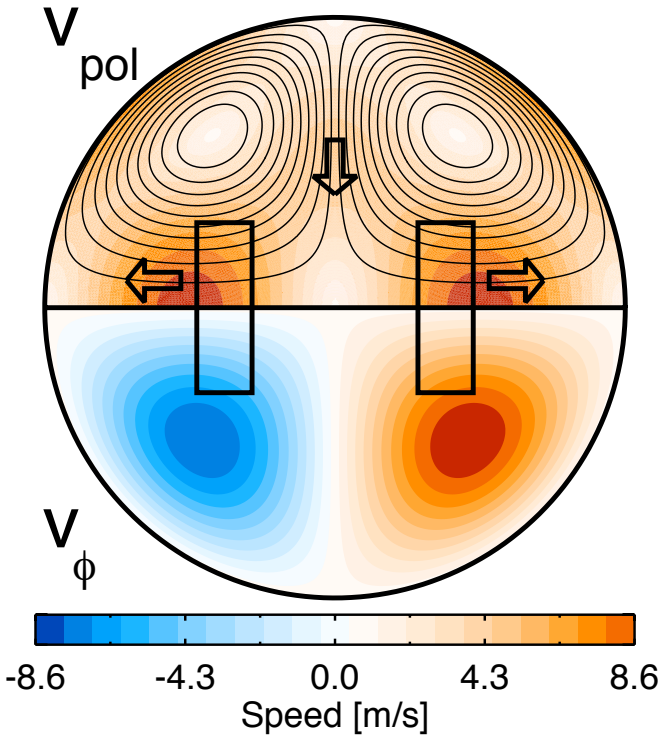

(c) Velocity Contour

Figure 2.1 (a) The poloidal radial profile and (b) the toroidal profile of the Dudley-James t2s2 flow. (c) The corresponding contour plot of the velocity field created by the poloidal (top hemisphere) and toroidal profiles (bottom hemisphere). The profiles were normalized with parameters of the Madison Dynamo Experiment at 1000 RPM.

the characteristic length is the radius of the spherical vessel ($v = v_{tip}$, $L = r_0$). In Figure 2.1 you can see the radial profiles and a contour plot of the velocity field. All flows addressed later in this thesis are presented in the same manner. The axis of rotation is horizontal, with the toroidal flow shown in the bottom hemisphere and the poloidal flow in the top hemisphere. The toroidal flow is directed into the page in one half of the sphere and out of the page on the other. The lines in the poloidal flow are stream lines. The color represents magnitude of the flow and the arrows indicate direction of the poloidal flow. The flow travels outward at the poles and radially inward at the equator. The Madison Dynamo Experiment is a spherical experiment designed to produce this two-vortex flow with impellers. The two rectangular boxes in figure 2.1 indicate the position of the impellers in the experiment, which will be described in Chapter 3.

2.4 Predicting the Induced Field

In the kinematic limit, the magnetic field is too weak to have an effect on the velocity field. Assuming the velocity field is fixed and unchanged by the magnetic field, the magnetic induction equation (2.1) becomes linear in $\mathbf{B}$. By truncating the number of spherical harmonics, the induction equation (Equations (2.13) and (2.14)) becomes a set of coupled linear ordinary differential equations for the poloidal and toroidal magnetic radial profiles.

A linear solver has been developed that can predict the induced field generated by applying a known seed field to a known flow. The magnetic and velocity fields are broken into spherical harmonics with the radial profiles. The radial profiles are discritized into 100 radial points. This allows the magnetic field to be written as a vector made of a set of all S_γ and T_γ evaluated at each radial position ($\mathbf{B} = [S_\gamma, T_\gamma]$). The diffusion and advection terms in equations (2.13) and (2.14) are discretized, becoming matrix operators (A and D) that act on the vector $\mathbf{B}$. The magnetic field vector can be separated into applied and induced magnetic field vectors ($\mathbf{B} = \mathbf{B}_a + \mathbf{B}_i$). The induction equation (1.4) then becomes

$$\frac{\partial \mathbf{B}_a}{\partial t} + \frac{\partial \mathbf{B}_i}{\partial t} = A(\mathbf{B}_a + \mathbf{B}_i) + D\mathbf{B}_i. \tag{2.20}$$

In the above equation, the applied field is assumed to be generated by currents outside the sphere, thus $D\mathbf{B}_a = 0$. Assuming a time-independent solution, the time dependence of the magnetic fields is removed. The terms in the induction equation can be rearranged and the induced field can be solved for

$$\mathbf{B}_i = -[A + D]^{-1} A\mathbf{B}_a. \tag{2.21}$$

The induced field is isolated by performing the matrix inversion using LAPACK linear algebra libraries. Given a known, fixed flow and a seed field, the time-independent induced field can be solved for. Shown in Figure 2.2 are the results from running the predictive kinematic solver with an applied axial dipole field, parallel to the rotation axis, on a modeled t2s2 flow. The toroidal flow interacts with the axially directed dipole seed field by wrapping it up in the toroidal direction where there are strong gradients in the toroidal rotation. This process is known as the Ω-effect. The two-vortex flow generated in the experiment has large gradients in toroidal flow in two separate regions. The first is in between the two impellers rotating in opposite directions, and the second is in the region between the rapidly rotating impeller and the stationary walls. The poloidal flow which is directed outward toward the poles and radially inward at the equator interacts with the seed field by compressing the flux, creating a very strong axially-directed field in the center and voiding the outer regions of magnetic flux.

The internal magnetic diagnostics in the MDE discussed in the next chapter were installed to measure all three of the regions of strong induced field; axial compression and toroidal windup near the center and the toroidal windup on the outside near the poles.

2.5 Predicting the Growth Rate

A kinematic eigenvalue solver has been developed to determine the growth rate the magnetic field with a fixed velocity profile for varying values of Rm. Assuming the magnetic field has the form of

$$\mathbf{B}(\mathbf{r}, t) = \sum_i \mathbf{B}_i(\mathbf{r}) e^{\lambda_i t}, \tag{2.22}$$

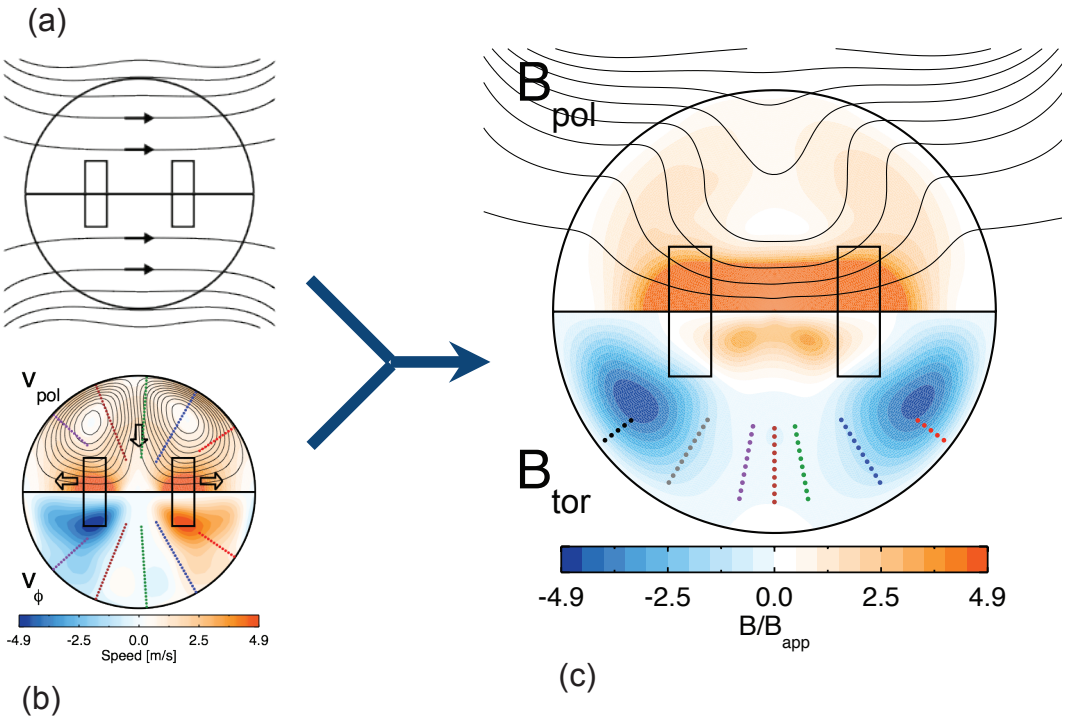

Figure 2.2 (a) The field lines for an applied axial dipole field. (b) A two-vortex flow profile that creates the advection matrix in the kinematic solver. (c) The results from the kinematic solver: the predicted steady-state field generated by the seed field interacting with the flow. The poloidal field is shown in the top hemisphere the toroidal field is shown in the bottom hemisphere.

the induction equation can then be written as an eigenvalue equation,

$$\lambda_i \mathbf{B}_i(\mathbf{r}) = Rm \nabla \times \mathbf{v} \times \mathbf{B}_i(\mathbf{r}) + \mathbf{B}_i(\mathbf{r}). \tag{2.23}$$

The dynamo problem has been simplified to finding a velocity profile ($\mathbf{v}$) for which $\lambda > 0$ for the lowest value of Rm. The discretization of radial profiles and the advection and diffusion operators described in the previous section can be implemented here. Equation (2.23) then becomes

$$\lambda \mathbf{B} = [A + D]\mathbf{B}. \tag{2.24}$$

This linear equation is solved using the linear algebra ARPACK eigenvalue solver. The eigenvalue solver searches to find the magnetic mode (eigenvector) that has the largest growth rate (eigenvalue). The magnetic Reynolds number can be ramped up in the advection matrix until a growing magnetic field is expected (a positive eigenvalue is returned). The point at which a growing field is first observed is the critical magnetic Reynolds number (Rm_{crit}). Analyzing the Dudley-James flow, the solver has good agreement with the predicted Rm_{crit}=50 reported by [Dudley and James, 1989]. The magnetic eigenmode generated by the t2s2 flow is predominately a transverse dipole outside the experiment (S_1^1). There is no preferred orientation in the ϕ-direction, so S_1^{1c} or S_1^{1s}, or a combination of the two, is the excited mode. This solver and its results have been reported by [Forest et al., 2002] and [O'Connell et al., 2000].

Figure 2.3 shows the results of the eigenvalue solver when applied to the Dudley-James flow. As Rm is increased, the transverse dipole mode is less damped until $Rm = Rm_{crit} = 50$ when the mode's growth rate becomes positive. Also shown in Figure 2.3 is that the ratio of poloidal to toroidal flow has a significant impact on the dynamo threshold. By multiplying the poloidal flow by ε, the strength of the poloidal flow can be increased or decreased with respect to the toroidal flow, but the shapes of the radial profiles remain fixed. Running the eigenvalue solver multiple times with the amplitude of the poloidal flow modified reveals that Rm_{crit} is very sensitive to the ratio of poloidal to toroidal flow. This effect indicates that the feedback mechanism that is necessary for a dynamo is heavily dependent on the helical pitch of the flow. Quantifying this pitch and determining the optimal ratio was done by surveying many different two-vortex flows, and the results are shown in section 4.5.

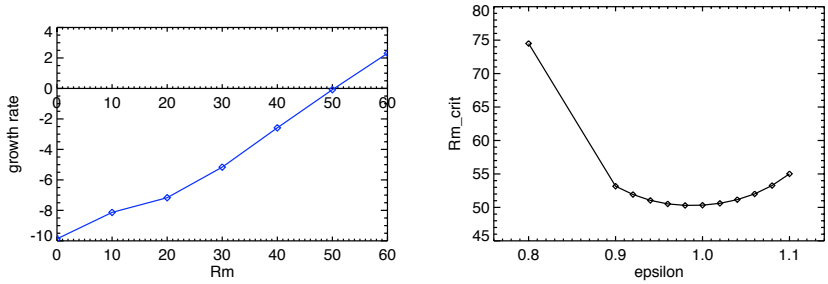

(a) Growth rate (b) Critical Rm vs poloidal flow strength

Figure 2.3 (a) The predicted growth rate, in units of $[\tau_\sigma]^{-1}$, of the fasting growing (least damped) mode for the Dudley-James flow. τ_σ=$\mu_o \sigma L^2$ is the resistive decay time for the flow. Where the growth rate crosses from negative to positive is the critical magnetic reynolds number (Rm_{crit}). (b) Rm_{crit} depends on the ratio of poloidal to toroidal flow. Epsilon is a linear modification of the poloidal profile.

2.6 Role of Turbulence

The predicted induced magnetic fields and growth rates shown in this chapter were computed assuming a laminar flow. Initial runs of the Madison Dynamo Experiment found that large-scale fluctuations played a large and detrimental role in the generation of magnetic flux. The standard way of addressing the role of turbulence is through mean field theory [Krause and Rädler, 1980]. In this analysis, the velocity and magnetic fields are separated into mean and fluctuation components

$$\mathbf{B} = \langle \mathbf{B} \rangle + \tilde{\mathbf{b}}, \tag{2.25}$$

$$\mathbf{v} = \langle \mathbf{v} \rangle + \tilde{\mathbf{v}}. \tag{2.26}$$

Substituting equation (2.25) and (2.26) into equation (1.4) and then averaging, we find the time evolution for the mean magnetic field,

$$\frac{\partial \langle \mathbf{B} \rangle}{\partial t} = R_m \nabla \times \left[\langle \mathbf{v} \rangle \times \langle \mathbf{B} \rangle + \varepsilon \right] + \nabla^2 \langle \mathbf{B} \rangle, \tag{2.27}$$

where ε=$\langle \tilde{\mathbf{v}} \times \tilde{\mathbf{b}} \rangle$ is the turbulent electromotive force (EMF). Correlated fluctuations in the velocity and magnetic field can interact to generate currents that create mean magnetic fields.

Assuming that the turbulence is isotropic, and assuming scale separation between the mean fields and fluctuations, the applied first-order smoothing results in the turbulent EMF

$$\varepsilon = \langle \tilde{\mathbf{v}} \times \tilde{\mathbf{b}} \rangle = \alpha \langle \mathbf{B} \rangle + \beta \nabla \times \langle \mathbf{B} \rangle + \cdots, \tag{2.28}$$

where α and β are defined by [Krause and Radler, 1980, Sec. 3.7] as

$$\alpha = -\frac{1}{3} \int \langle \tilde{\mathbf{v}}(\mathbf{r}, t) \cdot \nabla \times \tilde{\mathbf{v}}(\mathbf{r}, t - \tau) \rangle \mathrm{d}\tau, \tag{2.29}$$

$$\beta = \frac{1}{3} \int \langle \tilde{\mathbf{v}}(\mathbf{r}, t) \cdot \tilde{\mathbf{v}}(\mathbf{r}, t - \tau) \rangle \mathrm{d}\tau. \tag{2.30}$$

The α-effect is related to kinetic helicity and generates currents that are parallel to the mean magnetic field. The α-effect generated currents produce a magnetic field perpendicular to the mean magnetic field. In conductive astrophysical bodies, differential rotation can create a toroidal magnetic field (Ω-effect). Correlated helical fluctuations can take that initial toroidal field and

generate a poloidal field through the α-effect. The β-effect is related to the amount of energy in the turbulent flow. The β-effect generates currents that are perpendicular to the mean magnetic field and anti-parallel to the mean current (that generates the magnetic field). Thus, the β-effect acts as an enhancement to the resistivity. The increased dissipation due to the β-effect reduces the ability of the flow to advect the field. The effective magnetic Reynolds number is reduced to $Rm_{\text{eff}} = \mu_o \sigma_{\text{eff}} L V_{max}$ where $\sigma_{\text{eff}} = \sigma/(1 + \mu_o \sigma \beta)$.

Although the turbulent EMF (α-effect) is a necessary component in the astrophysical dynamo models, in the Madison Dynamo Experiment, it has been found that the turbulent EMF plays a solely detrimental role. The modifications made to the experiment were done to characterize and reduce the turbulence.

Chapter 3

Madison Dynamo Experiment

3.1 Description of the Sodium Dynamo Experiment

The Madison Dynamo Experiment is a roughly 1-meter (42 inches) diameter stainless steel sphere. The walls of the vessel are 5/8 inches thick. The two-vortex flow of liquid sodium is generated by two counter-rotating impellers. These impellers are identical, stainless steel, square-pitched boat propellers which have been modified to generate a velocity field approximating the ideal Dudley-James flow [Dudley and James, 1989]. The radii of the impellers were reduced to 6 inches and a Kört nozzle (a 4 inch wide ring) was welded to the impellers' outer edge. The Kört nozzle removes the radial thrust generated by an unmodified impeller. Three 1/2 inch rectangle bars were added to the outer edge of each Kört nozzle to increase the amount of toroidal flow generated. Both impellers are attached to a shaft entering the vessel through ports at the poles. On these ports there is a complicated, multi-layer seal assembly that the shaft must pass through. Behind the first seal is an oil reservoir filled with hydro-cracked mineral oil. The oil is pressurized 30 PSI above the pressure of the sodium in the vessel, so that a failure in the first mechanical seal the oil will flow into the vessel instead of sodium getting into the seal body. Behind the oil reservoir is a second mechanical seal, and behind that is a volume supplied with a flow of argon gas. Should sodium leak through both mechanical seals, the flow of argon gas would stop and the build up of pressure in the argon line would indicate a seal failure.

The shafts are spun by 75 kW motors with a maximum rotation rate of 1780 RPM. A 21-inch torque tube connects the impeller shaft to the motor. This allows for a maximum misalignment of 0.052" in the total indicator reading runout. Each motor is powered by a variable frequency drive

(VFD). These VFD's record the motors' torque and power information. At high rotation rates, the sphere is pressurized up to 80 PSI to prevent cavitation. Cavitation is the creation of gas bubbles in the low pressure region behind the rapidly rotating blades. These bubbles collapse on the impellers surface and can cause damage to the impellers and reduce the momentum transferred to the flow.

3.2 Operating the Sodium Experiment

When the experiment is not in use, all of the sodium (roughly 275 gallons) is stored in a holding tank. The holding tank is located in a steel-lined vault below the floor level of the lab. The holding tank was set up so that the sphere could be gravity drained in case of a power outage or other failure during a run. The holding tank also allows for the sphere to be open up and modifications made in-between experimental campaigns. The holding tank is electrically heated by 240 Volt Calrod heaters and insulated with mineral wool that keep the sodium liquid at 120 degrees.

The freezing point of sodium is 98 degrees Celsius. For the experiment to operate, the vessel must be heated from room temperature up to 120 degrees. The heat up process takes approximately 5 hours. The slow heat up rate is done to avoid stress caused by thermal expansion that could be present due to the low thermal conductivity of stainless steel.

Three different oil systems must be running before and during operating the experiment. The first is the bearing lubrication oil system. The two bearings located inside the shaft-seal assemblies are heated and lubricated with royal purple oil heated to 60 degrees. A single pump and chiller circulate the oil to all four bearings.

The second oil system is for the heating and cycling of the hydro-cracked oil in the seal assemblies. The seal body is heated up to 120 degrees and maintained at that temperature when the experiment is in operation. Each seal has its own oil reservoir that is heated with a 3 kW heater. The oil is circulated with a pump and cooled with an oil-air heat exchanger.

The third oil system is for the vessel heating and cooling. The motors dump up to 150 kW of power into the sodium when the experiment is operating at the maximum rotation rate. This energy is dissipated in the sodium, causing it to heat up. This heat must be removed from the flow to optimize the conductivity of the sodium ($R_m \propto \sigma \propto 1/T$). In addition, excessive heating could

damage the Hall sensors that are rated to 150 degrees. Finally, liquid sodium is more volatile at higher temperatures. A sodium leak at high temperature would be more dangerous than a leak close to the freezing point. Copper wedge-shaped plates have been glued to the surface of the sphere using a heat-transfer putty. Heat transfer oil is pumped through winding copper tubing that has been soldered to the plates. Most of the sphere's heating system oil is stored in a large reservoir. The oil is heated with a 12 kW heater and cooled with a 75 kW oil-water heat exchanger located just outside the lab. A three-way mixing valve sends oil to the oil-water heat exchanger or out to the manifolds that distribute the oil to the copper plates on the sphere's surface. The heater and a three-way mixing valve are controlled by a PID controller, based on a thermocouple temperature measurement on the surface of the sphere. The entire surface of the sphere along with the oil manifolds and oil lines are covered with insulation to prevent ambient heat loss.

In addition to the oil systems, there are several electrical heaters for different components of the experiment. Calrod heaters strapped to the outside of the 16-inch flange necks where the seal assemblies mount to the sphere. Calrod heaters also heat the sodium transfer lines that connect the holding tank to the 2-inch port at the bottom of the sphere. Another Calrod heated component is the large pneumatic sodium valve located on the transfer line that connects the holding tank to the sphere.

Sodium is transferred from the holding tank to the sphere using pressurized argon. As the holding tank is pressurized, the sodium is forced through a long dip tube opening near the bottom of the tank up through the transfer line and sodium valve into the bottom of the sphere. Once the entire sphere is filled, the sodium continues filling through a 2-inch port at the top of the sphere. This 2-inch port leads to expansion lines that lead to the expansion tank. A vent is opened near the top of the expansion tank during the fill process to allow for the displaced gas to escape. Four load cells monitor the weight of the holding tank. By keeping track of the reduction of strain on the load cells, the amount of sodium in the vessel can be approximated during a sodium transfer. Electrical contact switches allow for the direct confirmation of the sodium level when filling the experiment. These switches are single leads held at 24 VDC. When the sodium comes in contact with the lead, the voltage is shorted to ground indicating the presence of sodium at that

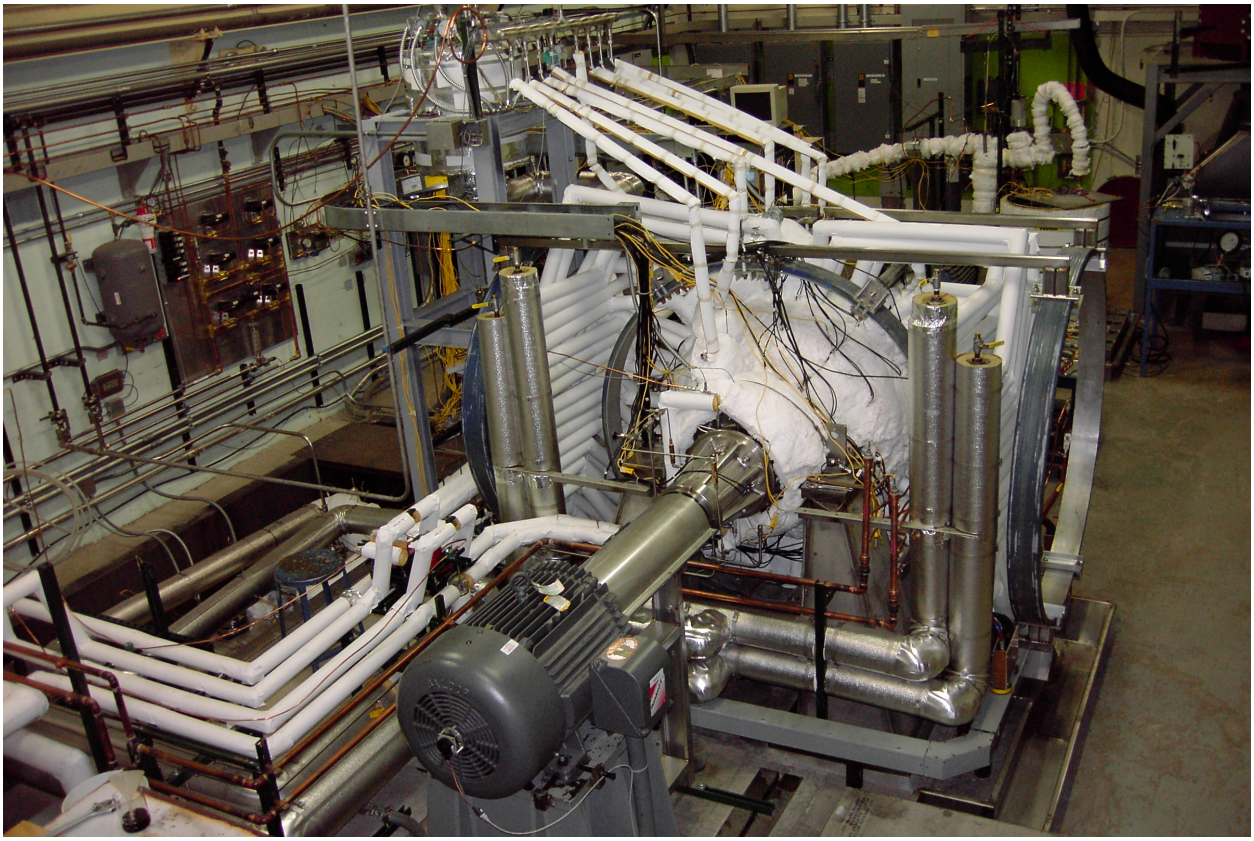

Figure 3.1 Picture of the Madison dynamo experiment from 2006 before hole drilling for baffle installation took place.

height. Three electrical contact switches, at different heights, are located in the expansion tank and another three are in the holding tank. Once the expansion tank is filled halfway with sodium, the sodium valve and vent are closed and the transfer is complete. The expansion tank is partially filled intentionally to accommodate the thermal expansion and contraction of the sodium due to variations in temperature.

The sodium experiment is controlled by Lookout, a software program by National Instruments. Lookout interfaces with National Instruments Fieldpoint input/output modules as well as control cards. The FieldPoint modules monitor temperatures and pressures, actuate valves, and perform other monitoring and control tasks. The Lookout program also communicates with the VFDs setting the rotation rates and starting and stopping the motors. The more advanced settings such as rampup time and rotation direction must be programed in the VFD directly. A more detailed description of the Experiments construction and operation can be found in theses by M.D. Nornberg [Nornberg, 2006] and E.J. Spence [Spence, 2006].

3.3 Applied Fields

The flowing sodium in the vessel is probed with two sets of coils. One pair is aligned along the motor axis and the other pair are perpendicular. The axial coils can be used to produce a dipole (ℓ=1, m=0) or a quadrupole (ℓ=2, m=0) field. The transverse set of coils can be used to produce a transverse dipole (ℓ=1, m=1) or a transverse quadrupole (ℓ=2, m=1) field. The axial set is powered by a single DC power supply and can provide up to 600 Amps (≈ 150 Gauss on axis). The transverse set is powered by two DC power supplies in series and can provide up to 920 Amps ($\approx \ 60$ Gauss on equator). The transverse set is located further away from the sphere, thus the lower field.

Both the axial and transverse power supplies are hooked up to an H-bridge that can switch the applied current to generate programmable waveforms in the coils. In this work, the H-bridges were used to apply square wave forms to measure the rate of decay of the induced field in the sodium. For a more detailed description of the H-bridge construction and control, see the thesis by E.J.

Kaplan [Kaplan, 2012]. The coils are water cooled by closed loop system with the chiller located outside the lab.

3.4 Hall Probes and Data Acquisition

The most used diagnostic on the experiment are Hall sensors which measure the magnetic field. There are 74 one-dimensional Hall probes on the outside of the sphere. There are also arrays consisting of 10 three-dimensional Hall probes that each sit in thermal wells immersed in the sodium and measure the internal field.

3.4.1 External Hall Probes

The external Hall probes are built with a single direction Hall effect sensor (Analog Devices AD22151). The sensor is mounted on an integrated circuit board with the appropriate resistors and capacitors. The value of the resistors and the capacitor set the temperature compensation, magnetic field sensitivity, and the low pass filter frequency. These Hall probes require 5 VDC and return a signal between 0 V and 5 V depending on the magnetic field. The range of the external Hall probes is -180 Gauss to +180 Gauss.

The Hall probe circuit board is mounted to two 0.5 inch plastic standoffs which are mounted to a 1.75 inch diameter stainless steel disk with brass screws. The disk is placed on a stainless steel ring with the same diameter. A 0.25 inch stud is welded to the sphere at the location for each Hall probe. A 0.25 inch mounting hole in the disk allows for the stud to pass through the ring and for the ring and disk to be tightened to the sphere's surface with a nut. The steel ring pressed on the spherical vessel surface forces the Hall array mounted on the steel disk to be perpendicular to the vessel wall measuring purely radial magnetic fields. Two BNC feed-throughs also pass through the steel disk. Two coaxial cables are connected to these BNC feed-throughs. One coaxial cable supplies the probe with 5 VDC while the other coaxial cable provides ground and returns the Hall probe output signal back to the data acquisition.

The external Hall probes were calibrated on a bench before being installed on the sphere. The probe being calibrated was mounted on its stainless steel disk and ring and bolted to a plastic

cylinder. This plastic cylinder slides into a 10.5 inch long, 2.5 inch diameter solenoid, consisting of three layers of fine magnetic wire. The probe was positioned to measure the z-component of the solenoid's magnetic field. The output of the probe is digitized along with the current (magnetic field) in the solenoid. The calibration curves were created from this data.

3.4.2 Internal Hall Probes

The internal Hall probe arrays consist of the same single direction Hall effect sensor used in the external probes (Analog Devices AD22151) and a two-direction Hall effect sensor (Sentron 2SA-10). The top side of the Hall array circuit board is essentially the single external board repeated 10 times. The two axis Hall sensors have all of their temperature compensation and magnetic sensitivity contained internally in the chip. There is no low pass filtering on the two-axis Hall sensors. The bottom half of the Hall array circuit board contains the two-axis chip plus additional holes for the output signals to be measured. All of the sensors on one array board (20 total) receive 5 VDC and ground on common rails on the board.

Both the single and two axis sensors in the internal arrays require 5 VDC and return a signal between 0 V and 5 V depending on the magnetic field. The range for the single axis Hall probes is -180 Gauss to +180 Gauss except for the 10 closest to the center of the vessel in the equatorial array. Those sensors had their corresponding resistors changed to reduce the magnetic sensitivity to make the measurement range be -1000 Gauss to +1000 Gauss. The measurement range for the 2 axis sensors in both directions is -500 Gauss to +500 Gauss.

Four 2-inch ports were drilled on the sphere at the equator, another six were drilled at different theta coordinates at one toroidal position. Each of these ports are terminated with a Grayloc flange. Mating with that Grayloc flange are custom machined Grayloc endcaps with a female Swagelok connector welded to them. Dip tubes, or 0.75 inch stainless steel tubes open on one end and closed on the other, have a mating Swagelok connector swaged on near the open end. The dip tubes are inserted through this swage connection and tightened in place. When the vessel is filled, the outside of the dip tube is in contact with the sodium but the inside of the tube to be open to the air in the lab. This creates a hot, but safe environment for the internal Hall arrays. The depth of the

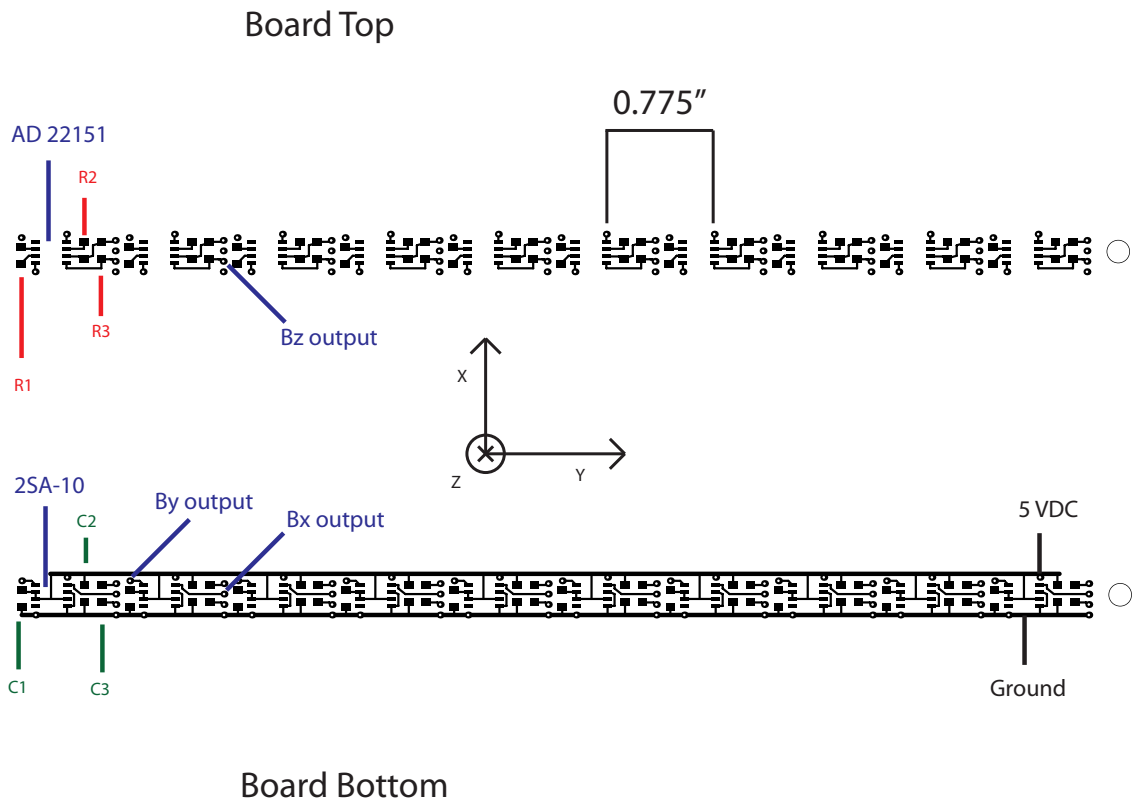

Figure 3.2 This is a schematic of the board for the 3D Hall arrays in the experiment. The boards are oriented in the sphere so that $B_x = B_\phi$, $B_y = B_r$, and $B_z = B_\theta$. The values of the resistors and capacitors are; R1=$15k\Omega$, R2=$3.3k\Omega$, R3=$100k\Omega$, C1=C2=$0.10\mu F$, and C3=$3.3nF$.

dip tubes depends upon their location. The tubes closest to the poles only extend about 5 inches into the sodium due to the presence of the impellers. The tubes further away from the poles extend about 10 inches into the sodium. Unlike the other internal arrays in the dip tubes, the equatorial array consists of four of the 10 chip boards daisy chained together. Three small, U-shaped, high temperature plastic pieces were machined to connect four of the 10 chip boards together to make the equatorial array. Each 10 chip array requires 5 VDC and ground and has 30 output signals (3 directions x 10 positions). There are 32 small magnet wires soldered to holes in each array board making these connections. The 32 small magnet wires for each array are bundled together into high temperature teflon tubing which goes from the end of the array, out the open end of the dip tubes, and up to breakout boxes mounted just above the experiment. The 30 outputs from the Hall arrays go to a 37-pin connector, and a D-sub 37 pin shielded cable takes the signals from the breakout box to the data acquisition computer. The 5 VDC and ground that power each of the arrays is not transmitted on the 37 cables, a separate coaxial cable carries these to a BNC connection in each breakout box that goes to the array.

The three-dimensional arrays were aligned using the applied axial field. The arrays are oriented so that the single-axis Hall sensors measure the θ-directed field (axial field for the equatorial probe) and the two axis Hall sensors measure the radial and phi-directed field (B_r, B_ϕ). The internal Hall probe arrays would be more difficult to calibrate on the bench so instead they were installed in the experiment and calibrated *in situ*. Four different field configurations were applied to an empty sphere with the internal probes installed. By measuring the current in the field coils, the applied field at all the probe locations is known. The output of the Hall probes is logged along with the strength of the magnetic field to give the calibration curves. The four field configurations allows for the exact direction of each of the probes to be determined along with the calibration curves.

Since the dip tubes are fixed at one end, they are prone to vibrate at higher rotation rates. The vibrations become alarming around 1000 rpm. For this reason, all of the longer dip tubes were removed for campaigns with high rotation rates. The equatorial tube fixed at both ends does not vibrate as much as the long dip tubes, but still does suffer some vibrations. The equatorial array contains 120 small magnetic wires solder connections and lacks the 0.5 inch casing of the single

arrays. For these reasons, the occasional probe loss is observed when rotating at high speeds. The appropriate steps are taken in the data analysis to identify and remove bad or questionable probes. Fortunately the structure of the equatorial magnetic field can still be determined with dense probe coverage in the internal array.

3.4.3 $\mathbf{V} \times \mathbf{B}$ Probe

A new diagnostic was built and installed in the machine to measure the potential produced by flow when interacting with a local magnetic field. The purpose of this diagnostic was to make a direct local measurement of the turbulent EMF in the sodium [Rahbarnia, 2012]. The probe is a 0.75 inch stainless steel tube that fits into the same Swageloc ports used for the internal Hall probe arrays. Contained in the tube are two small permanent magnets, one pointed radially and the other perpendicular to that in the theta direction. There 3 sets of electrodes separated by a few milimeters that measure the potential difference in the sodium. Two sets (4 electrodes) are on the bottom of the sphere measuring v_θ and v_ϕ crossed with the permanent b_r magnet. The third set of electrodes is on the side of the tube measuring v_r crossed with the permanent b_θ magnet. Just behind the permanent magnets in the tube is a single 3-D Hall probe that can make a local measurement of the total B field in that region. Therefore, this probe can provide measurement of the mean $\langle \mathbf{V} \rangle \times \langle \mathbf{B} \rangle$ and also the $\tilde{\mathbf{v}} \times \tilde{\mathbf{b}}$.

3.4.4 Data Acquisition System

The signals from the external Hall probes are transmitted through coaxial cables while the internal signals are transmitted through D-sub 37 pin cables. All of the signal cables travel through cable trays above the experiment to the data acquisition rack next to the experiment. In the rack all of the signals terminate into large breakout boxes which contain 68 pin breakout boards. The signals, partitioned into these 68-pin boards, go to five National Instruments M Series PCI-6225 16-bit digitizers on PCI-based data acquisition cards located in the data acquisition computer. Each card has a 80 analog inputs and a single analog to digital converter with a maximum sample rate of 250 kHz. The sample clock on the first acquisition card is routed to the other four cards on an

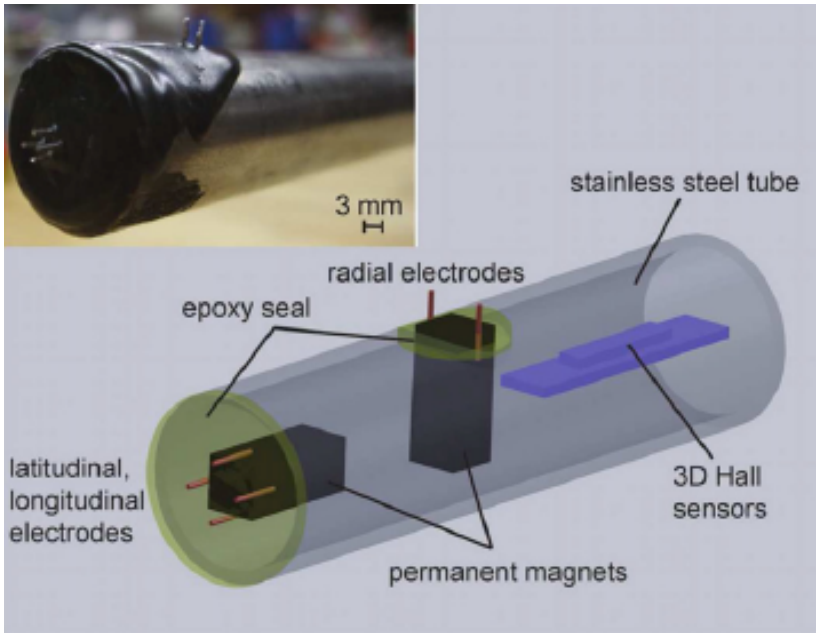

Figure 3.3 A picture of the VxB probe before being installed in the experiment and a schematic showing the components of the probe. Two permanent magnets and 3 sets of electrodes allow the probe to measure three components of the flow. The Hall probe measures all three components of the magnetic field. This allows for the direct measurement of the turbulent EMF.

internal bus so that the samples are synchronized. The data Hall probe data is sampled at a rate of 512 Hz. This sampling frequency is sufficient to resolve the fluctuations well past the noise floor in the Hall probes. After the data collection is complete a separate IDL routine is run that reads in the raw voltage data from the dataset and uses the calibration curves for all the the Hall probes to convert the voltage to magnetic field. The analysis of these signals will be discussed in detail in Chapter 5.

The data acquisition computer, data breakout boxes, and the rack they are mounted on are on a separate ground line that runs to the main grounding pole in the lab. To prevent ground loops which can cause noise to be picked up in the data, all of the external and internal Hall probes are also on data acquisition ground and are electrically isolated from the rest of the experiment. The ground can for the entire data acquisition system can be disconnected by a single knife switch to check for ground loops. A ground loop check is performed at the beginning of each run day.

3.5 Addition of Flow Constraints

Several modifications have been made to the sphere to reduce detrimental large-scale turbulence and to optimize the pitch of the flow. These modifications were baffles, or metal planes, that have been installed in the flow at certain locations to impede detrimental flow cells or to redirect the flow. The effect of these baffles is to improve the amplification and feedback mechanisms in the MDE flow necessary for a dynamo

3.5.1 Addition of Equatorial Baffle

The first baffle added to the sphere was an equatorial baffle. It is believed that the position of the shear layer between the two counter rotating hemispheres was not stable. The movement of this shear layer, described as sloshing, was dissipating the magnetic field in a critical region for building a $\ell = 1, m = 1$ dipole field. An annulus extending 3 inches into the sphere at the equator was modeled and expected to stabilize the shear layer. To implement this in the experiment an equatorial baffle was constructed that was stainless steel 0.25 inches thick and spanned 2.75 inches. The outer radius of curvature for the equatorial baffle was 20.75 inches, 0.25 less than that of the

sphere. The dimensions and the placement of the equatorial baffle can be seen in Figure 3.4. This gap was included to adjust to any imperfections in the vessel wall. Equatorial baffle was separated into 6 sections to allow a gap for the four ports located along the equator and also the drain and expansion ports on the top and bottom of the vessel. Four specialized holders were developed that used these existing ports on the equator to position the equatorial baffle and temporarily hold it in place. Quarter inch studs were welded on either side of the baffles and L-shaped brackets were bolted on. The brackets were then welded to the baffle and vessel wall locking the baffle in place.

3.5.2 Addition of Poloidal Vanes

The next modification to the experiment was the addition of poloidal vanes. In a two-vortex flow the ratio of poloidal-to-toroidal flow is critical in self-excitation. The critical magnetic Reynolds number required for self-excitation is very sensitive to this ratio (see Section 2.5). Six poloidal vanes were constructed and installed on the experiment. Three were placed in each hemisphere (at $\theta = 45$ degrees and $\theta = 135$ degrees). They were evenly spaced in the toroidal direction ($\Delta\phi = 120$ degrees). The vanes were the shape of a rectangle 20 inches by 4 inches making a union with the sphere wall (4 inches at deepest spot, approximately 1.7 inches and shallowest). They were made with a slightly smaller curvature ($r = 20.75$ inches), similar to the equatorial baffle construction, so that they could turn freely near the inner wall of the vessel.

The vanes were made out of 0.25 inch copper instead of stainless steel to allow currents induced in the sodium to pass through. To mount these vanes in place, a 2 inch hole was drilled at the desired vane locations. A 2-inch dimeter neck with a Grayloc flange was welding in place in each of the six locations. This Grayloc port is identical to the ports that the internal Hall arrays were installed in, just with shorter necks. The copper vane had a tab that mated with a cylindrical stainless steel piece with a threaded rod on the other end. The cylindrical piece was connected to a modified Grayloc end cap with a crushable graphoile gasket between cylinder and end cap. The threaded rod had a section that was flattened parallel to the vane orientation. That way, the direction of the vanes could be known from the outside, and once the Grayloc seal was loosened, it could be rotated with a wrench applying torque to the threaded rod.

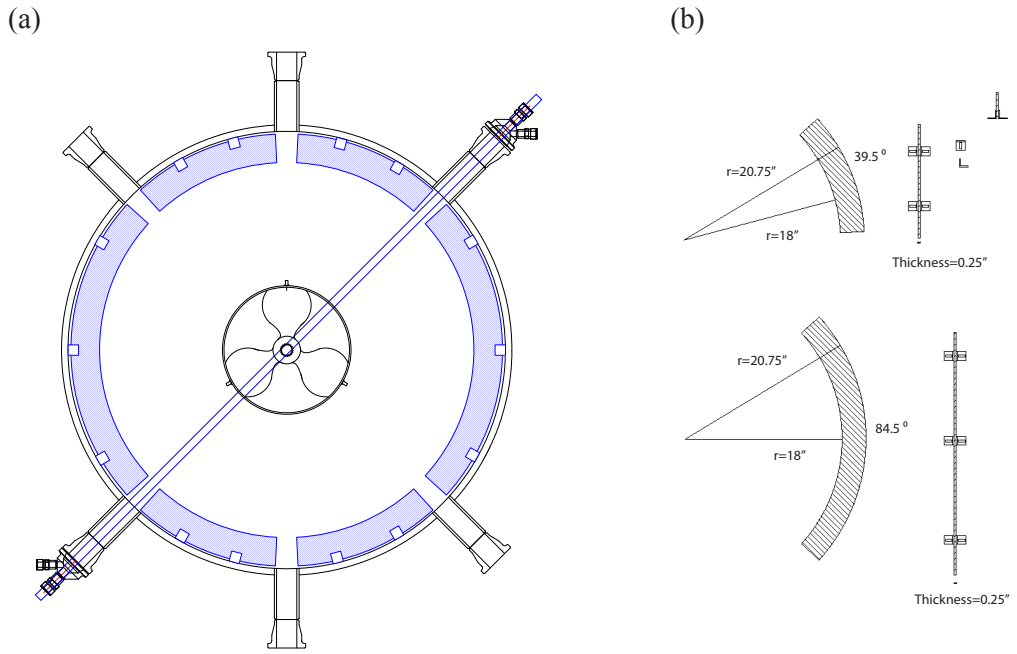

Figure 3.4 (a) A schematic of experiment with equatorial baffle installed. (b) Dimensions of the baffles and the brackets used to attach to the inner vessel wall. The equatorial baffle is constructed from 6 separate arc lengths.

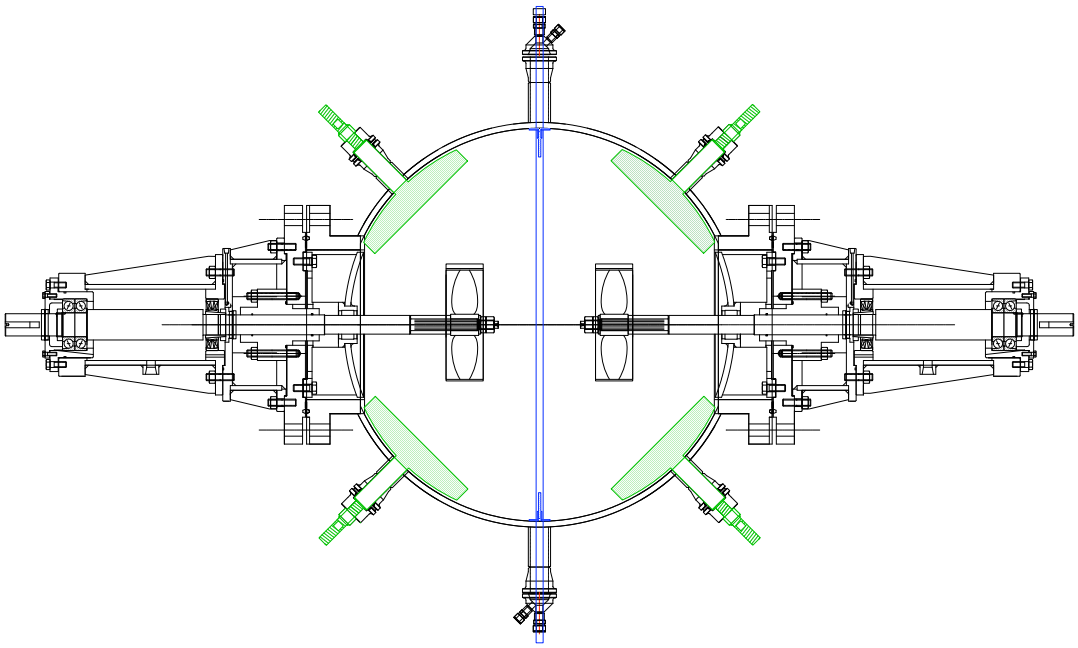

Figure 3.5 A schematic of experiment with the poloidal vanes installed (green) and the equatorial baffle and equatorial probe (blue).

3.5.3 Addition of Center Disk

The last modification to the experiment was the addition of a center disk. The benefit of reduced large-scale turbulence seemed to be reduced at higher RPM (this will be shown in Chapter 4). The center disk was installed to further separate the hemispheres and stabilize the shear region. The center disk was made out copper and split into two mating circles. The two circles are held together with 8 threaded bolts each with their own crushable graphoile seal to prevent sodium from entering the treaded area. There is a channel in both parts to allow for the equatorial probe array to pass through. There is also two threaded sections, each with a crushable graphoile gasket, perpendicular to the equatorial probe channel. Two rods with threaded ends coming through equatorial ports in the sphere are fed into the threaded sections in order to stabilize the center disk (see Figure 3.6).

The results of all these modifications to the experiment can be seen in Figure 3.7. All three of these modifications made an impact on the flow and the resulting induced field. These results will be shown in Chapter 5.

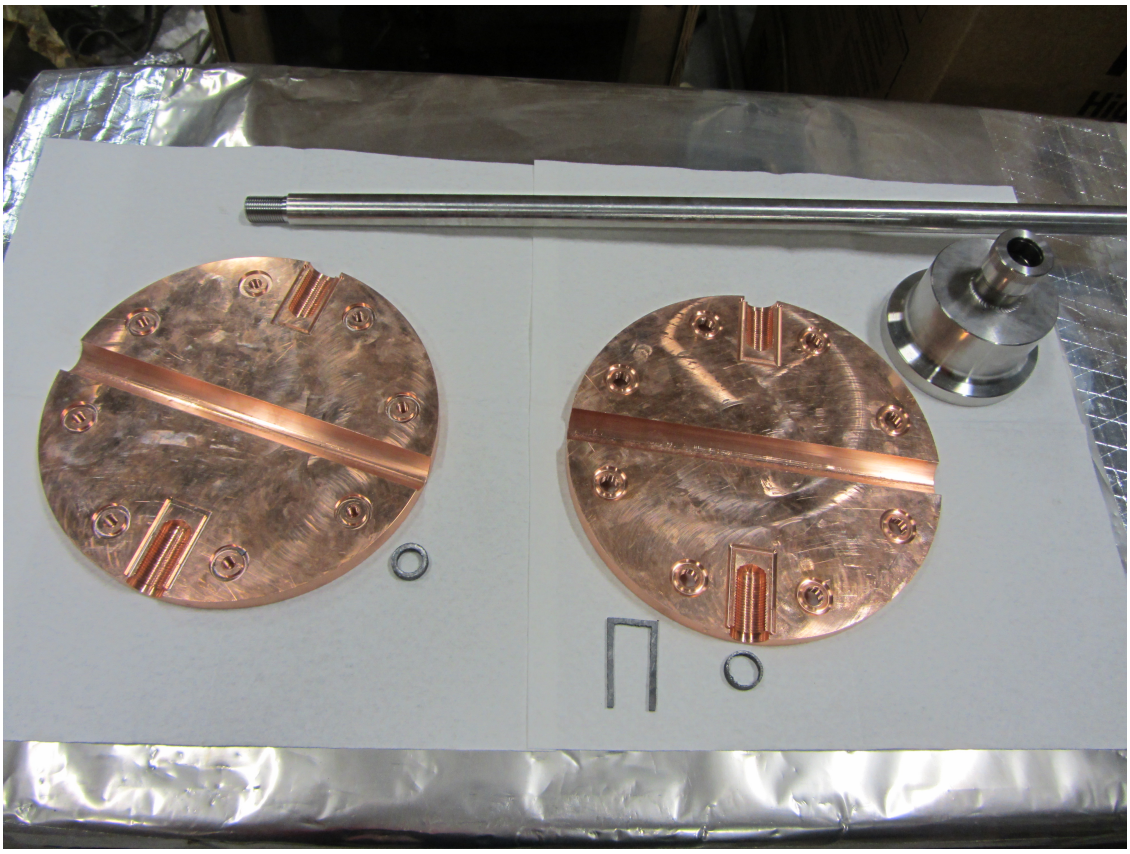

Figure 3.6 All of the components used to construct the center disk; Two mating halves of the center disk with gaskets, supporting rod, and Grayloc cap.

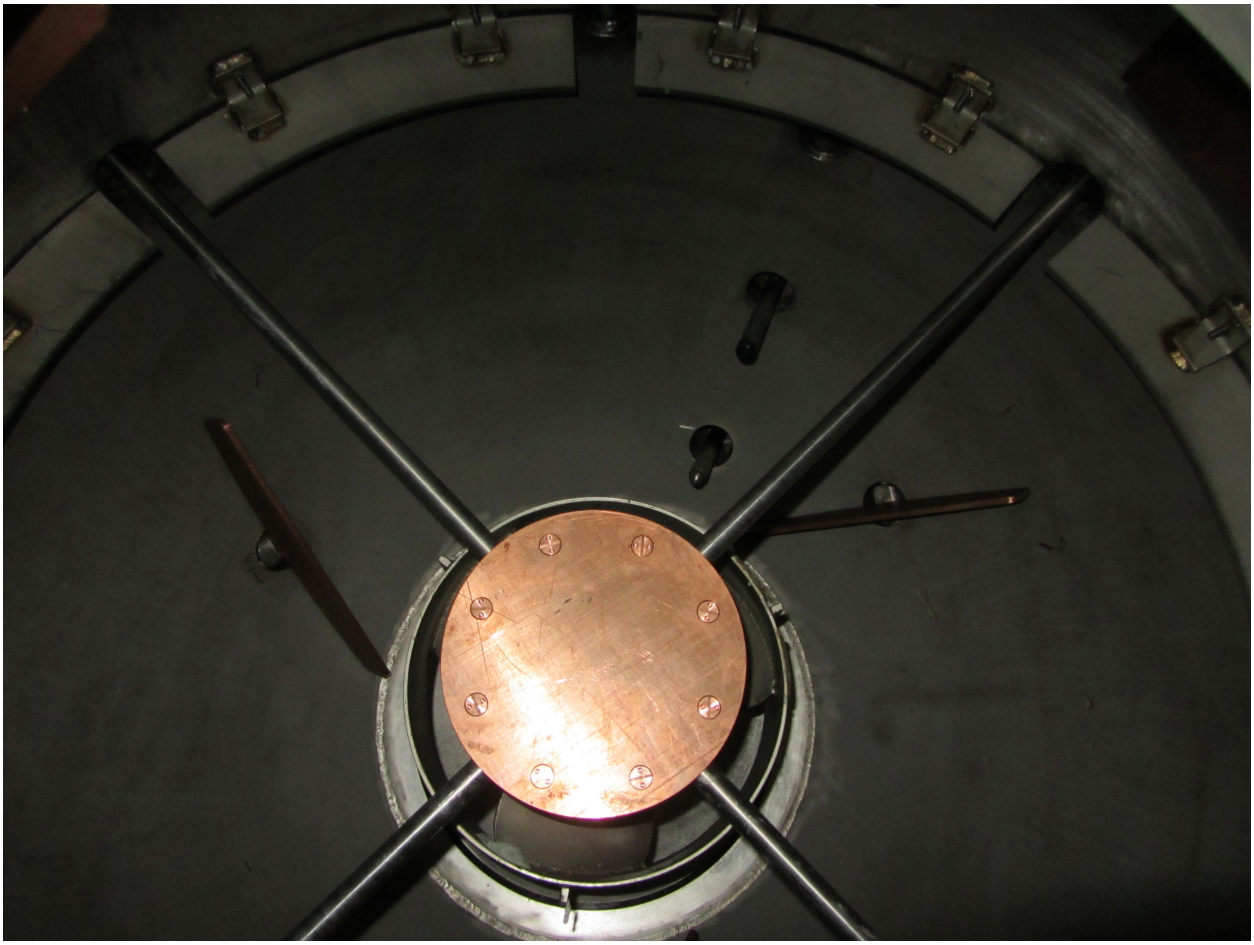

Figure 3.7 Internal view of the experiment showing the center disk installed. The disk is enclosed over the equatorial array and is supported by two rods. The equatorial baffle and poloidal vanes are also visible. Behind the disk is one of the side Hall arrays, near the pole, in a dip tube and the $\mathbf{V} \times \mathbf{B}$ probe.

Chapter 4

Modeling and Predicting Flows

4.1 Computational Fluid Dynamics Modeling

To determine the flow constraints' effects on the flow geometry and large-scale fluctuations, the flow was simulated with a Computational Fluid Dynamics (CFD) model, Fluent. The results from the CFD model were validated by comparing with data taken from an identical-scale water experiment. Physical modifications implemented in the sodium experiment were first tested with these CFD simulations. The mean velocity field was taken from these hydrodynamic simulations and put into the linear kinematic predictive solver described in Section 2.4.

4.2 Modeling MDE

The geometry and mesh used in the hydrodynamic simulations were created on a single PC with software called Gambit. To accurately replicate the impellers, a mill with a sharp tipped end bit was used to record 500 $x-y-z$ data points over the surface of a blade on a duplicate impeller of those that are used in the experiment. The data points were taken by sweeping the sharp tip in multiple radial cords along blade (for a given sweep, y-value is constant, x and z varied). A spline curve was fit to each of these radial sweeps. This resulted in approximately 20 lines that spanned the surface of a single propeller blade in the radial direction. A surface was created from these radial lines by a net surface function in Gambit that creates a surface from a mesh of lines. Only one side of the impeller was scanned with the mill tip. To give the blade a thickness and make it a volume, the surface was swept (a volume function in Gambit) the thickness of the propeller blade along the radial line at the center of the propeller blade. This is an approximation but should not affect the

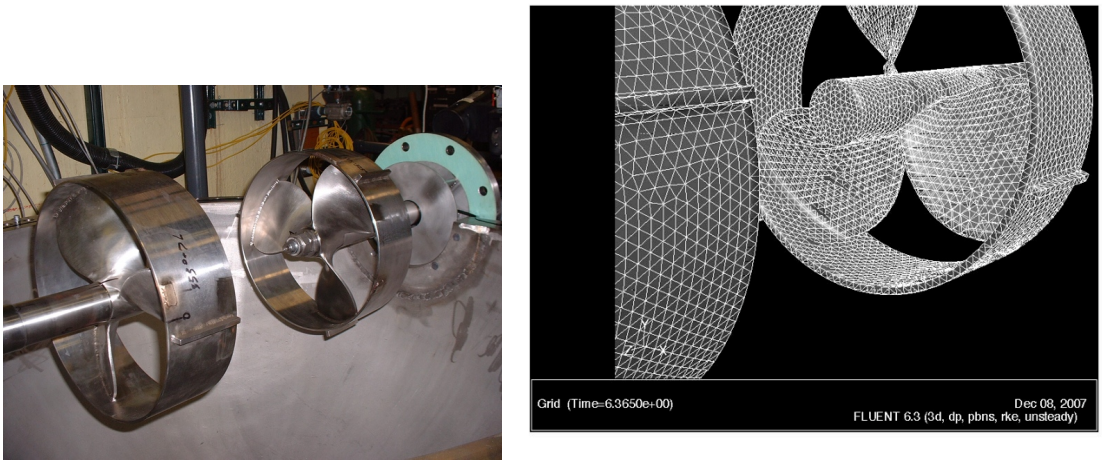

(a) Experiment (b) Fluent

Figure 4.1 (a) The impellers used to drive the flow in the experiment. (b) The impellers, with a geometry approximating the ones in the experiment, used in the CFD simulations.

large scale flows of the model significantly. Creating the geometry of the central shaft or hub of the impeller was done with a simple cylinder volume command in Gambit. The single impeller blade was then copied twice and rotated by 120 degrees in both directions, and then a Boolean operation was performed uniting the three propeller blades and the central hub which overlapped the blades. This object was then a good approximation of the impeller scanned. However, the impellers in the experiments have a K′ort ring with three 0.75 inch rectangle bars on the outer edge of the ring. This geometry was created with simple volume features and boolean operators that removed the outer two inches of the impeller and formed a union with a 12” diameter ring and 0.75 inch rectangles. The last approximation made in the impeller geometry was smoothing the joints between the blades and the hub using Gambit’s fillet feature, with a fillet radius of about 0.5 inches.

Two of these modeled impellers and drive shafts are placed in a perfect 42 inch diameter sphere. The simulated domain is split into three separate volumes. Two smaller cylindrical volumes surrounding the rotating impellers and a larger volume containing the rest of the domain. The reason for this is when the mesh is uploaded into Fluent, the two smaller domains are to be solved using a

moving mesh that is rotating at the same angular velocity that the impellers are rotating at and the large domain can be solved in a stationary reference frame.

For cases with an equatorial baffle a 3-inch annulus (39-inch inner diameter) or 6-inch annulus (36-inch inner diameter) was merged with the 42 inch diameter sphere at the equator. In cases with the poloidal vanes, six 14-inch by 3-inch rectangles were merged with the sphere wall with the center of the outside edge of each rectangle located at $\theta = 45^\circ$ and 135° and $\phi = 0^\circ$, 120°, and 240°. The baffles that were installed on the experiment were matched to the dimensions in the simulation.

4.3 CFD Generated Flows

The geometry and mesh for the simulations, created on a single PC, were loaded on to a 12-node cluster constructed for running CFD simulations. After a Fluent case had converged, 13 meridional slices ($r - z$ planes in cylindrical geometry) were created and the velocity in all three directions at each node in the plane was outputted to a data file. All of the CFD generated flows were found to be very axisymmetric. The variation in the flow between different meridional planes was small. A Matlab routine was used to read the data from each plane, fit it to a regular grid (in the $r - z$ plane) and then average the 13 different values (azimuthal symmetry is assumed). Changing the number of meridional slices used in the averaging did not significantly impact the resulting mean flow. The velocity data, still in spherical coordinates, and the average velocity fit to a regular grid in cylindrical coordinates are saved to a data file that is read by an IDL routine. The velocity is then converted from cylindrical to spherical coordinates

Since the data grid is so dense we can directly integrate the data to get the toroidal and radial profiles. Starting with the axisymmetric expansion of the velocity field from Section 2.2

$$v_\theta(r,\theta,\phi) = \sum_\alpha \frac{1}{r}\frac{\partial s_\alpha(r)}{\partial r}\frac{\partial Y_\alpha(\theta,\phi)}{\partial \theta}$$

$$v_r(r,\theta,\phi) = \sum_\alpha \frac{\ell_\alpha(\ell_\alpha+1)}{r^2} s_\alpha(r) Y_\alpha(\theta,\phi)$$

$$v_\phi(r,\theta,\phi) = -\sum_\alpha \frac{t_\alpha(r)}{r}\frac{\partial Y_\alpha(\theta,\phi)}{\partial \theta}.$$

Using the orthogonality relations of spherical and partial spherical harmonics

$$\int Y_\alpha(\theta,\phi)Y_\beta(\theta,\phi)\sin\theta d\theta d\phi = \delta_{\alpha,\beta}$$

$$\int \frac{\partial Y_\alpha(\theta,\phi)}{\partial\theta}\frac{\partial Y_\beta(\theta,\phi)}{\partial\theta}\sin\theta d\theta d\phi = \ell_\alpha(\ell_\alpha+1)\delta_{\alpha,\beta}.$$

The individual toroidal and poloidal profiles for the flow become

$$s_\alpha(r) = \frac{r^2}{\ell_\alpha(\ell_\alpha+1)}\int v_r(r,\theta,\phi)Y_\alpha(\theta,\phi)\sin\theta d\theta d\phi$$

$$t_\alpha(r) = -\frac{r}{\ell_\alpha(\ell_\alpha+1)}\int v_\phi(r,\theta,\phi)\frac{\partial Y_\alpha(\theta,\phi)}{\partial\theta}\sin\theta d\theta d\phi.$$

In these cases only axisymmetric flows are considered ($m = 0$). For efficiency, the integration is done up up to $\ell = 14$. The vast majority of the flow energy is in the lowest modes. Shown in Figures 4.2, 4.3 and 4.4 are the toroidal and poloidal velocity radial profiles from several different CFD simulations where the poloidal vanes were oriented at different angles and their corresponding contour plots of the velocity field.

The different CFD simulated flows showed that the equatorial baffles and poloidal vanes could alter the shape of the flow. But an equally important effect of adding these constraints to the flow is the reduction of detrimental fluctuations in the experiment. Fluent can also model the amount of turbulent energy present in the flow simulations. Shown in Figure 4.5 is the amount of turbulent kinetic energy in on one meridional slice (r-z planes in cylindrical geometry) for three different 800 RPM simulations with no baffles, just an equatorial baffle and with both an equatorial baffle and poloidal vanes at 45 degrees. The turbulent energy is the intensity of k in the realizable $k-\epsilon$ turbulence modeling used in the simulations.

Recall from Section 2.6 that the β-effect acts as an enhanced dissipation lowering the effective conductivity of the flow. By referencing the simplified expression for the turbulent EMF in Equation (2.30), the β-component of the EMF scales as $\beta \sim \tilde{v}^2\tau_{coor}/3 = \tilde{v}\ell_v/3$. Where $\tilde{v}$ is the rms fluctuation level and ℓ_v is the eddie size. Therefore, the effective magnetic Reynolds number (Rm_{eff}) becomes

$$Rm_{\text{eff}} = \mu_0\sigma_{\text{eff}}VL = \frac{\mu_0\sigma VL}{1+\mu_0\sigma\tilde{v}l_v/3}. \tag{4.1}$$

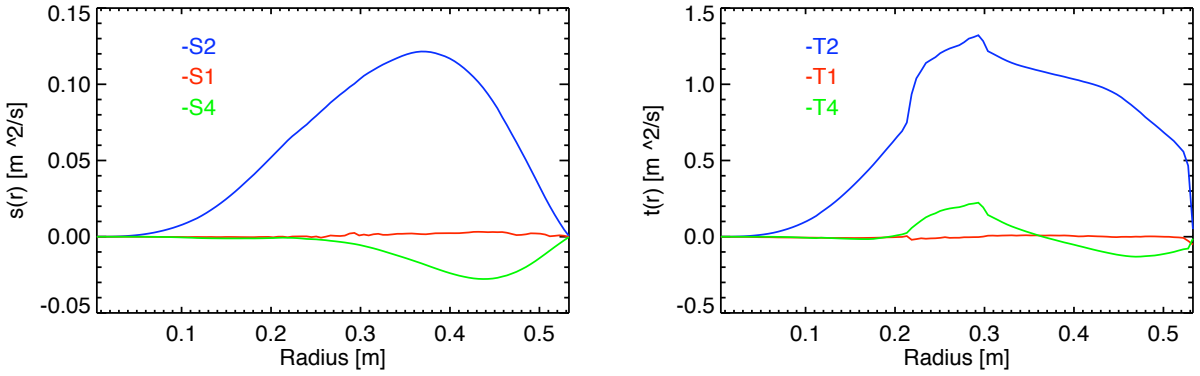

(a) Poloidal Radial Profiles

(b) Toroidal Radial Profiles

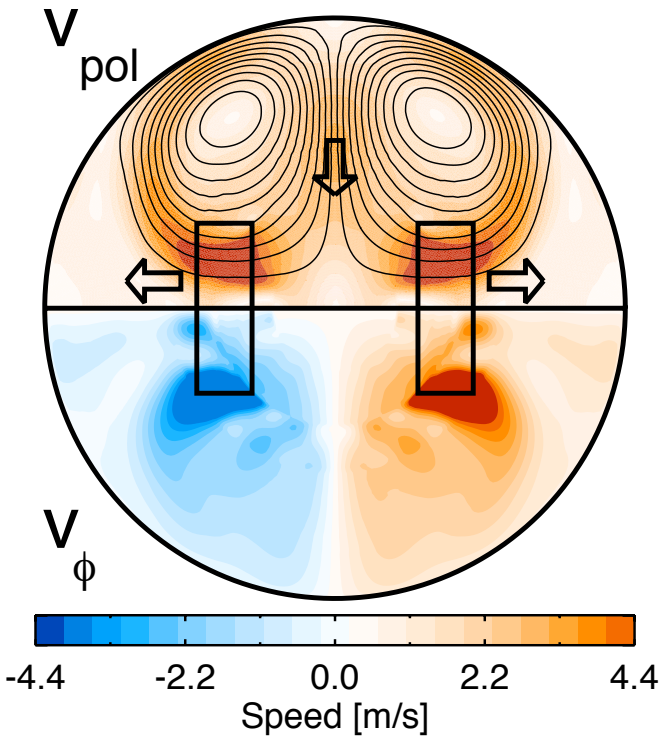

(c) Velocity Contour

Figure 4.2 (a) The poloidal and (b) the toroidal radial profiles from the CFD simulations with a 3-inch equatorial baffle and the poloidal vanes at 30 degrees. (c) The corresponding contour plot of the velocity field created by the poloidal and toroidal profiles.

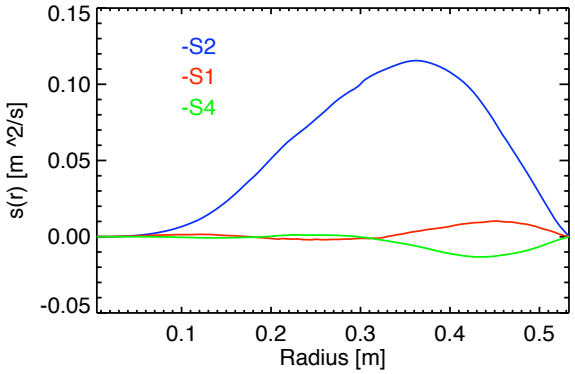

(a) Poloidal Radial Profiles

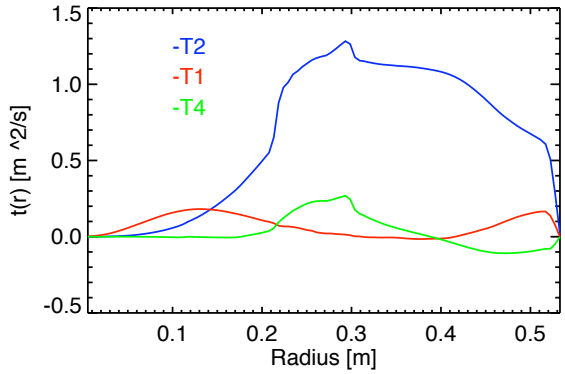

(b) Toroidal Radial Profiles

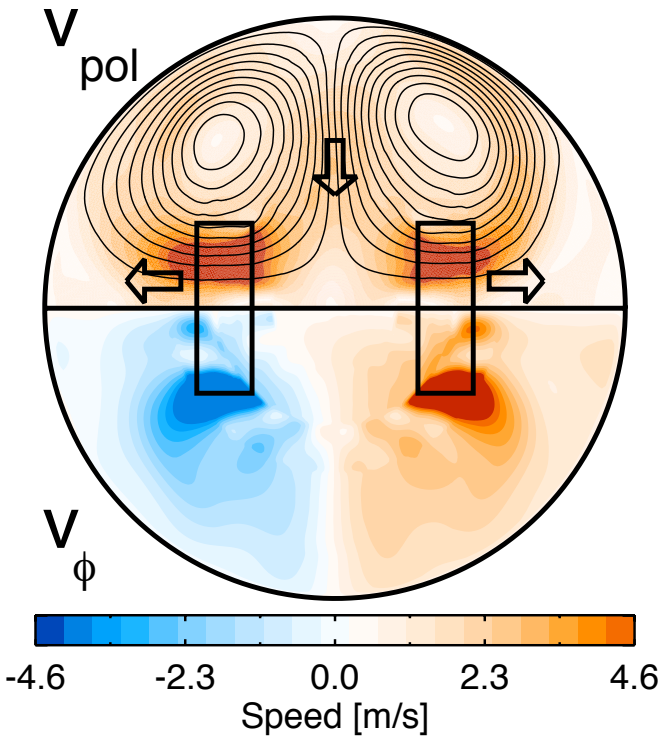

(c) Velocity Contour

Figure 4.3 (a) The poloidal and (b) the toroidal radial profiles from the CFD simulations with a 3-inch equatorial baffle and the poloidal vanes at 45 degrees. (c) The corresponding contour plot of the velocity field created by the poloidal and toroidal profiles.

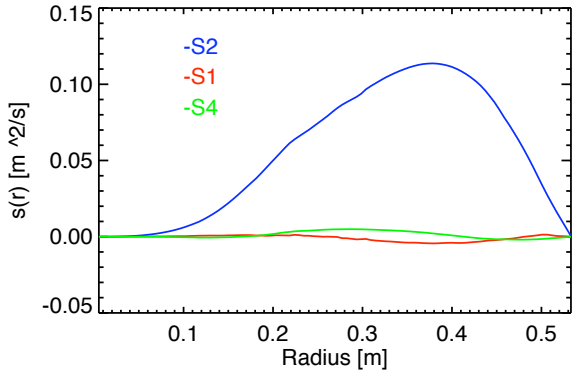

(a) Poloidal Radial Profiles

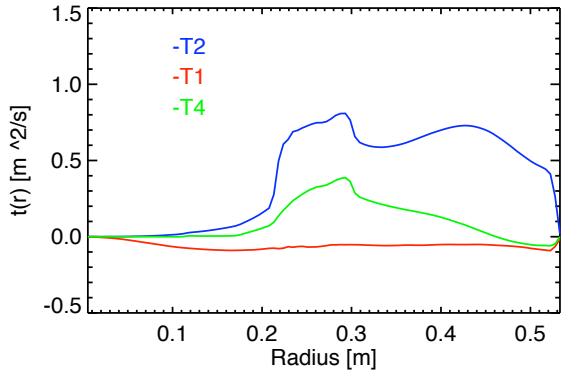

(b) Toroidal Radial Profiles

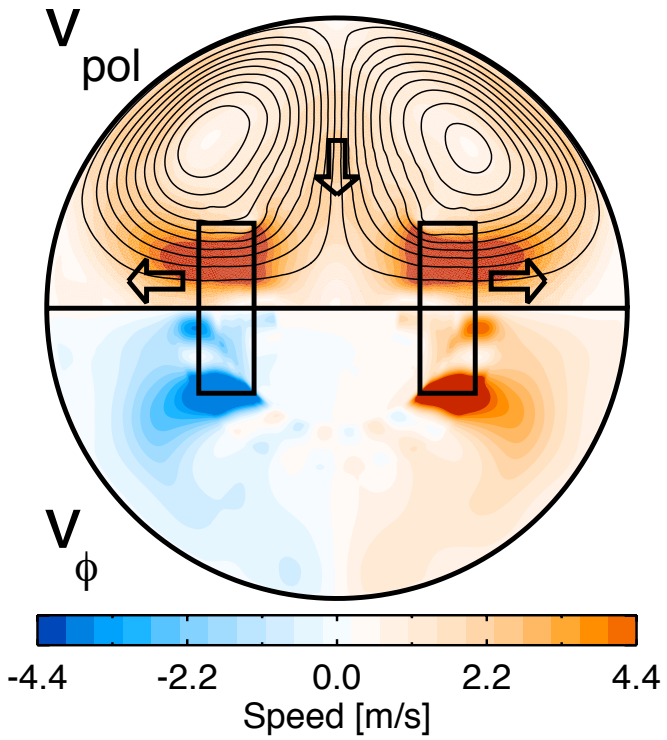

(c) Velocity Contour

Figure 4.4 (a) The poloidal and (b) the toroidal radial profiles from the CFD simulations with a 3-inch equatorial baffle and the poloidal vanes at 60 degrees. (c) The corresponding contour plot of the velocity field created by the poloidal and toroidal profiles.

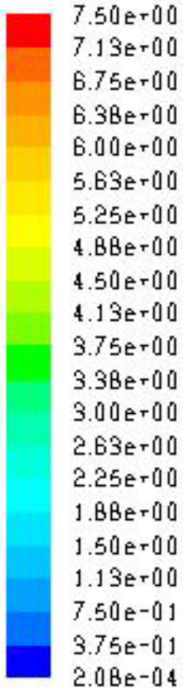

(a) Turbulent Kinetic Energy

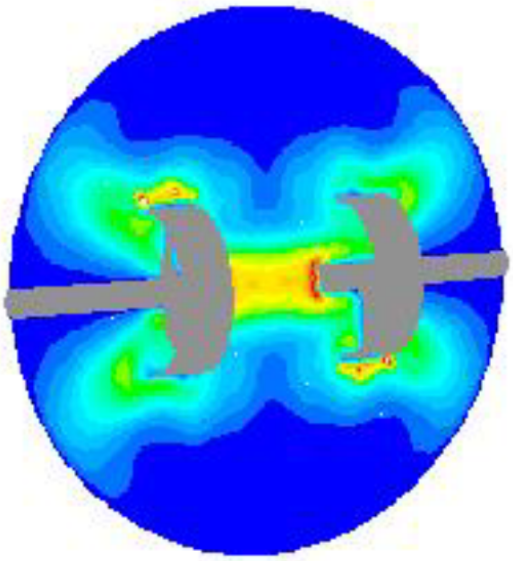

(b) No Baffles

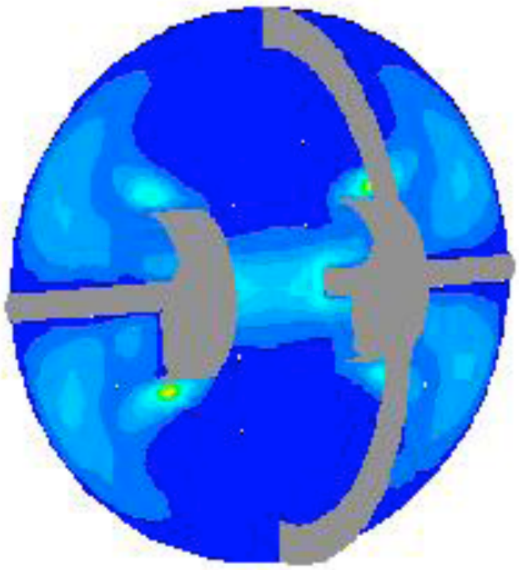

(c) Velocity Contour

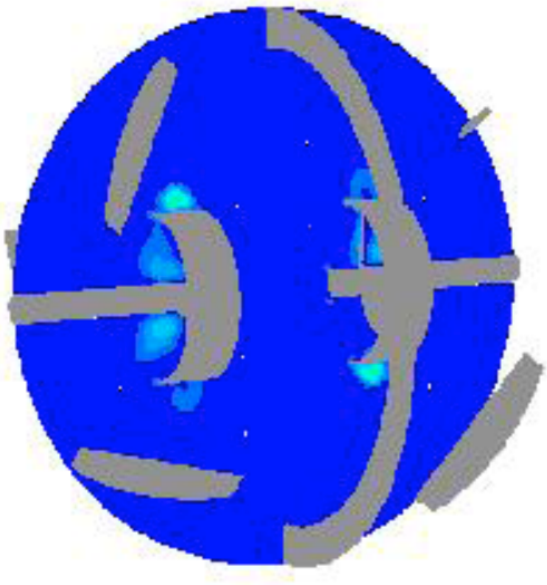

(d) Poloidal Radial Profiles

Figure 4.5 (a) The scale for the amount of turbulent energy the CFD modeled flows in m^2/s^2. The turbulent energy on one meridional slice for three different CFD flows: (b) A flow with no baffles, $\tilde{v}^2 = 0.78m^2/s^2$. (c) A flow with just an equatorial baffle, $\tilde{v}^2 = 0.42m^2/s^2$. (d) A flow with both an equatorial baffle and poloidal vanes, $\tilde{v}^2 = 0.06m^2/s^2$

By assuming that the scale length of the fluctuations (l_v) scales with the intensity of the fluctuations ($\tilde{v}$) the excepted reduction in the effective conductivity (β-effect) for each of the CFD flows can be solved for. Table 4.1 summarizes the results from comparing the three simulations shown in Figure 4.5. As more constraints were added, the turbulent energy in the flow was reduced while the magnitude of the mean flow remained constant. All three simulations had equivalent Rm's as computed by magnitude of the mean flow. However, if one calculates the expected reduction in conductivity due to the β-effect, the expected Rm_{eff} goes from 60% to 95% of Rm.

case	turbulent energy	$\tilde{v}_{\text{rms}}/\text{v}_{\text{rms}}$	Rm_{eff}
no baffles	0.71 m^2/s^2	0.35	$0.60Rm$
equatorial baffle only	0.42 m^2/s^2	0.25	$0.75Rm$
poloidal vanes added	0.06 m^2/s^2	0.1	$0.95Rm$

Table 4.1 The volume averaged turbulent intensity ($\tilde{v}^2$) from the three 800 RPM fluent simulations shown in figure 4.5. With each new constraint the energy in the fluctuations became a smaller fraction of the energy in the mean flow resulting in smaller reduction in expected Rm_{eff}.

4.4 Laser Doppler Velocimetry

Sodium is optically opaque and very few diagnostics are available to directly measure the flow. An identical scale water experiment was constructed to measure the flow in the sodium experiment. The kinematic viscosity of water at 35 degrees [Robert C. Weast, 1986] is nearly identical to that of liquid sodium at 115 degrees [Shpil'rain et al., 1985]. The water experiment is a 42-inch diameter stainless steel sphere with two counter rotating impellers of the same customized geometry but opposite handiness as the sodium experiment. The impellers are driven by two 50 kW motors that can rotate up to 1200 RPM.

Velocity measurements were taken with a method called Laser Doppler Velocimetry (LDV). The water experiment sphere has five 1-inch thick Pyrex windows at 5 different latitudes (θ coordinates). All of the windows are at a single longitude (ϕ position) at the top of the sphere.

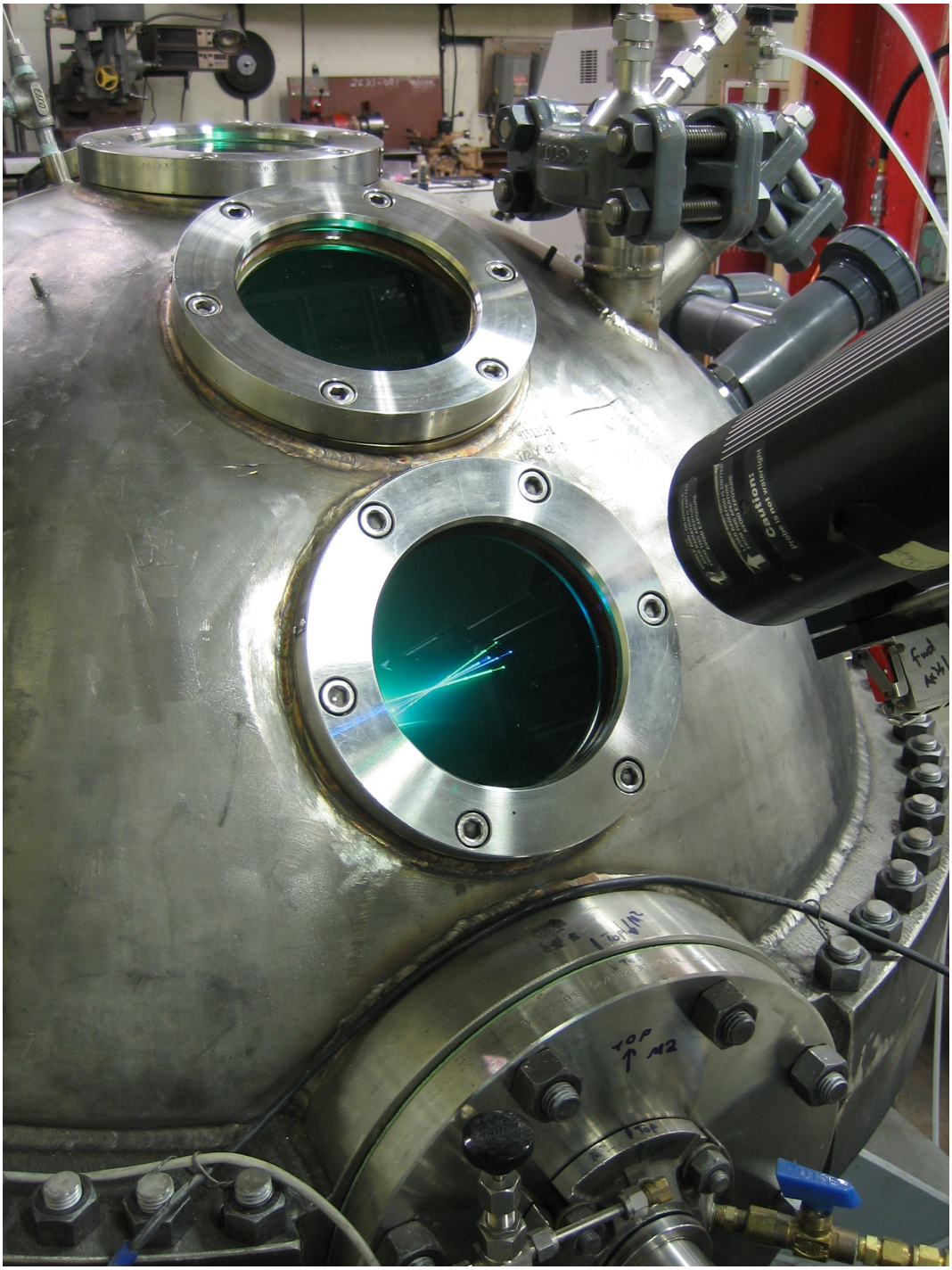

Figure 4.6 The Laser doppler velocimetry probe taking measurements of the velocity field in an identical-scale water experiment. The intersecting lasers create an interference pattern in the flow. The water is seeded with particles that reflect the light back, allowing for the velocity to be measured.

The LDV system consists of a 5 Watt Argon-Ion laser that is directed into a beam separator that partitions the laser light into green (514 nm) and blue (488 nm) beams. These beams are then split to create four total. These four beams travel through fiberoptic cables to a probe head that focuses and angles the four beams through one of the windows so that they intersect at a single location in the water. The probe head can be swept to be positioned above each of the five windows. A stepper motor can move the probe head in the radial direction closer and further from the window so that the beams intersect and multiple radial positions in the flow. The two intersecting laser beams of each color create an optical interference pattern. The water in the experiment is seeded with neutrally buoyant, reflective, pieces of mica. As the mica particles pass through the interference pattern they reflect the pattern back to the fiberoptic probe head. The reflected light is transmitted from the probe head through fiberoptic cable to a ColorLink Plus Multicolor Receiver. The speed of the passing particles shifts the frequency that the interference pattern is received. The two blue beams are oriented perpendicular to the two green beams so that the green interference pattern measures v_θ and the blue interference pattern measures v_ϕ

The water velocity field is measured at 99 locations spread out over the five viewing windows. The mean velocity field at each point is determined by averaging 3000 measurements. Unlike the CFD simulations, the data is not dense enough to use direct integration to determine the structure of the radial profiles. Instead the poloidal and toroidal radial profiles were fit to the data using a cubic spline interpolation. This technique is the same basic fitting concept used to fit the internal magnetic data and is described in more detail in the next chapter. The boundary conditions for the fitting profiles are determined by physical constraints of the experiment. Both $s_\alpha(0) = 0$ and $t_\alpha(0) = 0$ or else the velocity would go to infinity at the origin. At the vessel wall $s_\alpha(r_0) = 0$ otherwise fluid would be escaping the vessel. For the toroidal flow, the no-slip boundary condition is not enforced due to the the very thin boundary layer in high fluid Reynolds number flows ($Re \sim 10^5$). However, for the cubic spline fitting, some boundary condition must be specified: $\frac{\partial^2 t_\alpha(r_0)}{\partial r^2} = 0$. There is no physical motivation for this boundary condition. The number of spherical harmonics and fixed spline points used in the fit were determined by trial and error of the user. The results from the LDV experiment at 1000 RPM can be seen in Figure 4.7. In this water experiment data

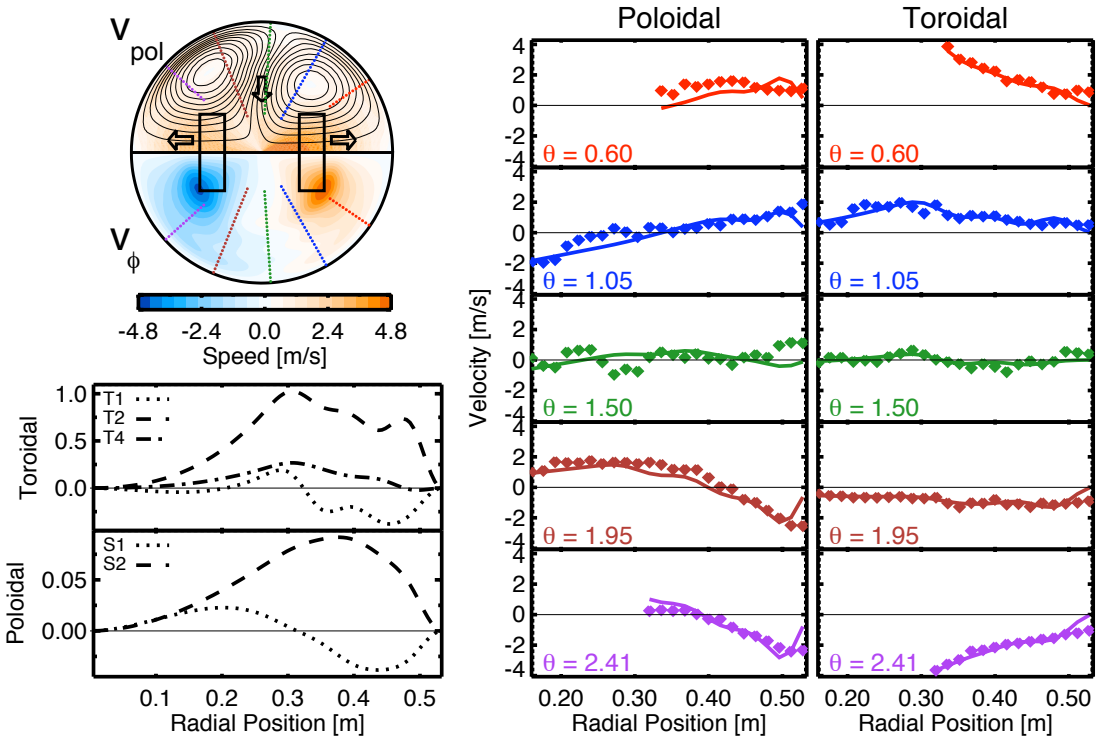

Figure 4.7 The LDV data from a 1000 RPM is the mean velocity measured at 99 individual points along 5 separate cords. The measured velocity is indicated by the dots, the fit is shown with the solid lines. The velocity is fit with two poloidal harmonics (s_1,s_2) and three toroidal harmonics (t_1,t_2,t_4). Each of the radial profiles in the fit was built with six cubic spline points.

set the dip tubes (thermal wells) used for the magnetic diagnostics were installed to study their effect, if any, on the mean flow.

The profiles from the CFD simulations qualitatively agreed with the mean field profiles fit to the LDV data from the water experiment shown in Figure 4.8. One significant difference between the simulations and the LDV data was that the velocity data from the water experiment could not be accurately fit without the use of an odd harmonic (ℓ=1). Odd harmonics in the flow indicate an in-balance between the two counterrotating hemispheres. In an optimized flow, the two hemispheres should be mirror-symmetric across the equator. The results from the LDV water experiments enforced the need for an equatorial baffle to assist in stabilizing the shear region between the two hemispheres and help maintain symmetry across the equator. The LDV results were also used along with the CFD simulations to determine that the pitch of the flow was not optimal and could be improved with the installation of the poloidal vanes.

4.5 Pitch Parameter Defined

The mean flows produced by the Fluent simulations can be inserted into the predictive eigenvalue solver described in Section 2.5. The solver indicates whether the flow profiles are capable of generating a self-excited field and also what the critical magnetic Reynolds number is. One of the essential parameters for self-excitation in a two-vortex flow is the ratio of poloidal to toroidal flow. A pitch parameter that characterizes this ratio has been defined as

$$\mathrm{P} = \sqrt{\frac{\mathrm{E}_{pol}}{\mathrm{E}_{tor}}} \tag{4.2}$$

where E_{pol} and E_{tor} are the kinetic energy in the poloidal and toroidal flow. More explicitly

$$\mathrm{E}_{pol} = \frac{1}{2\rho}\int_V \mathbf{v}_{pol}^2 \mathrm{d}V$$

$$\mathrm{E}_{tor} = \frac{1}{2\rho}\int_V \mathbf{v}_{tor}^2 \mathrm{d}V.$$

Results of the solver for the LDV data set can be seen in figure 4.9. The plot on the left shows that the growth rate for the least damped mode vs Rm for an two-vortex flow measured in the identical-scale water experiment. The flow is expected to produce a self-excited field at Rm=126.

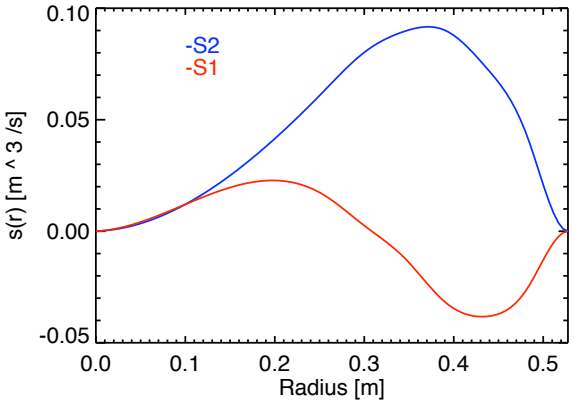

(a) Poloidal Radial Profiles

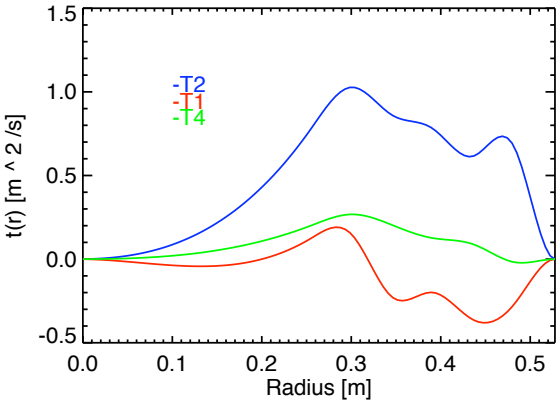

(b) Toroidal Radial Profiles

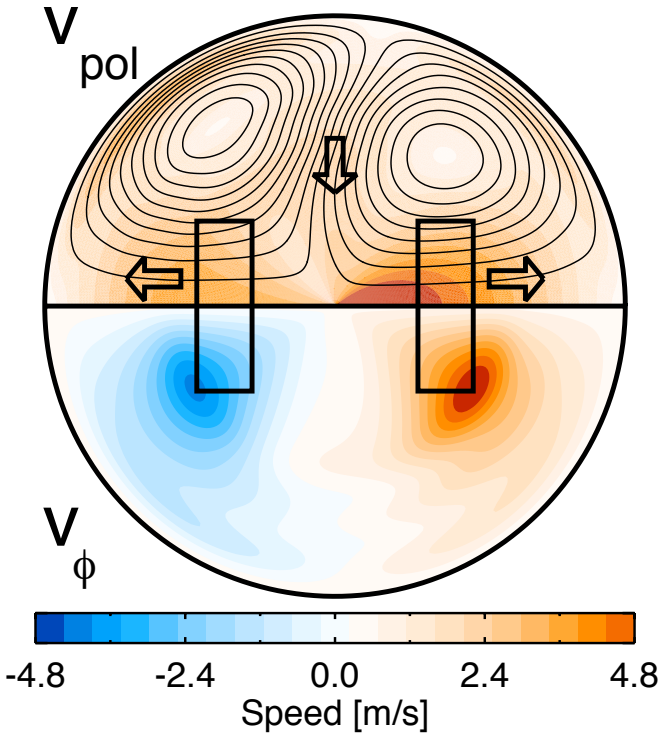

(c) Velocity Contour

Figure 4.8 (a) The poloidal and (b) the toroidal radial profiles from a 1000 RPM LDV dataset with 7 dip tubes installed. (c) The corresponding contour plot of the velocity field created by the poloidal and toroidal profiles. Note the lack of symmetry across the equator in the velocity field.

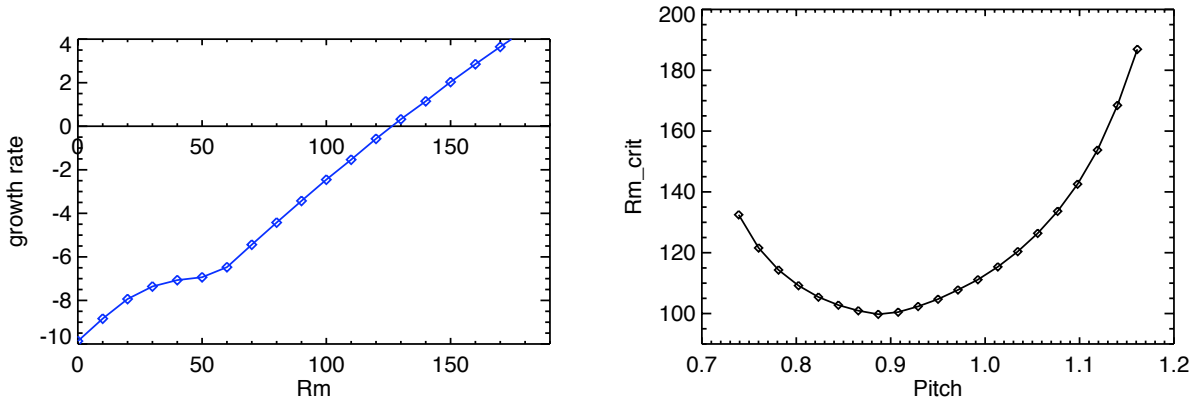

(a) Poloidal Radial Profiles

(b) Toroidal Radial Profiles

Figure 4.9 (a) The predicted growth rate, in units of $[\tau_\sigma]^{-1}$, of the fastest growing (least damped) mode for the flow fit to the measured LDV data. τ_σ=$\mu_o \sigma L^2$ is the resistive decay time for the flow. The critical magnetic Reynolds number (Rm_{crit}) is where the growth rate crosses from negative to positive. (b) Rm_{crit} depends on the pitch parameter which describes the ratio of poloidal to toroidal flow.

By varying the pitch of the flow and running through the same eigenvalue solver, we see that the LDV flow had a pitch=1.04, but observing the plot on the right hand side, Rm_{crit} is at a minimum when the pitch=0.84. The point at which Rm_{crit} is at a minimum is considered the optimum pitch. This pitch parameter is is proportional to ε used in Figure 1.4 and Figure 2.3. Setting ε=1.15 is equivalent to increasing pitch by 15%. It is beneficial to use the pitch parameter instead of ε because it provides a physically defined quantity that describes the helical pitch of a two-vortex flow.

A survey of seven different flows was performed. All of the flows were run through the kinematic solver and had their pitch modified to find the optimum. The results are summarized in the table 4.5. The survey includes four CFD generated flows with just the equatorial baffle and with the equatorial baffle and poloidal vanes at 3 different angles (30°, 45°, 60°). Also shown are results from two flow profiles fit to LDV data taken from the identical scale water experiment run at 1000 rpm. The first two rows in the table are two ideal profiles; the Dudley-James flow and the optimized Forest-O'Connel flow [Forest et al., 2002].

Flow	Rm_{crit}	Pitch	P_{opt}
Dudly-James	50.3	0.82	0.82
O'Connel	47.5	0.74	0.78
LDV ds87	126.4	1.0	0.84
LDV ds49	195.0	1.04	0.90
CFD800 3inch	179.3	0.56	0.77
CFD800 v30	204.8	1.01	0.86
CFD800 v45	140.6	0.89	0.82
CFD800 v60	—-	1.2	0.82

Table 4.2 The results of running multiple flow profiles through the eigenvalue solver and varying the pitch of each flow until a minimum in Rm_{crit} is found. P_{opt} is the value of the pitch where Rm_{crit} is minimized. The CFD flow with the vanes a 60 degrees did not dynamo at any value of Rm until the pitch was modified, allowing for a P_{opt} to be found.

It must be noted that the Rm used in the kinematic solver is calculated with the characteristic velocity as the the maximum velocity in the flow. The large disparity in critical magnetic Reynolds number between the ideal flows and the CFD/LDV flows is mostly due to the fact that the simulated and measured LDV flow profiles having non-optimal shapes and pitches. Another contributor to the disparity in Rm_{crit} is the sharply peaked profiles in the CFD flows. If the magnetic Reynolds number were computed with an average velocity instead of the maximum velocity some of this disparity would be reduced.

There are three major takeaways from the survey of two-vortex flows: First, here is a consistent optimal pitch for all the flows around 0.82. These flows had different profiles and ratios of poloidal to toroidal flow, but all had a very similar value for optimal pitch. Second, the two different LDV datasets were analyzed with a different number of harmonics and by different experimenters, however, both fits agree with a similar pitch that is much higher than optimal. Third, implementing and rotating the poloidal vanes from 30 degree to 45 degrees in the CFD simulations altered the pitch of the flow in the desired direction.

The implications of the CFD simulations are that the addition of constraints to the flow (the equatorial baffle and poloidal vanes) reduced the total turbulent kinetic energy. Also, adding and rotating the vanes can adjust the pitch of the flow. Ideally the baffles and vanes would have first been implemented in the water experiment and their effect on that flow verified experimentally. Due to limited manpower and time, the baffles were only installed in the sodium experiment. The effects of adding these constants on the flow were evaluated with measuring the response magnetic field and motor power requirements.

Chapter 5

Measuring Magnetic Fields

This chapter goes over results taken from the Madison Dynamo Experiment. It explains methods for benchmarking flow performance and shows that response fields now match predictions.

5.1 Motor Power as an Indicator of Turbulence and Pitch

Results from earlier experiments on the Madison Dynamo Experiment have shown that turbulence played a significant and purely detrimental role in the generation of magnetic fields. The installation of the equatorial baffle, poloidal vanes, and center disk described in the previous chapter was done to reduce the turbulent fluctuations and optimize the helical pitch of the flow. One method to determine how much the turbulence has been reduced is to look at the motor power required to spin the flow at set speeds. The viscous drag force of on object moving trough a fluid is proportional to the velocity squared. The work done to move through a vicious medium (force • velocity) should be proportional to the velocity cubed.

$$P \sim A\frac{1}{2}\rho v^3 \tag{5.1}$$

If the amount of energy required to spin the fluid at a set speed changes, then that excess energy is being dumped into turbulent energy that cascades down to smaller scales until it is dissipated as heat. In a standard Kolmogorov spectrum, the energy in fluctuations cascades from the largest scales to smaller scales as

$$E_v(k) = C\varepsilon^{2/3}k^{-5/3}. \tag{5.2}$$

In the case of the Madison Dynamo Experiment, the amount of energy in the turbulent spectrum is equal to the amount of energy added to the flow at the largest scales with the impellers

$$\varepsilon = \frac{P}{\frac{4}{3}\pi a^3 \rho}. \tag{5.3}$$

The installation of the equatorial baffle caused a large drop in the amount of power required to spin at a set speed. This can be seen in Figure 5.1. Adding the equatorial baffle reduced the amount of power required by approximately 25%. Also, removing the dip tube that contained the magnetic diagnostics had no impact on the motor power.

These motor power curves can also be used to characterize the effect of the poloidal vanes. Shown in Figure 5.2 is the motor power curves from ramping up to max speed with just the equatorial baffle and then compare that to the curves with the equatorial baffle and the poloidal vanes at 30 degrees the power required is almost identical. The power curve for the equatorial baffle and vanes at 45 degrees has a higher power requirement and the case where the vanes where at 60 degrees is even higher. This indicates that the natural pitch of the flow created with just the impellers and the equatorial baffle probably aligns with the baffle at 30 degrees. As you rotate the vanes more they start the impede the natural flow more changing the flow but also creating more turbulence.

The effect of the last flow constraint, the center disk, can been seen in Figure 5.3. With the addition of the center disk at the equator, a drop in the motor power curves was observed when the vanes where at 45 degrees. Not nearly as significant a drop was observed when the vanes where at 30 degrees. This indicates that the additional turbulence that was created by rotating the vanes to 45 degrees was suppressed by the addition of the center disk. From these motor power curves, it appears that the flows with the least amount of turbulent kinetic energy are the case with just the equatorial baffle and poloidal vanes at 30 degrees and the case with the equatorial baffle, center disk, and poloidal vanes at both 30 and 45 degrees.

A parallel method of associating mechanical energy to level of turbulence is to measure the increase in temperature of the sodium. Energy is injected into the flow at the largest scales by the two impellers powered by up to 150 kW of motor power. The turbulent energy cascades down to smaller and weaker eddies until it dissipates. By logging the increase in sodium temperature during

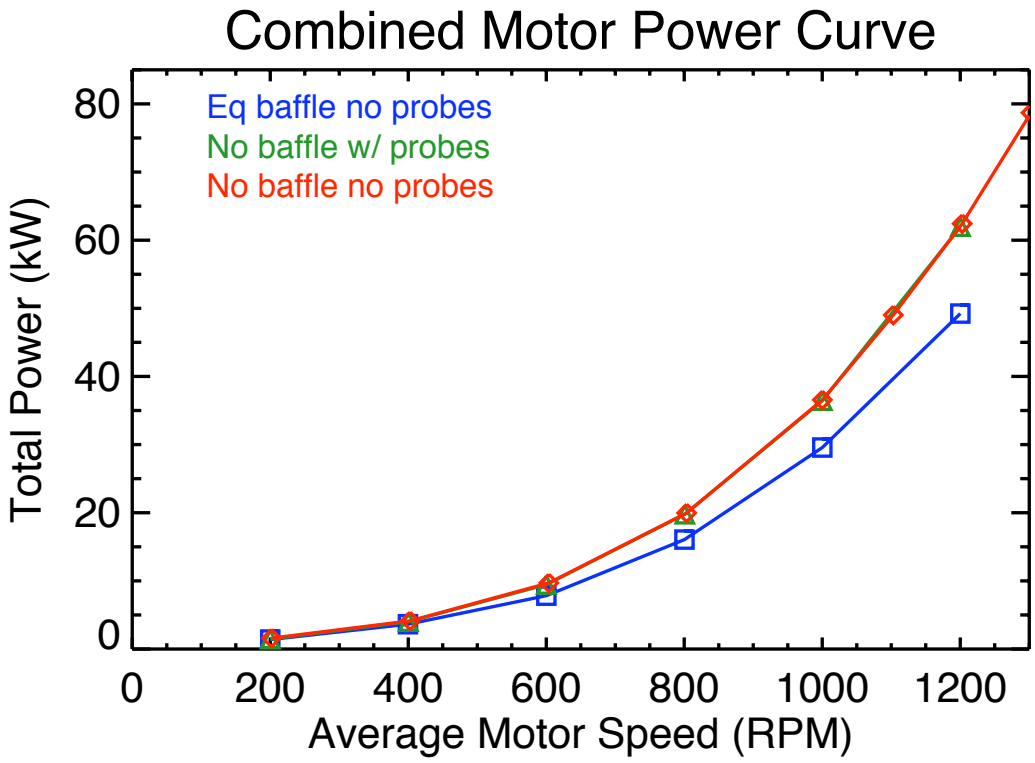

Figure 5.1 The amount of power required to spin the impellers at several different fixed speeds. The presence of the dip tubes made no significant impact on the motor power. The addition of an equatorial baffle greatly reduced the amount of power required. Flows with the equatorial baffle require less motor power, thus there is less energy in turbulent fluctuations.

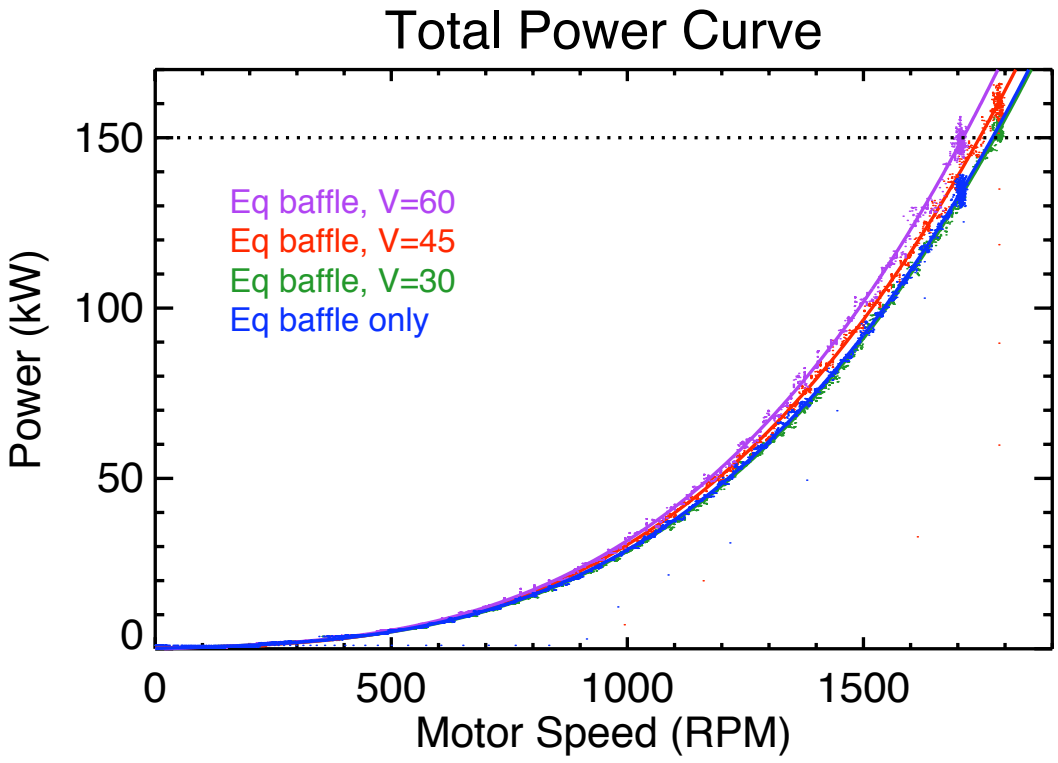

Figure 5.2 The amount of power required to spin the impellers vs rotation rate for several baffle configurations. Adding poloidal vanes at 30 degrees to the equatorial baffles did not effect the power requirements. As the vanes were rotated to 45 and 60 degrees more power was required. The vanes at 30 degrees are aligned closely with the natural pitch of the flow with just the equatorial baffles. Rotating the vanes to a larger angle is altering the flow but also adding turbulence.

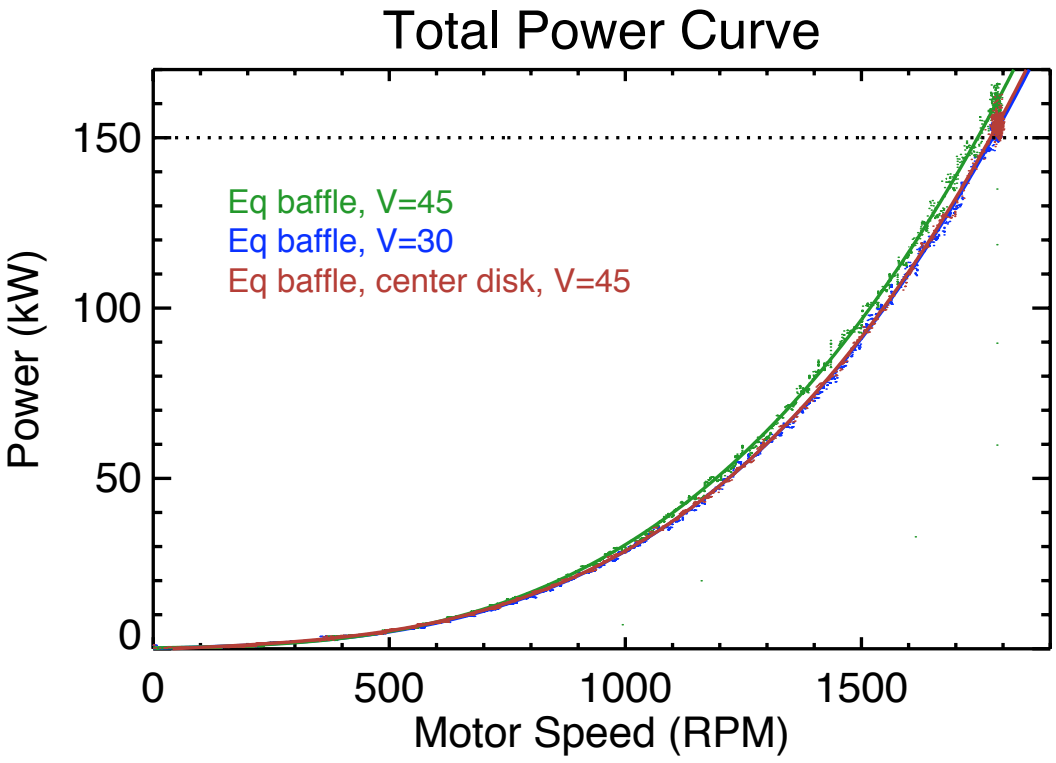

Figure 5.3 The amount of power required to spin the impellers vs rotation rate for several baffle configurations. Adding the center disk to a flow with the equatorial baffle and vanes at 45 degrees dropped the power required to be the same level as the configuration with the vanes at 30 degree. Adding the center disk lowered the amount of energy in the turbulent fluctuations when the poloidal vanes were at 45 degrees.

a run, a qualitative assessment of the turbulent energy can be obtained. The observed temperature increases agreed with the quantitive motor power measurements.

5.2 External Response Modes as an Indicator of Turbulence

The magnetic field outside the sphere is measured by 72 1-D external Hall sensors, 66 are arranged on a grid (11 longitudinal and 6 latitudinal coordinates) on the surface of the vessel and eight additional sensors along the motor shaft near the poles. We can take advantage of the fact that the applied seed field interacting with the sodium inside the sphere is being generated solely by currents in the coils outside the sphere. In addition, the measured external field is being generated solely by induced currents in the sodium inside the sphere. Thus, in both regions the magnetic field is the gradient of a scalar potential ($\mathbf{B} = -\nabla\Phi_m$) with $\nabla^2\Phi_m = 0$. The solution for the magnetic field is then

$$\Phi_m(r,\theta,\phi) = \sum_{\ell,m}\left(C_{\ell,m}r^{\ell} + D_{\ell,m}r^{-(\ell+1)}\right)Y_\ell^m(\theta,\phi). \tag{5.4}$$

The strength of the seed field is determined by knowing the geometry of the coils and measuring the applied current. Since we are looking at the applied field inside the vessel, Φ_m must approach 0 as r goes to 0 thus $D_{\ell,m} = 0$. So, the applied field inside the vessel can be expressed as

$$\begin{aligned}\mathbf{B}(r,\theta,\phi) &= -\nabla\Phi_m(r,\theta,\phi)\\ &= -\sum_{\ell,m} C_{\ell,m}r^{(\ell-1)}\left[\hat{\mathbf{r}}\left(\ell Y_\ell^m\right) + \hat{\theta}\left(\frac{\partial Y_\ell^m}{\partial\theta}\right) + \hat{\phi}\left(\frac{1}{\sin\theta}\frac{\partial Y_\ell^m}{\partial\theta}\right)\right].\end{aligned} \tag{5.5}$$

Similarly, if looking at the field outside the vessel, Φ_m must approach 0 as r goes to infinity thus $C_{\ell,m} = 0$. So the response field outside the vessel can be expressed as

$$\begin{aligned}\mathbf{B}(r,\theta,\phi) &= -\nabla\Phi_m(r,\theta,\phi)\\ &= \sum_{\ell,m} D_{\ell,m}r^{-(\ell+2)}\left[\hat{\mathbf{r}}\left((\ell+1)Y_\ell^m\right) - \hat{\theta}\left(\frac{\partial Y_\ell^m}{\partial\theta}\right) - \hat{\phi}\left(\frac{1}{\sin\theta}\frac{\partial Y_\ell^m}{\partial\theta}\right)\right].\end{aligned} \tag{5.6}$$

The probe coverage on the surface of the sphere allows for resolving $D_{\ell,m}$ up to $\ell = 7$, $m = 5$. These coefficients are solved for by using a truncated Singular Value Decomposition (SVD).

One of the recent achievements of the Madison Dynamo Experiment was the characterization of the largest detrimental eddies and an verification of their decrease after the installation of the equatorial baffle though the observed reduction of energy in specified response modes. [Kaplan, 2012]

In this section, a generalization of the method used by Kaplan [Kaplan et al., 2011] is presented. Instead of looking at the change in individual mode energies and to characterize the properties of the removed fluctuations, all the response mode energies are partitioned into two groups: expected and unexpected. The portion of the response mode energy that is in the expected modes allows us to evaluate the over all reduction of turbulence in the flow for different levels of constraints and vane orientations.

This method can be generalized to quantify the amount of turbulence in each baffle configuration tried. Referring to the Guant and Elsasser integral selection rules, when one applies a $\ell = 1$ or $\ell = 2$ seed field to an axisymmetric, purely t2s2 flow, the number of external response modes expected is very limited.

The magnetic energy in the applied and response modes is calculated by

$$\mathrm{E}_m = \frac{1}{2\mu_0} \int_V \mathbf{B}^2 \mathrm{d}V. \tag{5.7}$$

Plugging in the expanded form of $\mathbf{B}$ from 5.5 into this equation and recalling that the valid volume for the applied field is only inside the sphere ($0 < r < r_0$), the energy in the applied modes are

$$\mathrm{E}_l^m = \frac{\ell r_0^{2\ell+1}}{4\mu_0} C_{\ell,m}^2. \tag{5.8}$$

Plugging in the expanded form of $\mathbf{B}$ for the external response modes from 5.6 into the energy equation and recalling that the valid volume for the response modes is only outside the sphere ($r_0 < r < \infty$), the energy in the response modes are

$$\mathrm{E}_l^m = \frac{(\ell+1)}{2\mu_0 r_0^{2\ell+1}} D_{\ell,m}^2. \tag{5.9}$$

One observation when analyzing the allocation of energy in the external modes with an axial dipole applied is the large and unexpected transverse dipole response mode. This violates one of the Bullard-Gellman selection rules ($m_\alpha \pm m_\beta \pm m_\gamma = 0$).

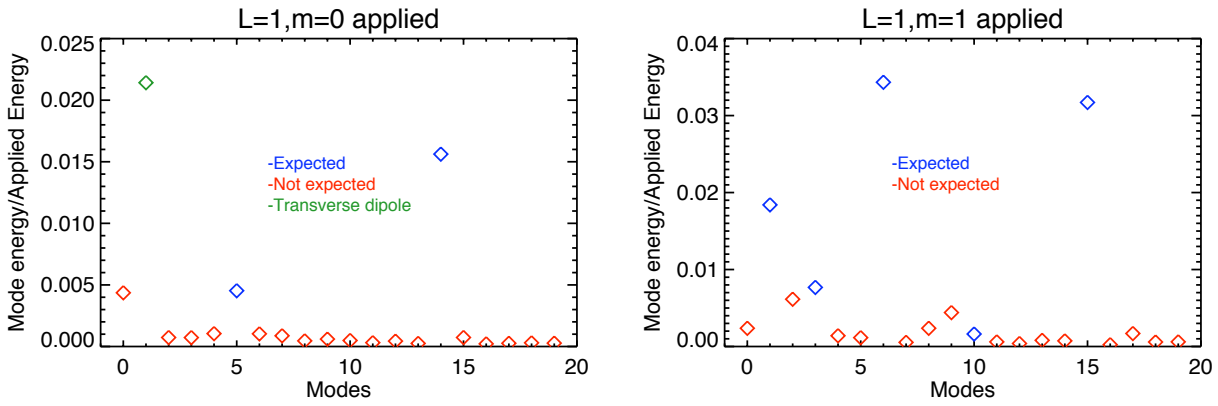

(a) Energy in External Response AD Applied

(b) Energy in External Response TD Applied

Figure 5.4 The energy in the response modes partitioned into expected (blue), unexpected (red), and unexplained S_1^1 (green): (a) The total energy in the each of the external response modes normalized to the amount of magnetic energy in the applied fields where the applied field is an axial dipole. (b) The total energy in the each of the external response modes normalized to the amount of magnetic energy in the applied fields where the applied field is a transverse dipole.

Shown in figure 5.4 is the energy in all of the response modes for a 1000 RPM flow with an equatorial baffle and the vanes at 45 degrees. In the figure the energy in the sine and cosine have been combined for the $m \geq 0$ modes. For the generalized mode analysis the energy in the response modes is split into two or thee categories depending on the applied field: 1. Expected external modes, 2. Unexpected $\ell = 1$, $m = 1$ mode, 3. Forbidden modes. All these measured mode energies are normalized to the energy in the applied mode in the volume of the sphere. An increase in energy in the allowed modes is evidence of an increased Rm indicating that the turbulent dissipation (β-effect) has been reduced. A significant amount of the response mode energy was observed in the $\ell = 1$, $m = 1$ mode when an axial dipole was applied. This mode can only exist due to a non-axisymmetric component to the flow. However, as turbulent dissipation is reduced and the flow pitch is optimized this $\ell = 1$, $m = 1$ field is amplified. For that reason it is put in a separate category for this analysis. The forbidden modes are produced by the seed field interacting with flows that are not ℓ=2 or flows that are not axisymmetric. An increase in the forbidden mode energy indicates that there was a relative increase in turbulent fluctuation levels.

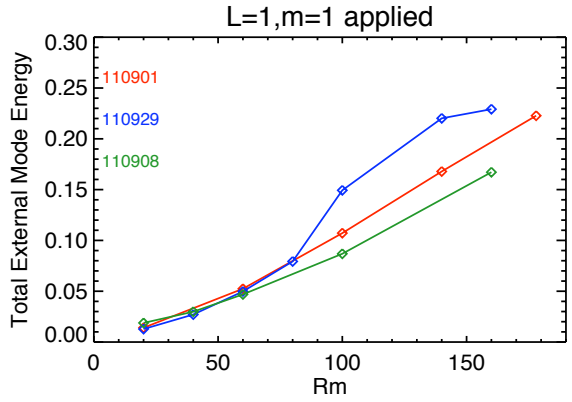

(a) Total Energy in External Response

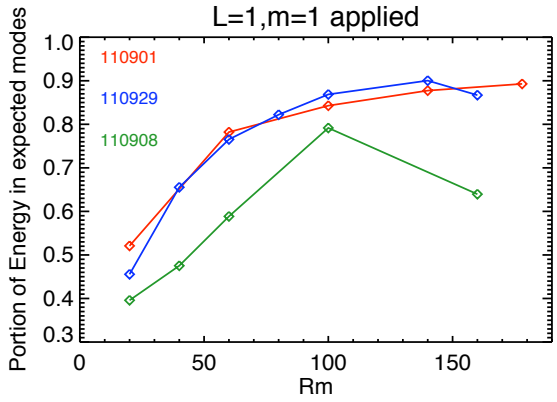

(b) Fraction of Response Energy in Expected Modes

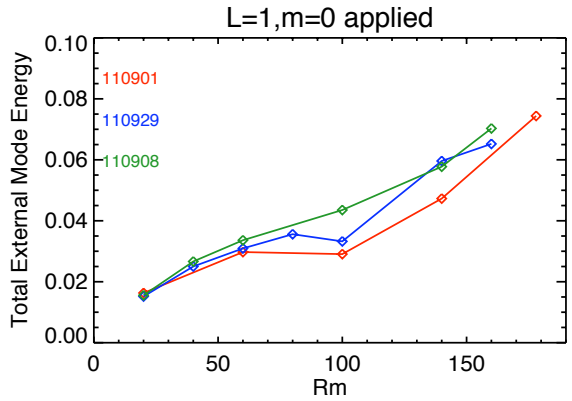

(c) Total Energy in External Response

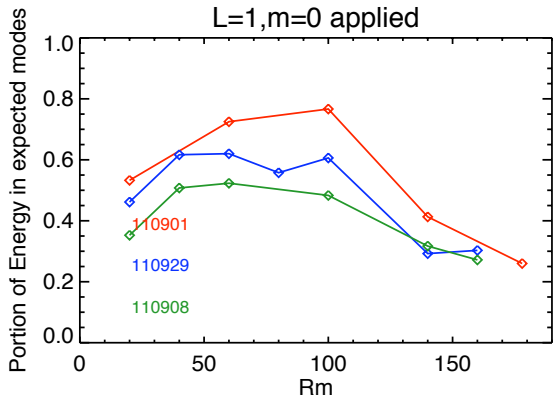

(d) Fraction of Response Energy in Expected Modes

Figure 5.5 Analyzing the energy in the response modes for three different poloidal vane orientations: 110901=30 degree, 110929=45 degree, 110908=60 degrees. (a) The total energy in all the of the external response modes (E_{resp}/E_{app}) where the applied field is a transverse dipole. (b) The percentage of the external response energy with the transverse dipole applied field that is in the expected modes according to the Bullard and Gellman selection rules. (c) The total energy in the all of the external response modes (E_{resp}/E_{app} except the S_1^1 response) where the applied field is an axial dipole. (d) The percentage of the external response energy (excluding the S_1^1) with the axial dipole applied field that is in the expected modes according to the Bullard and Gellman selection rules.

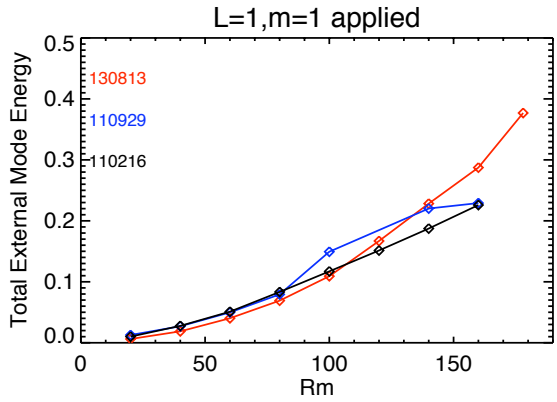

(a) Total Energy in External Response

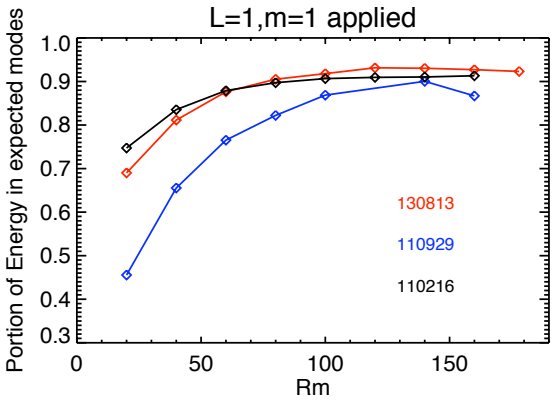

(b) Fraction of Response Energy in Expected Modes

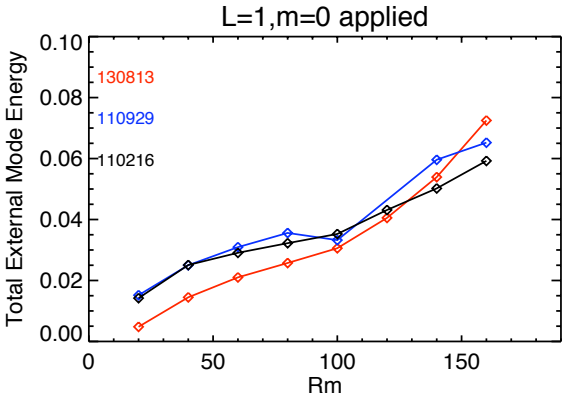

(c) Total Energy in External Response

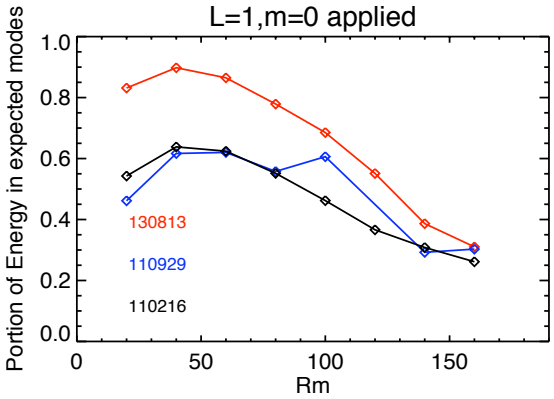

(d) Fraction of Response Energy in Expected Modes

Figure 5.6 Analyzing the energy in the response modes for adding more constraints to the flow: 110216=eq. baffle only, 110929=eq. baffle and vanes at 45 degrees, 130813=eq. baffle and center disk and vanes at 45 degrees. (a) The total energy in the all of the external response modes (E_{resp}/E_{app}) where the applied field is a transverse dipole. (b) The percentage of the external response energy with the transverse dipole applied field that is in the expected modes according to the Bullard and Gellman selection rules. (c) The total energy in the all of the external response modes (E_{resp}/E_{app} except the S_1^1 response) where the applied field is an axial dipole. (d) The percentage of the external response energy (excluding the S_1^1) with the axial dipole applied field that is in the expected modes according to the Bullard and Gellman selection rules.

From the Bullard and Gellman selection rules when an axial dipole ($\ell = 1$, $m = 0$) is applied, the only allowed external response modes are: S_ℓ^m=(S_3^0,S_5^0,S_7^0). The ($\ell = 1$, $m = 0$) mode is allowed in the selection rules but cannot exist due to a corollary to Cowling's anti-dynamo theorem (an axisymmetric flow cannot self-generate an axisymmetric field.) The existence of a large and diamagnetic (l=1,0) response was a significant discovery early on in the Madison Dynamo Experiment. And a corresponding reduction in this diamagnetic ($\ell = 1$,$m = 0$) field was observed with the addition of the equatorial baffle.

For the transverse-dipole ($\ell = 1$, $m = 1$) applied seed field the allowed modes are essentially all $m = 1$ modes. The energy partition plots are essentially looking at the m-spectrum of response mode energies. It should be noted that this partition of energies is how the t2s2 dynamo works. The applied $\ell = 1$, $m = 1$ mode interacts with the $\ell = 2$, $m = 0$ flow to produce $\ell = 2$, $m = 1$ magnetic modes, these induced modes interact with the $\ell = 2$, $m = 0$ flow to create a $\ell = 1$, $m = 1$ mode that amplifies the initial seed field. The probe coverage inside the sphere is not large enough to resolve the structure of any non-axisymmetric modes. Although there is a large amount of induced energy in the internal toroidal $\ell = 2$, $m = 1$ field, only poloidal modes can be measured by the external probe grid on the surface. Due to secondary interactions of the induced modes interacting with the t2s2 flow all $m = 1$ modes of some strength are expected to be measured on the surface.

We can see that with the addition of poloidal vanes, the amount of flux amplification was dependent on the poloidal vane angle. However, adding the vanes made the flow more turbulent. Despite the fact that the flows with the vanes at 45 degrees produced more magnetic flux than the runs with the vanes at 30 degrees, a larger fraction of the response mode energy was allocated to the allowed modes in the 30 degree case. Although the case with the vanes at 45 degrees produced more magnetic flux and a higher gain than the flow with just the equatorial baffle it also had more energy in unexpected modes.

There are three conclusions that can be made from analyzing the required motor power, the total amount of external mode energy produced, and the fraction of energy in the expected/unexpected modes:

1. The least turbulent flows produced were the flows with just the equatorial baffle and the flows with the equatorial baffle, poloidal vanes, and center disk.

2. Adding the poloidal vanes increased turbulence in the flow.

3. Rotating the poloidal vanes altered the $m = 1$ field amplification and turbulence levels.

4. Whatever turbulence that was added by the poloidal vanes is mitigated by the addition of the center disk.

5.3 Transverse Dipole Gain and Decay Time

The biggest measure used to benchmark the performance of a certain flow configuration is the transverse dipole gain. The two-vortex, t2s2 flow, is predicted to self-excite and produce a dipole field perpendicular to the rotation axis ($\ell = 1$, $m = 1$). The gain is a measurement of how much the flow amplifies a seed transverse dipole field. The gain is defined as

$$Gain = \frac{B_{applied} + cos(\delta) B_{response}}{B_{applied}} \tag{5.10}$$

where the δ is the phase between the applied and response S_1^1 mode. Shown in Figure 5.7 is the measured gain for three different flows all with the equatorial baffle installed and the vanes at three different angles (30°, 45°, and 60°) and the alignment of the response mode to the applied field. Shown in Figure 5.8 is the same measured gain and phase for three flow configurations: first with just the equatorial baffle, second with the equatorial baffle and the vanes at 45 degrees and finally a flow with the equatorial baffle, vanes at 45 degrees and the center disk. For all the flows at low rotation rates, the response transverse dipole mode was misaligned with the applied field and there was very little field amplification. As the speed of the flows were increased, the fields became co-aligned with the applied field and signifiant amplification was observed. From Figure 5.7, it can be seen that the flow with the vanes at 45 degrees saw the largest gain and saw the response mode co-align with the applied mode at the lowest Rm. This is indicates that the vanes at 45 degress produces a flow with a more optimum pitch. Also seen in the measured gain is a a rollover at higher rotation rates for the vanes at 45 degree flow.

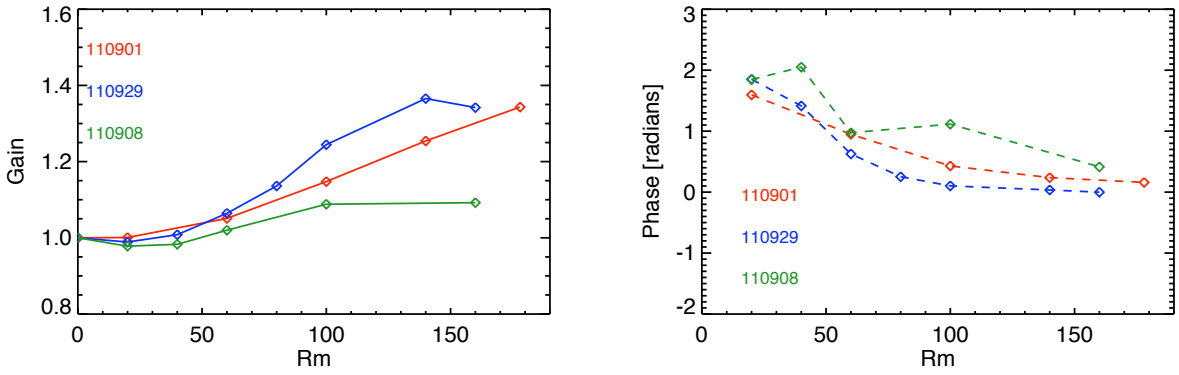

(a) S_1^1 Mode Gain

(b) S_1^1 Response Mode Phase

Figure 5.7 (a) Comparison of S_1^1 Gain vs Rm for three different poloidal vane angles: 110901-vanes at 30 degrees, 110929-vanes at 45 degrees, and 110908-vanes at 60 degrees. (b) The phase difference of the response S_1^1 to the applied seed S_1^1 mode vs Rm.

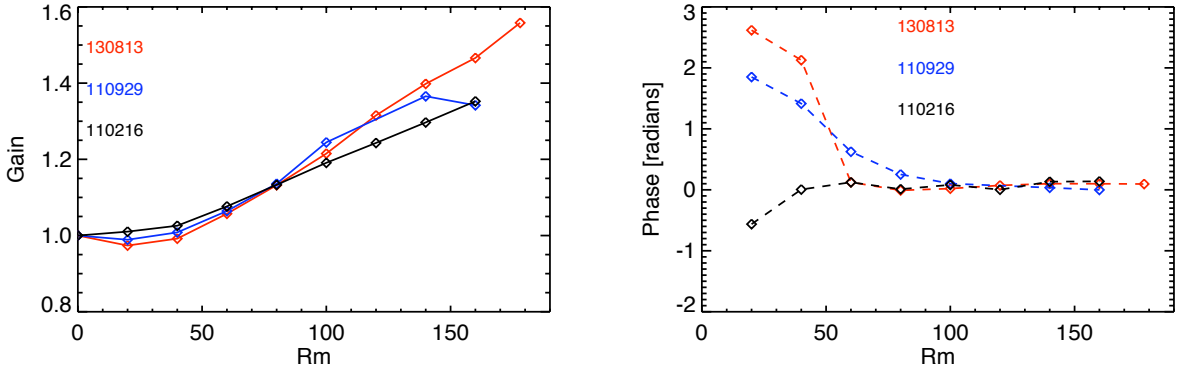

(a) S_1^1 Mode Gain

(b) S_1^1 Response Mode Phase

Figure 5.8 (a) Comparison of S_1^1 Gain vs Rm for three different baffle configurations: 110216-equatorial baffle only, 110929-equatorial baffle and vanes at 45 degrees, and 130813-equatorial baffle, vanes at 45 degrees, and the center disk. (b) The phase difference of the response S_1^1 to the applied seed S_1^1 mode vs Rm.

From Figure 5.8, it can be seen that with the addition of each new constraint to the flow, a larger measured gain was observed. Another important development was that the rollover in measured gain at higher rotation rate was not observed when the center disk was added. The additional turbulence created by the vanes at 45 degrees at higher rotation rates was efficiently suppressed with the center disk. The flow with the equatorial baffle, center disk, and poloidal vanes at 45 degrees produced the highest measured gain. At the maximum rotation rate of 1780 RPM the field strength of the response mode at the surface of the sphere was over 50% of the applied field strength.

Another interesting discovery was the consistent misalignment of the response mode at low rotation rates. For all of the flow configurations discussed above, the response mode was oriented in the same direction (approximately perpendicular to the applied field). In the equatorial baffle case shown in figure 5.8 the polarity of the applied field for the 110216 run was opposite than the other runs, so the physical orientation of the response mode at low RPM was the same for all other flow configurations.

Another method for determining the ability of a flow to produce field is to measure the decay time of the transverse dipole mode. To measure the decay rate the sodium is spun at a constant rate and the same transverse dipole field that was applied for the gain plots is pulsed at 0.2 Hz (2.5 seconds on, 2.5 seconds off). The response mode decays away exponentially. Taking the ensemble average of multiple decays an accurate decay time can be found.

The results from these decay time measurements can been seen in Figure 5.9. There was a drastic improvement to the decay rates of the completely unconstrained flows. In that case higher rotation rates just created more turbulence that shredded the magnetic fields enhancing the dissipation. As more constraints were added to the flow, a longer decay time was observed. However, no strong trend in the decay time was observed as the rotation rate was increased to maximum rotation rate.

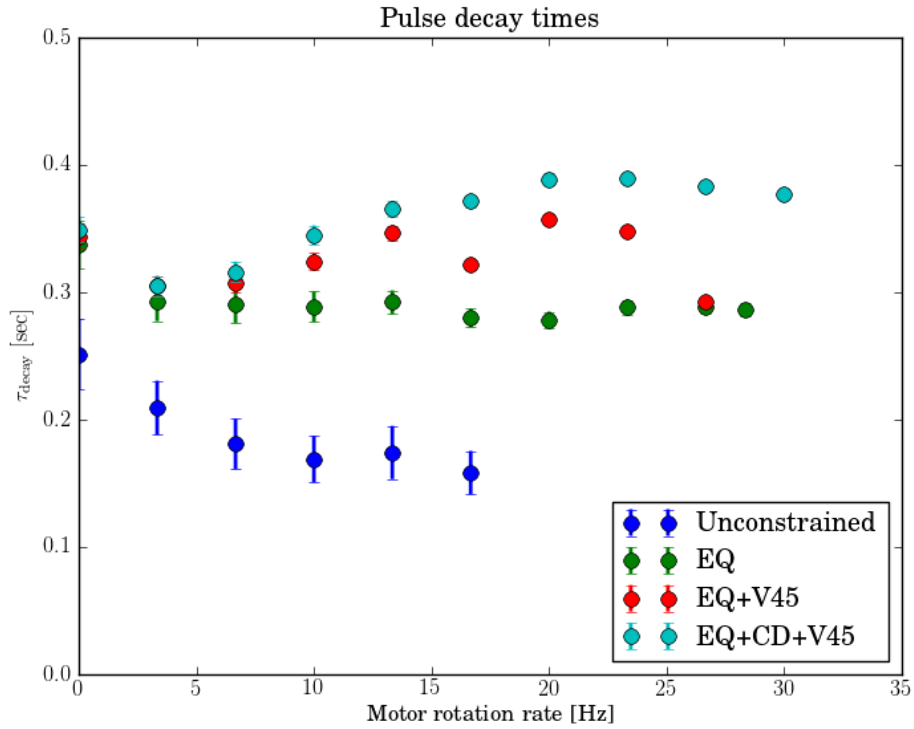

Figure 5.9 The measured decay times of the transverse dipole mode (S_1^{1c}) vs rotation rate for four different flow configurations. With the addition of each new flow constraint a longer decay time was observed.

5.4 Reduced Turbulent EMF Characterized

After the equatorial baffle and poloidal vanes were installed there was a significant improvement in the amplification of the magnetic field. The detrimental turbulent EMF was drastically reduced. A direct local measurement of the remaining turbulent EMF was obtained using the $\mathbf{V} \times \mathbf{B}$ probe described in section 3.4.3.

Shown in Figure 5.10 are the time traces of one component of the velocity and magnetic field. By crossing the fluctuating components of the measured velocity and magnetic fields, a mean turbulent EMF was found. Also shown in Figure 5.10 is the orientation of the measured turbulent EMF. The turbulent EMF was found to be nearly perpendicular to the mean magnetic field and anti-parallel to the mean current [Rahbarnia, 2012]. Recalling the assumed structure of the turbulent EMF from Section 2.6, it is found that the EMF is a β-effect. Thus, the effects of the large-scale fluctuations have been severely reduced and the effect of the remaining fluctuations is essentially a reduction to the effective conductivity of the flow.

5.5 Measuring the Large Induced Internal Field

The addition of baffles to the flow dramatically improved the amplification of a transverse dipole seed field. When an axial seed field is applied, there are three regions in the flow where a large response field is predicted to be induced. The 3D-equatorial array and the side arrays near the poles were placed so that they could measure these three predicted magnetic features. Figure 5.11 shows the average value of the toroidal field measured on one of the internal arrays near the pole for several different rotation rates. As the flow is spun at a higher rate, the differential rotation in the toroidal flow winds up the axial-directed seed field into a strong toroidal magnetic field (Ω-effect). Figure 5.12 shows the average value of the axially-directed field near the center of the vessel for several different rotation rates. The θ-directed probes near the center of the equatorial array measured the strong compression of the axially applied seed field. At the peak rotation rate, the maximum measured toroidal field is $\sim 3.5\mathrm{B}_{app}$ while the maximum measured poloidal field is

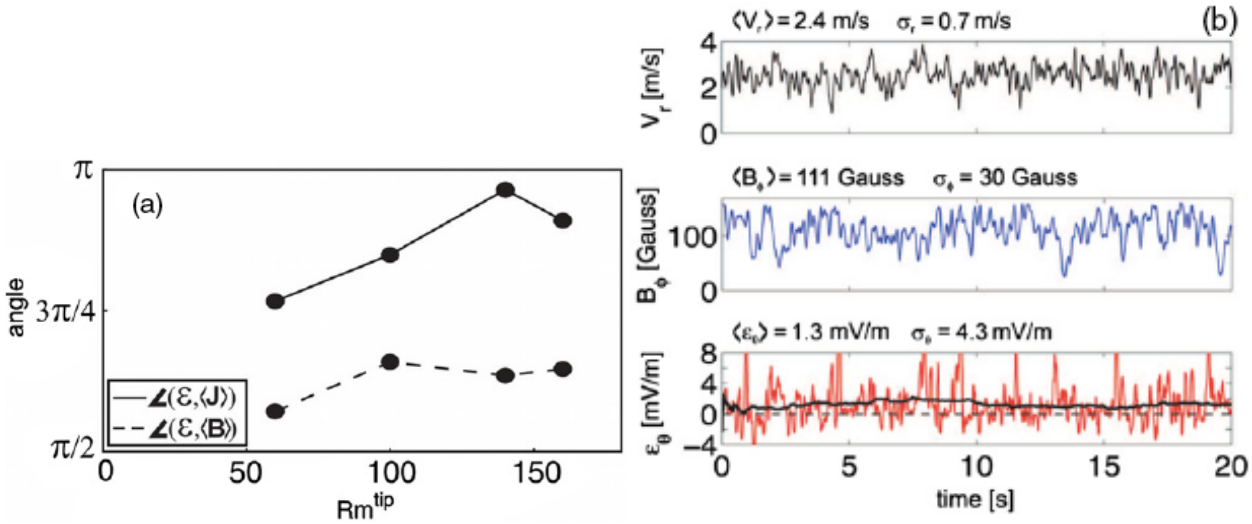

Figure 5.10 (a) The angle between the measured EMF and the mean component of the internal magnetic field and current. (b) Time traces of the v_r and B_ϕ that are used to compute the θ-component of the EMF. By measuring all three components of the velocity and magnetic field the magnitude and direction of the EMF can determined [Rahbarnia, 2012].

$\sim 15\mathrm{B}_{app}$. While these strong induced fields are significant, they are still smaller than the fields predicted by the kinematic solver described in Section 2.4.

The three dimensional internal arrays now measure very strong induced fields that approximate the values and structure from the kinematic prediction. However, observing the time series of the measured induced field shows large, non-gaussian fluctuations. Figure 5.13 shows the time series and the corresponding Probability Distribution Function (PDF) for an array of ϕ-directed probes near one of the poles. Data sets are typically two minutes long ($\sim 60,000$ magnetic data samples per probe) to provide small uncertainty in the measurement. Figure 5.14 shows the time series and the corresponding PDF for an array of θ-directed probes near the center of the vessel measuring the compression of the axially-applied seed field. There are strong non-gaussian fluctuations along the whole array. These fluctuations are highly correlated. However, the strength of the non-fluctuating component of the field falls off rapidly away from the center of the vessel. To evaluate the global structure of the non-fluctuating magnetic field in the presence of these non-gaussian fluctuations, the stationary field is designated as the most probable field (the peak of the PDF), not the mean field.

5.6 Asymmetries in the Induced Field

Analysis of the motor power and of the energy distribution in the external response modes have indicated that detrimental fluctuations in the flow have been greatly reduced. However, when an axial dipole seed field is applied, there are two asymmetric properties of the induced field that cannot be explained. The first asymmetry is a strong fluctuating transverse dipole ($\ell = 1$, $m = 1$) response mode that is measured. According to the Gaunt and Elsasser selection rules described in section 2.2, applying a $m = 0$ seed field to a $m = 0$ flow should only excite a $m = 0$ response field. So, all of the response modes should be axisymmetric.

However, a large fraction of the response mode energy is in fluctuating transverse dipole mode. Figure 5.16 shows how the measured S_1^1 response mode varies with rotation rate. Analyzing the frequency spectrum of this unexpected mode reveals that the mode seems to oscillate around 0.5 Hz and the frequency of oscillation seems to increase with rotation rate. A PDF of the phase of the

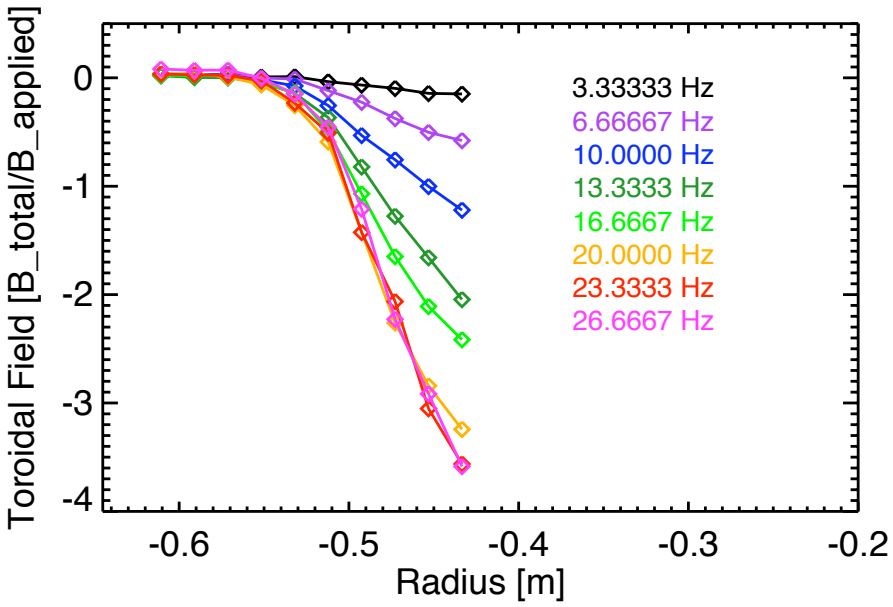

Figure 5.11 The induced toroidal field in the hall array closest to the poles. The applied seed field is perpendicular to the probes. The amplitude and gradient of the induced field increases with rotation rate.

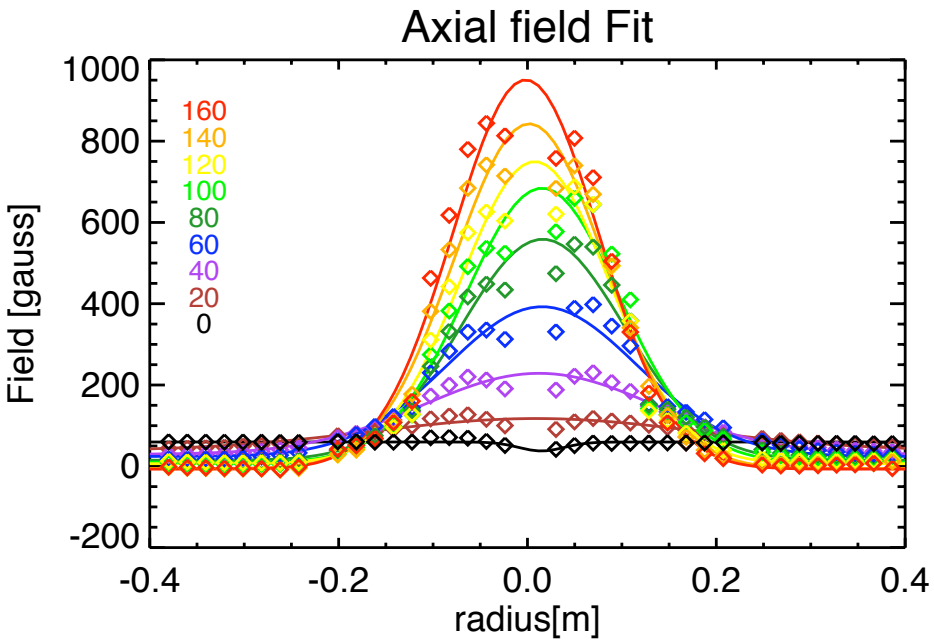

Figure 5.12 The measured axial field in the equatorial hall array. The seed field is an axial dipole with an amplitude of 60 Gauss at the equator. When the flow is stationary the measured axial field is essentially uniform across the array. At higher rotation rates the axial field at the outer radii is swept inward by the strong poloidal flow compressing the flux in the center. At maximum rotation rates the peak field measured in the center is 15 times the applied field.

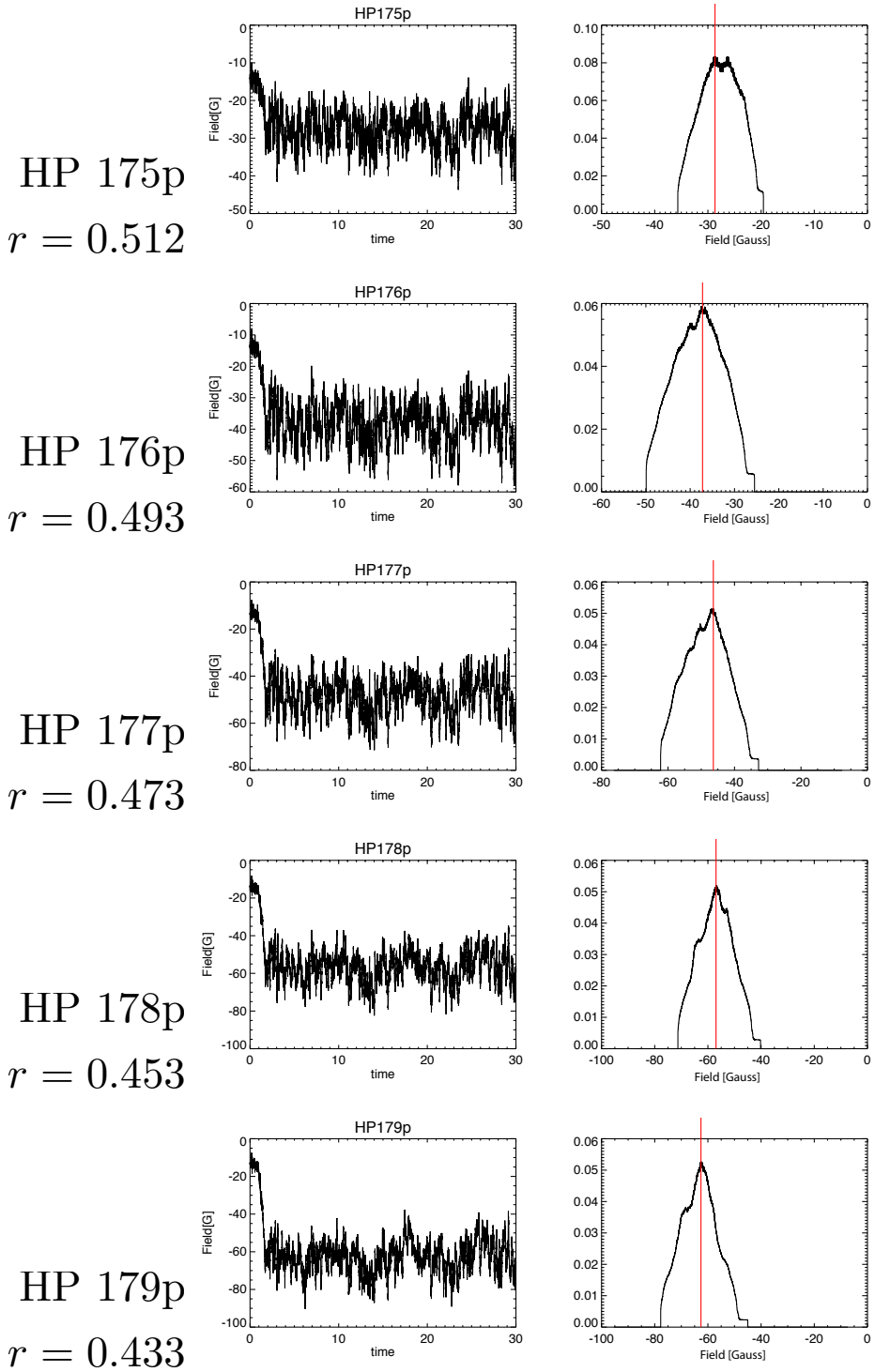

Figure 5.13 The time series for ϕ-directed probes for one of the internal arrays located near the poles. When the axial seed field is turned on, the toroidal windup in the field is measured. The corresponding PDFs for the toroidal probes are also shown. The area under each PDF curve totals to 1. The most probable value of the field is used to fit the internal data.

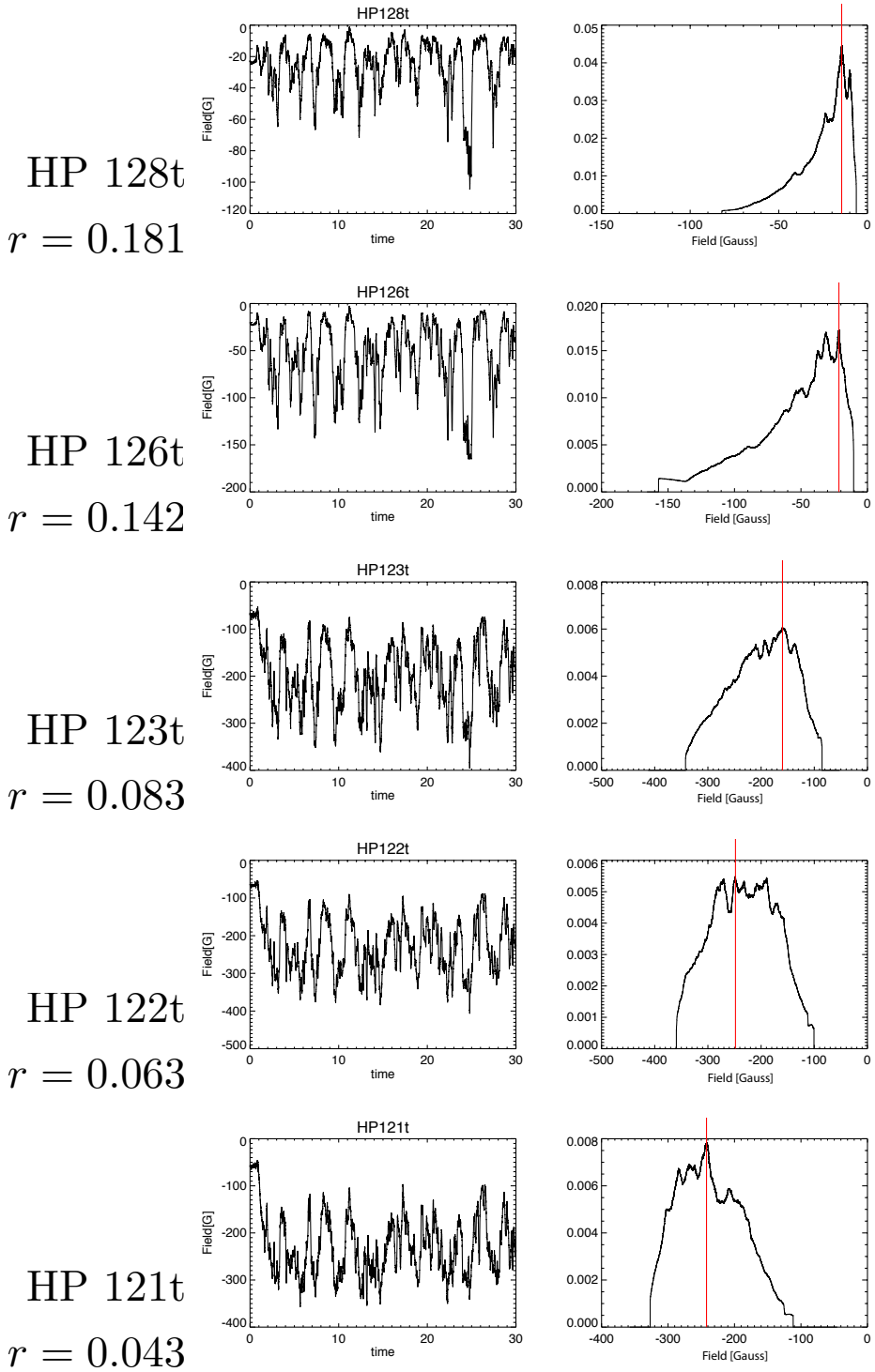

Figure 5.14 The time series for θ-directed probes in the equatorial array near the center of the vessel. When the axial seed field is turned, the poloidal flow compresses the seed field toward the center of the device where a large field is measured. The corresponding PDFs for the axial probes are also shown. The area under each PDF curve totals to 1. The most probable value of the field is used to fit the internal data.

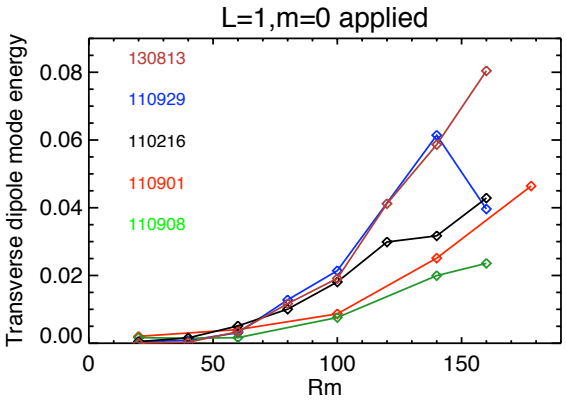

Figure 5.15 The amount of energy in the large and unexpected S_1^1 response mode (E_{resp}/E_{app}) when an axial dipole field is applied for multiple flow configurations: 130813-equatorial baffle, poloidal vanes at 45, center disk. 110901-equatorial baffle and poloidal vanes at 30. 110929-equatorial baffle and poloidal vanes at 45. 110908-equatorial baffle and poloidal vanes at 60. 110216-just the equatorial baffle. The energy in the unexpected mode increases with the amount of constraints added to the flow.

induced mode ($\tan^{-1}(S_1^{1s}/S_1^{1c})$) was computed for when the energy in the mode was large. It was found that the unexpected S_1^1 response mode is oriented predominately in the cosine direction. The source of this m=1 response mode has not been identified. The addition of more constraints to the flow reduced the turbulent fluctuations in the flow including the wobbling of the shear layer (t_1^1) which is one of the candidates for the source of the induced S_1^1 response. However, as more baffles were added to the flow, the observed mode got larger not smaller. This can be seen in Figure 5.15. This figure shows that adding constraints to the flow increased the energy in the S_1^1 mode. It must be noted that this transverse dipole mode is the magnetic eigenmode for the t2s2 flow. The source of this $m = 1$ might not have increased with more flow constraints, rather the optimized flow may be more conducive to amplifying it.

A second asymmetry observed in the mean induced field is the toroidal windup at the equator is not axisymmetric. The differential rotation in the toroidal flow between the two impellers winds up a axial seed field in the toroidal direction. The amplitude of this windup should not depend on the ϕ-position. In figure 5.17 a dataset was taken with a transverse dipole field seed field applied to a stationary flow. This applied field should is nearly uniform along the equator and the B_ϕ probes confirm that. This was done just to ensure that the B_ϕ probes along the equatorial array were positioned and working properly. The next data set was with an axial seed field applied to a flow rotating at 600 RPM. A large, axisymmetric toroidal windup is expected. A large measured toroidal field is measured but it is not axisymmetric. This asymmetry was observed for multiple baffle configurations. Usually the toroidal field on the top side of the equatorial probe (right hand side on graph) was larger than the bottom side but sometimes the larger field was on the bottom side. The side of the probe with the stronger measured field did not depend on rotation rate or the applied field polarity. The axial dipole and axial quadruple applied fields were used prior to these data sets to ensure that the equatorial array was aligned in the proper direction and position.

No significant correlation was found when the time series of both the internal field data and the fluctuating transverse dipole response mode were analyzed. The unidentified asymmetric flow modes that are causing them do not appear to be related.

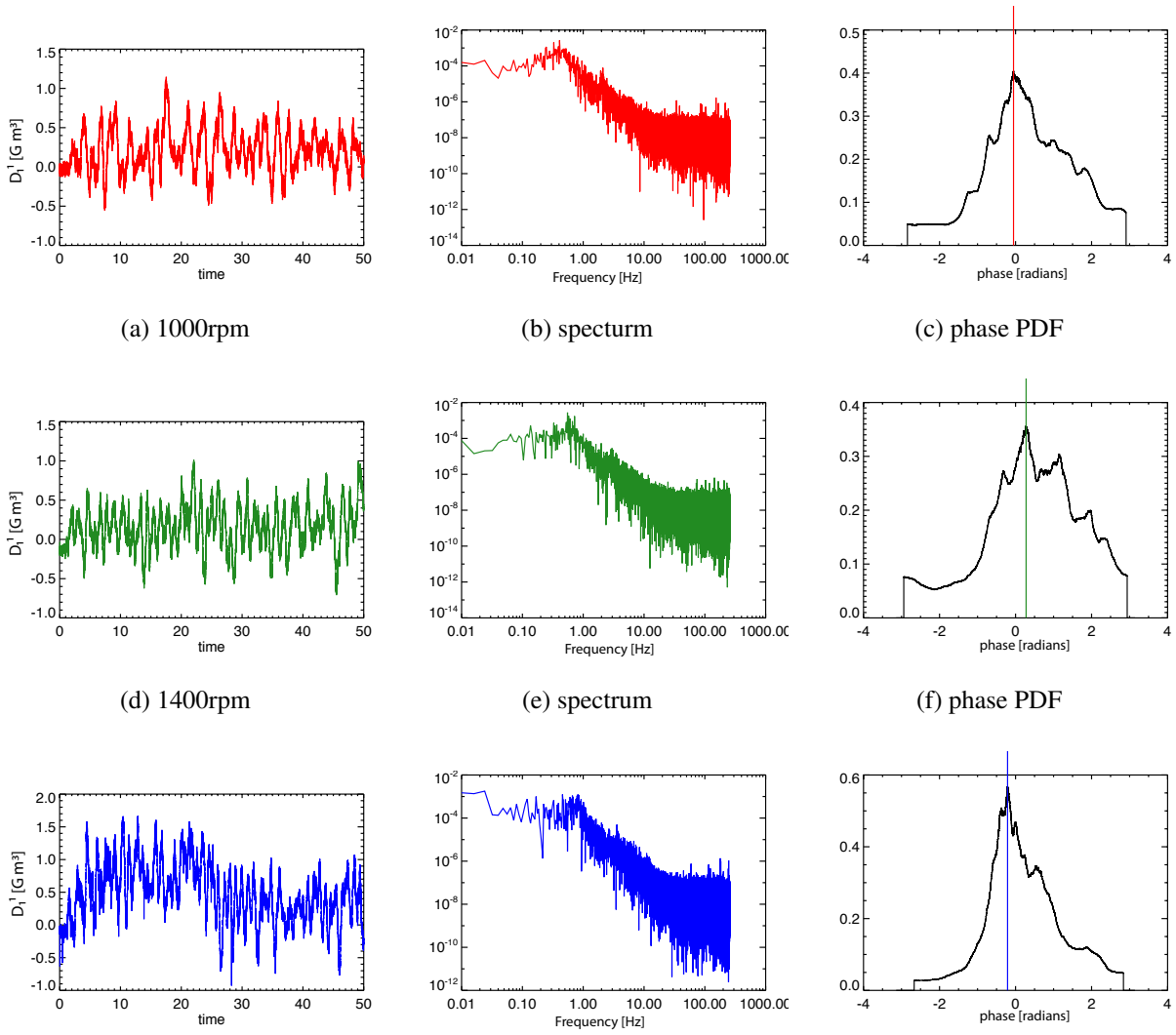

(a) 1000rpm (b) specturm (c) phase PDF

(d) 1400rpm (e) spectrum (f) phase PDF

(g) 1780rpm (h) spectrum (i) phase PDF

Figure 5.16 (a,d,g) The time series for the measured S_1^{1c} when an axial dipole is applied to three different rotation rates. The presence of this large response mode cannot be explained through laminar selection rules. (b,e,h) The corresponding frequency spectrum showing the dominate energy in the mode fluctuates at around 0.5 Hz. (c,f,i) The corresponding PDFs of the phase of the S_1^1 mode during large bursts. The area under each PDF curve totals to 1. There is more energy in the S_1^{1c} component than the S_1^{1s} component.

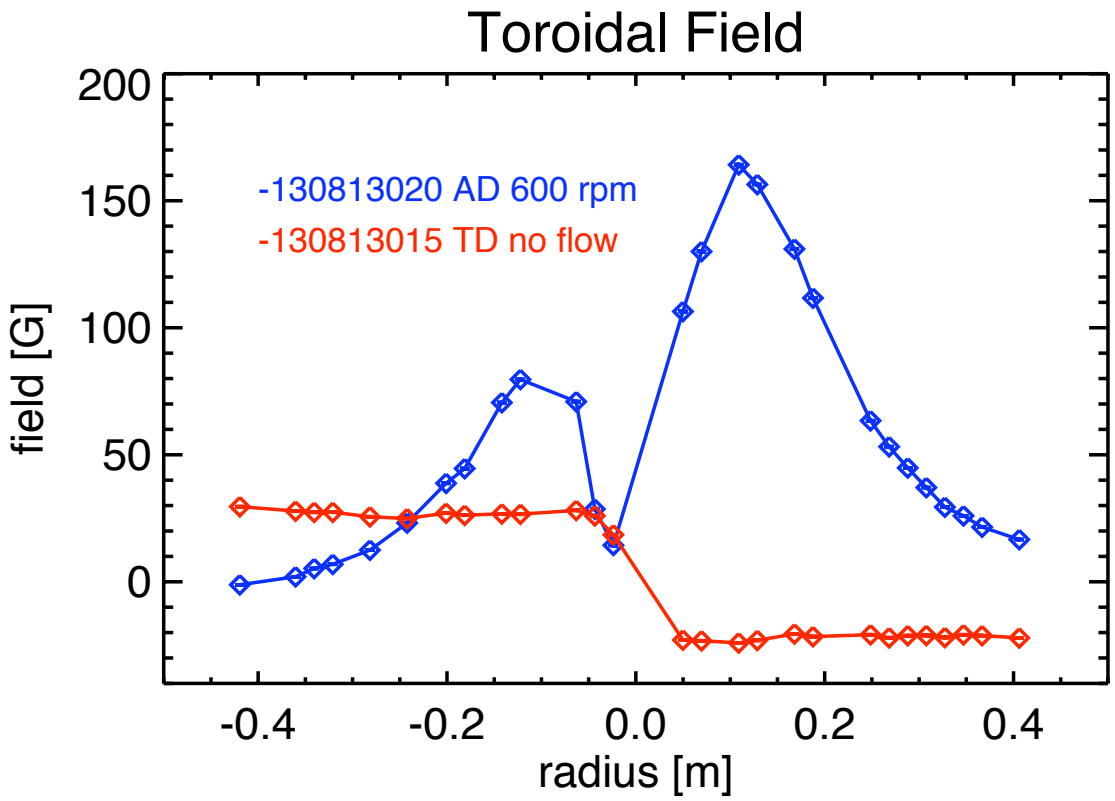

Figure 5.17 A plot of the ϕ-directed field along the equator for two data sets. A transverse dipole applied field to a stationary flow shows the probes measuring the expected nearly uniform field in the toroidal direction (red). An axial dipole field is applied to a 600 RPM flow, the induced toroidal field is not symmetric (blue). The toroidal field should go to zero at the origin by definition.

5.7 Fitting the Internal Field

All of the individual internal hall array dip tubes are located at one longitudinal position (ϕ=1.963) while the equatorial internal array is located at ϕ=0.7854 and ϕ=3.927 (the ϕ coordinate changes when passing through the origin). This probe coverage is not enough to resolve the global structure of internal $m \neq 0$ fields. However, in the case with an axial-dipole applied field, the mean field response, that is predominately axisymmetric, can be fit with a few spherical harmonics.

Fitting the internal field is done with a cubic spline interpolation. Due to the limited probe coverage in the azimuthal direction, only axisymmetric (m=0) fields can be resolved. Referring to the selection rules described in an earlier section, applying an axisymmetric seed field to an axisymmetric flow should produce an axisymmetric response. For the toroidal field the the end spline points of the radial profile at the origin and at the outer wall are zero. For the poloidal radial profiles the end spline points are zero at the origin but the edge is adjusted to match the external mode values measured with the set of external sensors. The internal field was fit multiple times with different numbers of splines and harmonics. The best fit was determined by minimizing a reduced χ^2 with extra weighting added to data points measuring large fields (to ensure the large induced points were captured in the fit) and with an added cost function that penalizes the total amount of magnetic energy used in the fit (to removes unrealistic gradients). We define

$$\chi^2_{fit} = \frac{1}{N}\sum_{i=1}^{n} \frac{(B_m[i] - B_a[i])^2}{\sigma[i]^2} \cdot W[i] + E_{cost} \tag{5.11}$$

where

$$W[i] = 1/2 + 1/2 \cdot \frac{|B_m[i]|}{\overline{|B_m|}},$$
$$N = n - n_{fit},$$
$$E_{cost} = scale \cdot \int_V \frac{B^2}{2\mu_0} \mathrm{d}V.$$

Figure 5.18 shows that both the internal toroidal and poloidal fields were best fit with just two harmonics ($\ell = 1$, $m = 0$ and $\ell = 3$, $m = 0$). The existence of a $\ell = 5$, $m = 0$ mode is expected

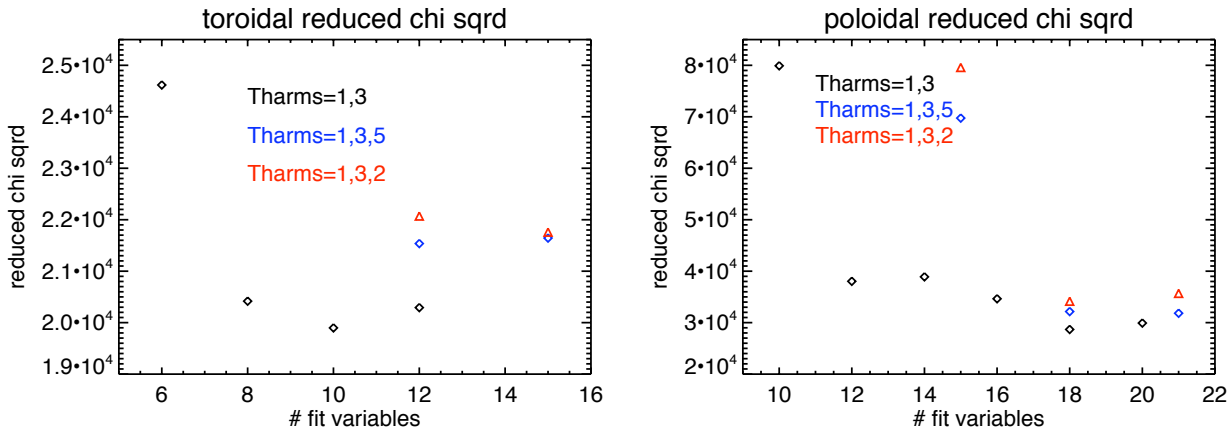

Figure 5.18 The reduced Chi squared with energy cost function for the (a) toroidal data and (b) poloidal data. The best fit of the both the poloidal and toroidal data was obtained using just two modes ℓ=1,3.

and observed in the response external modes. However, Its internal amplitude is not large enough and the probe coverage is not dense enough to cause adding $\ell = 5$vortex to improve the fit.

Figure 5.19 shows how well the fit matches the measured poloidal field from a 1000 RPM dataset. The poloidal fit is constructed with two harmonics where the radial profiles of those harmonics have 9 non-zero spline points (18 free variables). The fit accurately captures the strong field compression ($15\mathrm{B}_{app}$) near the center of the vessel. The Figure 5.20 shows how well the fit matches the measured toroidal field from the same 1000 RPM dataset. The toroidal fit is constructed with two harmonics where the radial profiles of those harmonics have 5 non-zero spline points (10 free variables). The fit matches the toroidal windup near the center of the vessel ($3\mathrm{B}_{app}$) and the toroidal windup near the poles ($3.5\mathrm{B}_{app}$). It should be noted that the internal magnetic field is very symmetric about the equator. Initial runs of the experiment with unconstrained flows resulted in flows that had a great deal of asymmetry (see Figure 1.5).

With this large induced magnetic field measured, the question can be asked if the experiment is still in the kinematic regime where the magnetic field is too weak to affect the flow. The total energy in the magnetic fields for the fits presented here is $\sim$100 Joules. From surveying the LDV water data and CFD flow profiles at 1000 rpm the expected energy in the flow is $\sim$2000 Joules. The magnetic energy is still a small portion (5%) of the flow energy. There is a small but measurable increase in motor power when an axial dipole field is applied. The strong axial field compressed at the center is causing extra force to be used to drive the flow. However, the measured response field on all the probes depends linearly on the strength of the seed field. If the field was strong enough to have a back-reaction and modify the flow a non-linear dependence on the strength of the applied field should be observed.

The next question that can be addressed is: what information about the velocity flow can we infer from the measured response field? As was just shown in this section, the internal field is best fit with just two harmonics. One implication of this result is that the internal magnetic data only provides enough information to infer the magnitude and structure of the largest and most dominate flow mode ($t_2(r), s_2(r)$). The effects of the next important mean velocity modes (most likely $t_4(r), s_4(r)$) are not large enough to be resolved in the internal magnetic diagnostics.

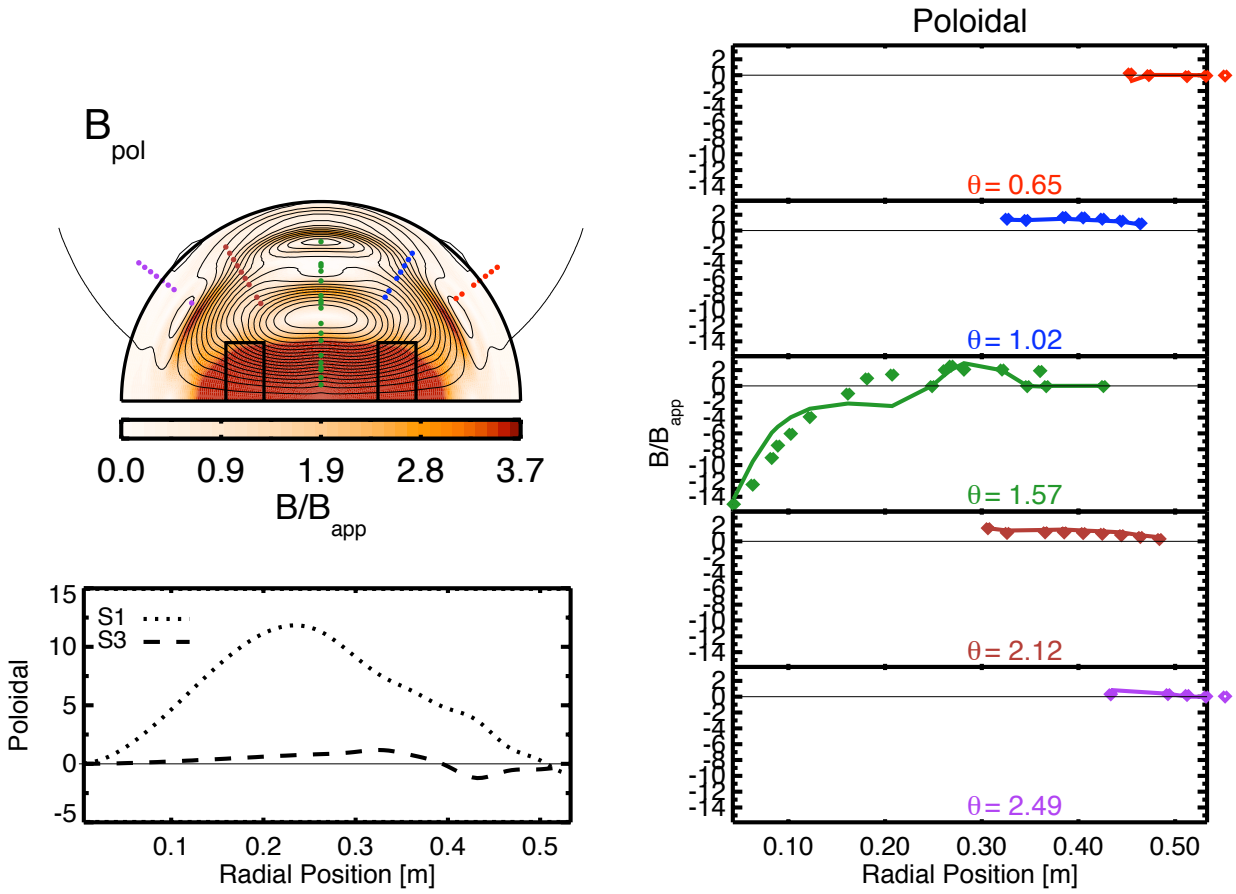

Figure 5.19 The internal poloidal magnetic field is fit with two spherical harmonics. The radial profiles of the two harmonics are shown. The internal poloidal field measurements are indicated by dots and the field produced by the fit at the measurement points is indicated by the solid line.

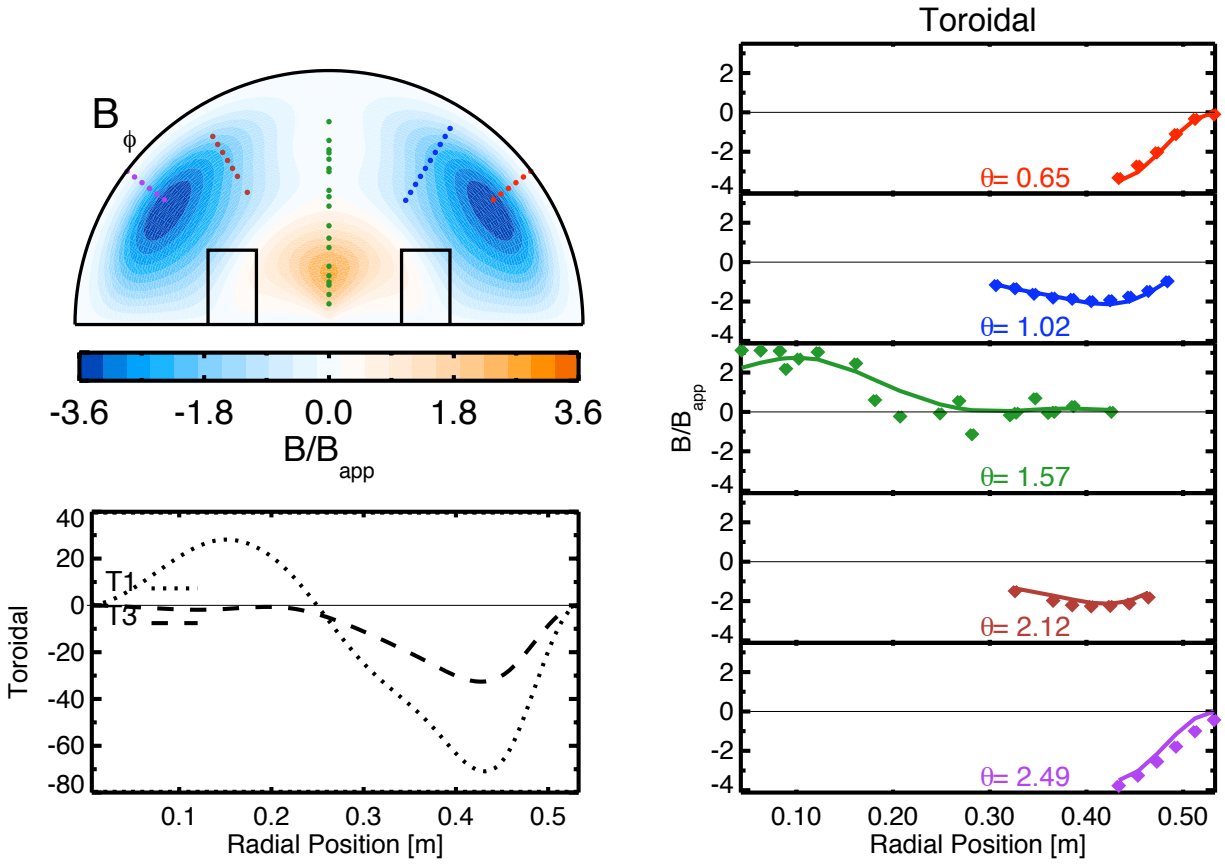

Figure 5.20 The internal toroidal magnetic field fit with two spherical harmonics. The radial profiles of the two harmonics are shown. The internal toroidal field measurements are indicated by dots and the field produced by the fit at the measurement points is indicated by the solid line.

Chapter 6

Velocity Inversion

6.1 Velocimetry

This chapter describes an inversion method used to determine the effective mean flow in the experiment. The inversion process involves probing a steady flow with a seed magnetic field, the induced field generated by the seed field interacting with the flowing sodium is measured on the internal probe arrays and on the surface of the vessel. The effective flow in the experiment can be determined by comparing the magnetic data with fields generated by the predictive kinematic solver described in Section 2.4. The method of using a measured magnetic field induced by a flowing conductive metal to infer the structure of the flow has been performed previously ([Baumgartl et al., 1993] and [Stefani and Gerbeth, 1999]). Initial attempts to perform an inversion on the magnetic field produced by the unconstrained flow were not possible due to a significant portion of the mean induced fields were generated by the turbulent EMF (see section 1.4).

From the reconstruction of the internal field in Section 5.7, we know the internal field now closely resembles the predicted field. Also, the best fit to the data was with just two harmonics ($\ell = 1, 3$). This implies that the effective flow generating the mean internal field is predominately $t_2 s_2$. The addition of constraints to the flow has greatly reduced the effect of fluctuations on the steady-state magnetic field. The inversion of the measured magnetic field to infer the structure of the flow is now possible.

6.2 Velocity Inversion Technique

The first method that was attempted to determine the velocity profiles from the magnetic field measurements was done by severely truncating the number of interaction terms in equation (2.13) (2.14) so that only ℓ=1,m=0 terms were kept. Once this is done, the measured S_1^0 and T_1^0 response modes fitted with cubic splines shown in section 5.7 can be used to solve for the s_2^0 and t_s^0 flow profiles analytically. This inversion process resulted in flow profiles that were approximately correct but failed to accurately return known flows in test cases. It seems truncating the induction equation to exclude the ℓ=3 modes results in an inaccurate velocity flow. More details on this inversion method are in Appendix A

To solve for the flow, we first start with a test two vortex flow that only depends on six variables (3 poloidal, 3 toroidal)

$$s_2^0(r) = a_p r^2 e^{\frac{-\delta}{r}} e^{\frac{(r-p_p)^2}{w_p^2}} e^{\frac{-\delta}{r_0-r}} \tag{6.1}$$

$$t_2^0(r) = a_t r^2 e^{\frac{-\delta}{r}} e^{\frac{(r-p_t)^2}{w_t^2}} e^{\frac{-\delta}{r_0-r}}. \tag{6.2}$$

The assumption that the flow is predominately $t_2 s_2$ is strengthened by the fact that the external response modes (which have good resolution up to $\ell = 7$, $m = 5$) show almost all the external magnetic energy is in modes generated by ℓ=2 flows.

These radial profiles are singularly peaked profiles that closely resemble the ideal profiles presented by Dudley and James [Dudley and James, 1989] . However, the 3 variables in each profile allow for the adjustment of amplitude, position of the peak, and the width of the peak. The exponentials with the δ terms force the radial profiles to be 0 at the origin to prevent unphysical flows and force the poloidal profile to be zero on the boundary (no flow escaping the sphere). These 3-variable profiles along with the eigenvalue solver were used by Forest, O'Connel et. al. to determine an optimized t2s2 flow that had an even lower Rm_{crit} than the Dudley and James profile [Forest et al., 2002].

The inversion routine starts by taking this test two-vortex flow and running it through the predictive solver with the applied field input being the seed field that was applied to the experiment. The resulting predicted field is then compared to the measured field at each internal data point

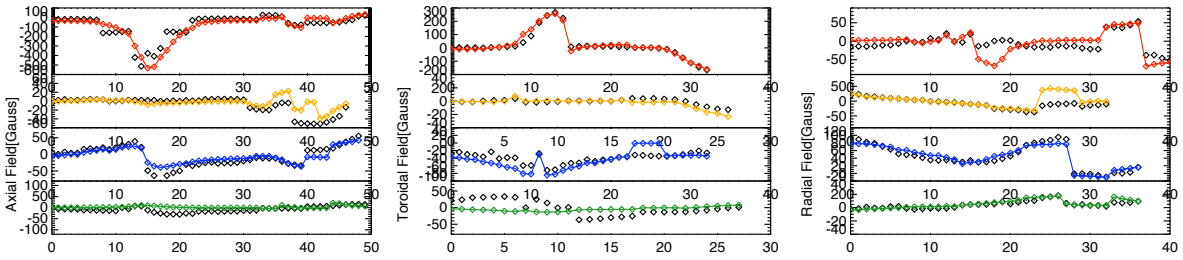

(a) B_θ probes (b) B_ϕ probes (c) B_r probes

Figure 6.1 The strength of the magnetic field measured on each internal probe in the experiment vs the predicted field generated by the inversion routine generated velocity field for four 1000 RPM datasets with different applied field configurations: axial dipole-red, axial quadrupole-orange, transverse dipole-blue, transverse quadrupole-green.

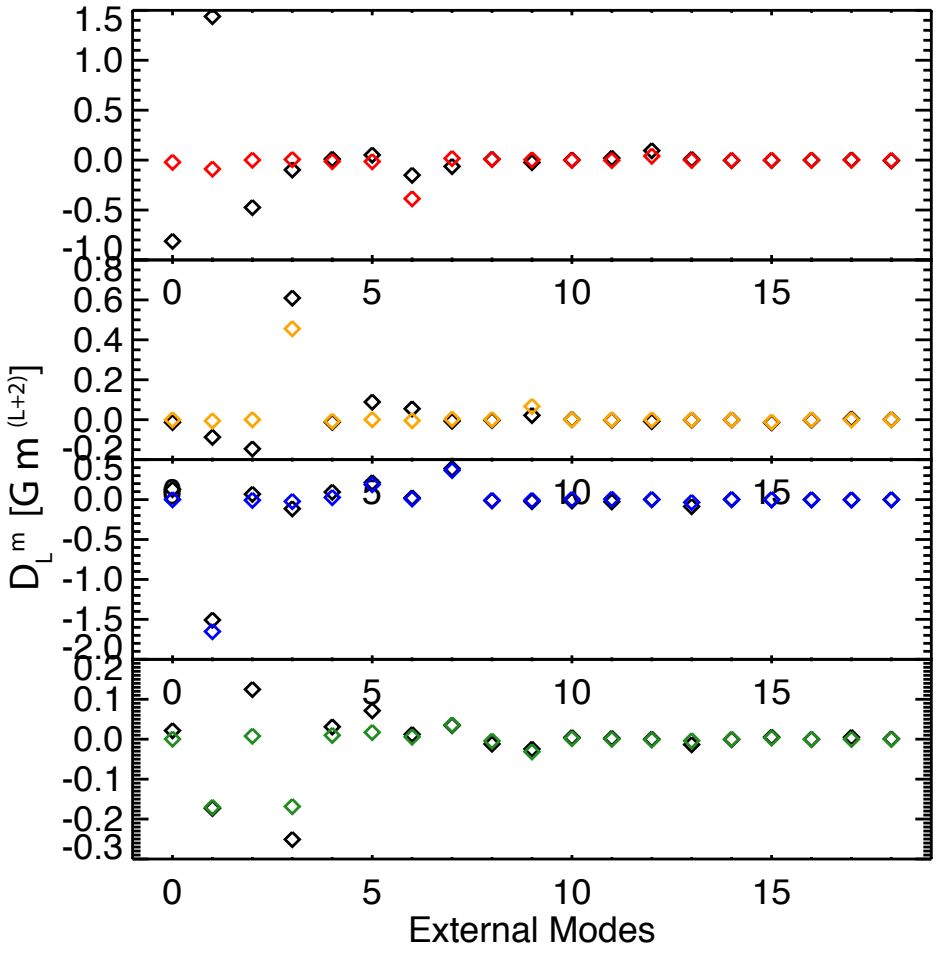

Figure 6.2 The strength of the mean component of the external modes (D_ℓ^m) measured on the surface of the sphere vs the predicted mode strength generated by the inversion routine. Shown for four 1000 RPM datasets with different applied field configurations: axial dipole-red, axial quadrupole-orange, transverse dipole-blue, transverse quadrupole-green.

and with the strength of the external modes. Adjustments to the six variables are done and the process is repeated. The determination of the variables by minimizing the difference between the predicted field and the measured field is performed by amoeba, a multidimensional function minimization routine using the downhill simplex method [Nelder and Mead, 1965] and [Press, 1992]. A cost function that penalizes high kinetic flow energy was added to remove unrealistic velocity fields. The use of a kinetic energy cost function in an inversion process has been used previously by [Stefani and Gerbeth, 2000]. Here, we use

$$\chi^2_{fit} = \sum_{i=1}^{n} \frac{(B_m[i] - B_a[i])^2}{\sigma[i]^2} \cdot W[i] \cdot \left(1.0 + E_{cost}\right) \tag{6.3}$$

where

$$E_{cost} = \frac{1}{10000\mathrm{J}} \int_V \frac{\mathbf{v}^2}{2\rho} \mathrm{d}V$$

where $W[i]$ is extra weighting given to a few specified internal probes that measure large induced fields in the axial dipole data sets and extra weighting given to response modes. $W[i] = 1.0$ for all internal magnetic probes except $W[i] = 10$ for 3 θ-directed probes closest to the center and $W[i] = 500$ for two largest ϕ-directed probes. $W[i] = 500$ for all the external modes except $W[i] = 1500$ given to the S_1^{1c} response mode (measured gain). By analyzing the velocity profiles obtained from the CFD simulations and the LDV water experiments energy in these effective flow is expected to be approximately 1500-2000 Joules. The cost function simply removes high-energy, sharply-peaked profiles and speeds up the time it take amoeba to converge.

To improve the fit, four data sets are used with four different applied field configurations ($S_{applied}$=S_1^0, S_1^1, S_2^0, S_2^1). The predictive code is also run for the four applied field configurations. Shown in Figure 6.1 is the measured field from four data sets with different applied field configurations and the field produced by the effective flow from the inversion process. Figure 6.2 shows the strength of the mean component of the external modes measured on the surface of the sphere for the four data sets vs the predicted mode strength generated by the effective flow obtained through the inversion routine.

The resulting effective velocity field from the inversion process can be seen in Figure 6.3. The velocity had a total kinetic flow energy of 1229 Joules and $Rm = 29$. It should be noted

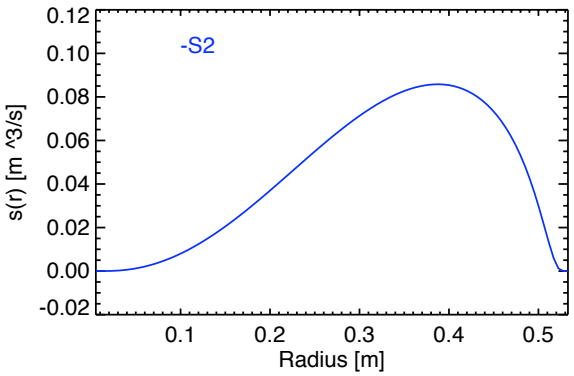

(a) Poloidal Radial Profile

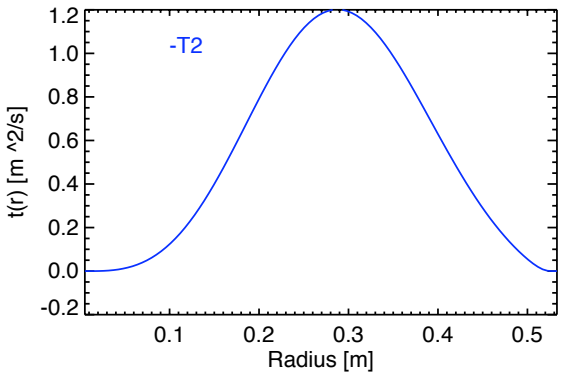

(b) Toroidal Radial Profile

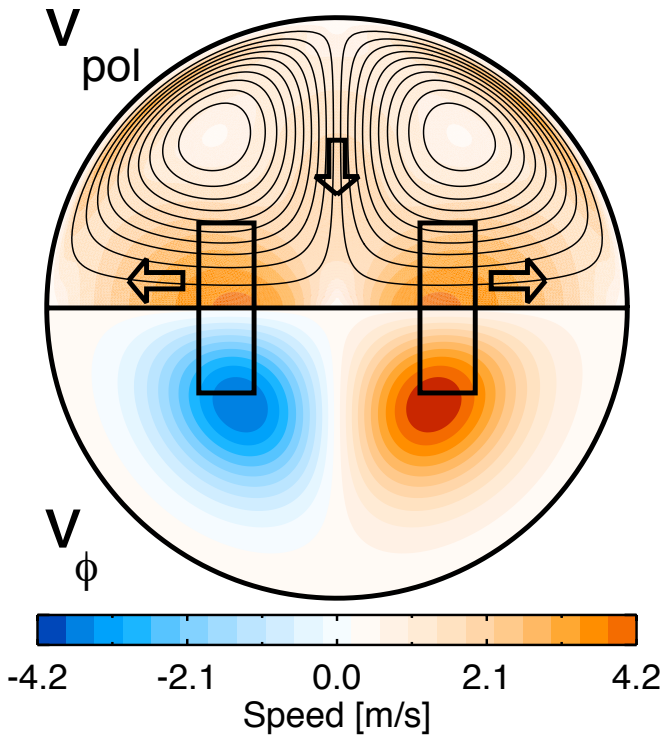

(c) Velocity Contour

Figure 6.3 (a) The poloidal and (b) the toroidal radial profiles obtained from the velocity inversion routine of the 1000 RPM datasets. (c) The corresponding contour plot of the velocity field created by the poloidal and toroidal profiles.

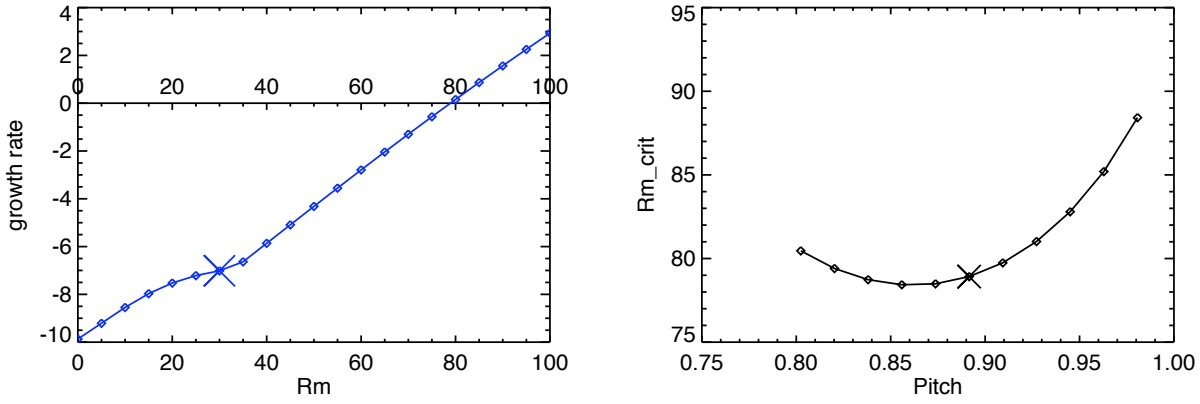

(a) Growth Rate vs Rm

(b) Rm_{crit} vs Pitch

Figure 6.4 (a) The predicted growth rate, in units of $[\tau_\sigma]^{-1}$, of the fastest growing (least damped) mode vs Rm for the velocity profiles obtained from the inversion results. (b) The corresponding Rm_{crit} as the pitch of the flow is varied. The velocity field that best replicated the real data had Rm=29 and Pitch=0.9.

that the velocity field is determined by what the magnetic field "sees" when it interacts with the sodium flow. To get the velocity field in real units, the conductivity of the sodium was assumed to be $\sigma = 10^{-7}\Omega m$. This is the approximate conductivity of sodium at 110 degrees Celsius, but it was mostly done for mathematic convenience ($\mu_0\sigma = 4\pi$). However, another arbitrarily chosen conductivity would have resulted in the same effective magnetic Reynolds number. It should be noted that the decay time of a pulsed transverse dipole field when the sodium was stationary ($\tau_{textdecay} = \mu_0\sigma L^2 \sim \pi$) agrees with this assumed value of σ (see Figure 5.9).

By running the velocity flow produced by inverting the magnetic data through the predictive routine described in section 2.5 we can determine how close the flow is to self excitation. The pitch of the resolved flow (ratio of poloidal to toroidal flow) can be scanned to see how close to the optimum pitch the current effective velocity flow is.

The results of applying the eigenvalue solver to the velocity flow obtained through the inversion process can be seen in Figure 6.4. The effective magnetic Reynolds number of the flow is 29 and the critical magnetic Reynolds number where a dynamo is expected is Rm=80. The pitch

parameter for the inverted flow was Pitch=0.9 which is very close to the optimum pitch parameter of 0.82. From these results it would seem that with this configuration and flow, the experiment should produce a self excited magnetic field if the speed of the flow was approximately tripled. This rotation rate is beyond the capabilities of the experiment.

6.3 Uncertainty in the Fit

For a t2s2 flow to dynamo, it must have sufficient amplification (Rm) and the correct flow geometry for feedback (pitch). From the velocity inversion results presented above, the effective velocity flow has the near optimal pitch, but it is has only approximately 1/3 the required Rm. We have determined the uncertainty of the fit parameters by further characterization of χ^2_{fit} vs Rm and pitch. Figure 6.5 shows a contour plot of χ^2_{fit} vs Rm and pitch. The shapes of the profiles obtained from the velocity inversion fitting are fixed (w_p,p_p,w_t,p_t) while the magnitude of the flow and the pitch of the flow are varied (a_p and a_t).

The center of the χ^2_{fit} well is at $Rm = 29$,Pitch=0.9 as was found by the inversion process. To determine the confidence in these two parameters we recall from [Bevington and Robinson, 2003] that χ^2 in the vicinity of a minimum can be expressed as:

$$\chi^2 = \frac{a_j - a'_j}{\sigma_{a_j}} + C \tag{6.4}$$

This shows that the variation of χ^2 with any parameter a_j in the vicinity of a minimum with respect to that parameter is parabolic. The constant C is a function of the uncertainties in all other parameters of the fit.

If we take the second derivative of equation (6.4) with respect to parameter a_j, we obtain the uncertainty in the fit with respect to the parameter a_j:

$$\frac{\partial^2 \chi^2}{\partial a_j^2} = \frac{2}{\sigma_{a_j}} \tag{6.5}$$

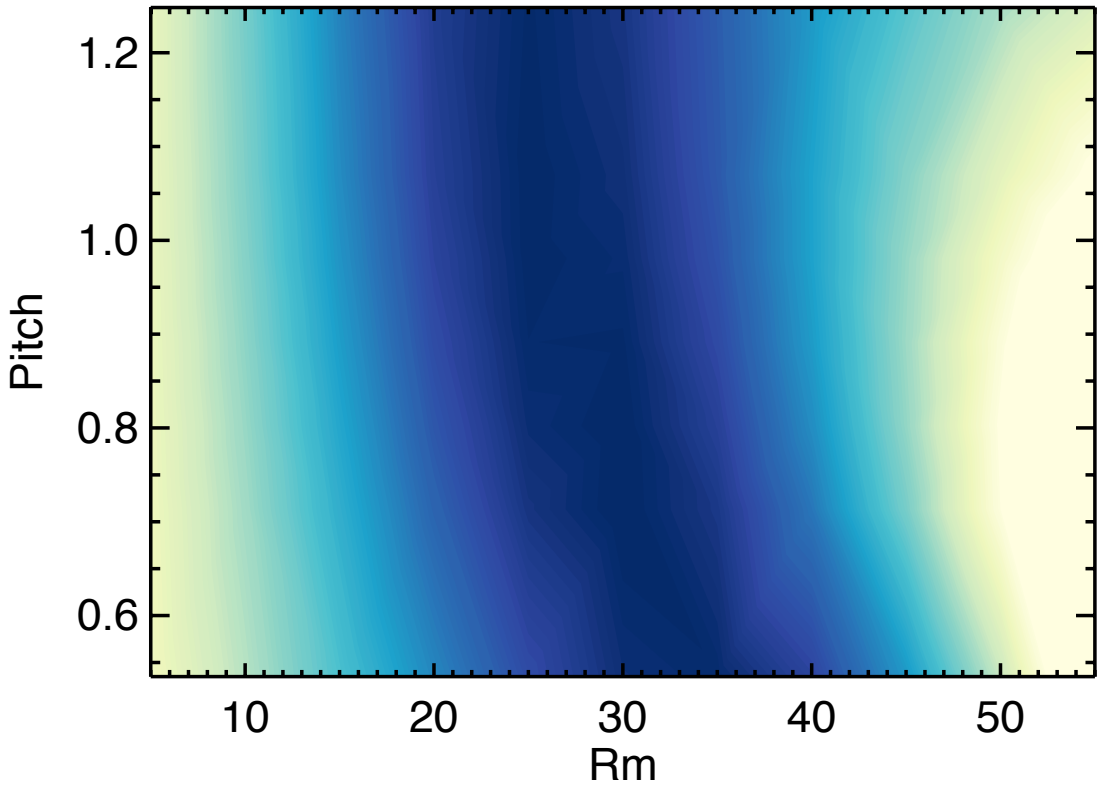

Figure 6.5 A contour plot of χ^2_{fit} is created by keeping the shapes of the profiles, obtained by the inversion routine, fixed and scanning Rm and pitch. The 1000 RPM velocity field from the inversion routine had $Rm = 29$ and Pitch=0.9. The darker color indicates a smaller χ^2_{fit}.

So, by looking at the curvature of the χ^2 function in the region of the minimum, the uncertainty in the parameters Rm and pitch are:

$$\sigma_{Rm} = 2\left(\frac{\partial^2\chi^2}{\partial Rm^2}\right)^{-1} \tag{6.6}$$

$$\sigma_P = 2\left(\frac{\partial^2\chi^2}{\partial P^2}\right)^{-1} \tag{6.7}$$

Figure 6.6 shows a zoomed in view of χ^2_{fit} from Figure 6.5. To evaluate the uncertainties in the fit the curvature of χ^2 must be evaluated near the minimum, where χ^2 is computed without the extra weighting and cost function associated with χ^2_{fit}. This causes the position of the minimum in the contour plot to shift from Figure 6.6 to Figure 6.7. The curvature of χ^2 with respect to the parameters Rm and pitch near the minimum were fit to a parabola are also shown in Figure 6.7. By taking the second derivative of these fit parabolas the uncertainties in Rm and pitch are given by equation (6.6) and were found to be σ_{Rm} = 1.47 and σ_P= 0.09. This results in a 5% error in Rm and 10% error in pitch. It should be noted that there is a correlation between pitch and Rm in the fit. This correlation is indicated by the tilted elliptical contours χ^2_{fit} shown in Figure 6.6. The fact that these two variables used in the fit are correlated implies that their uncertainties are also correlated, further increasing the uncertainties.

6.4 Summary of Inversion Results

Table 6.4 presents a summary of the inversion results for a variety of MDE runs from 200 RPM up to 1600 RPM. Four field configurations were applied at each rotation rate. Most velocity fields were determined from just two data sets ($S_{applied}$=S^0_1,S^1_1).

One notable result is that $Rm_{\text{eff}} \sim 1/3 Rm_{\text{tip}}$. The measured induced fields are best predicted with a velocity field that has a peak speed approximately 1/3 of the speed of the impeller tips. Another important result is that the pitch of the flow does not seem to remain constant. Analysis of the external response mode energies in section 5.2 indicated that turbulence was becoming more prevalent at higher rotation rates. It appears from the velocity inversion results that the increased amount of turbulence is altering the ratio of poloidal to toroidal flow to be less optimal.

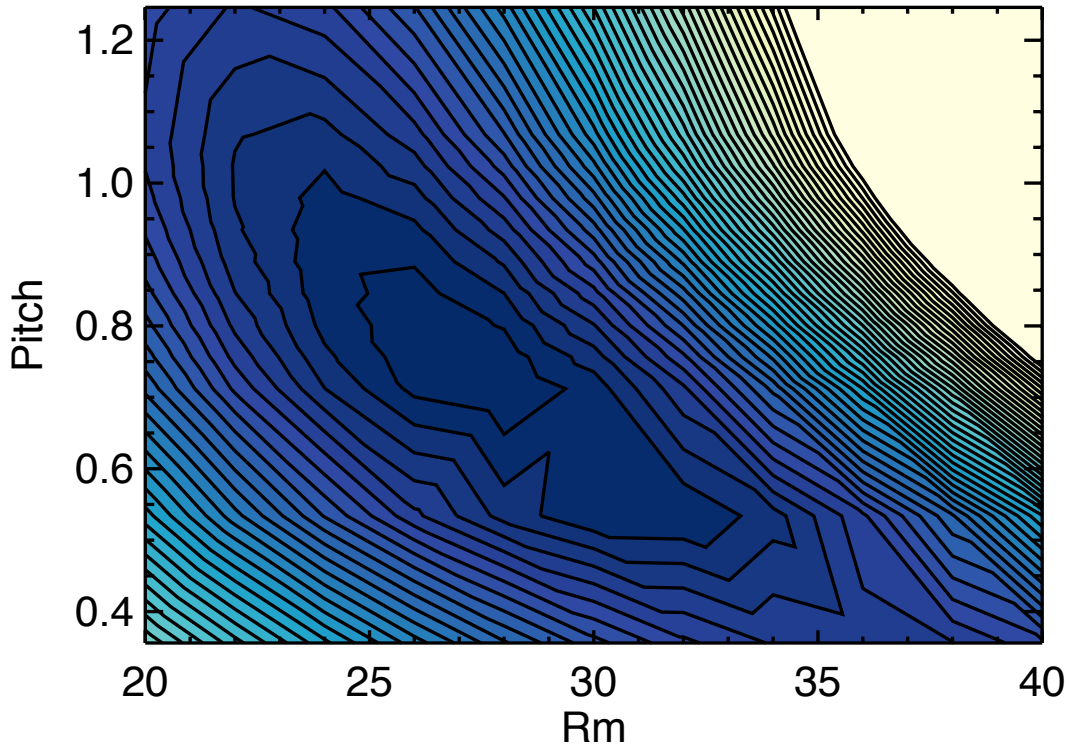

Figure 6.6 A contour plot showing a zoomed in view of χ^2_{fit} from Figure 6.5. The darker the color indicates a smaller χ^2_{fit}. The solid lines are contours on constant χ^2_{fit}.

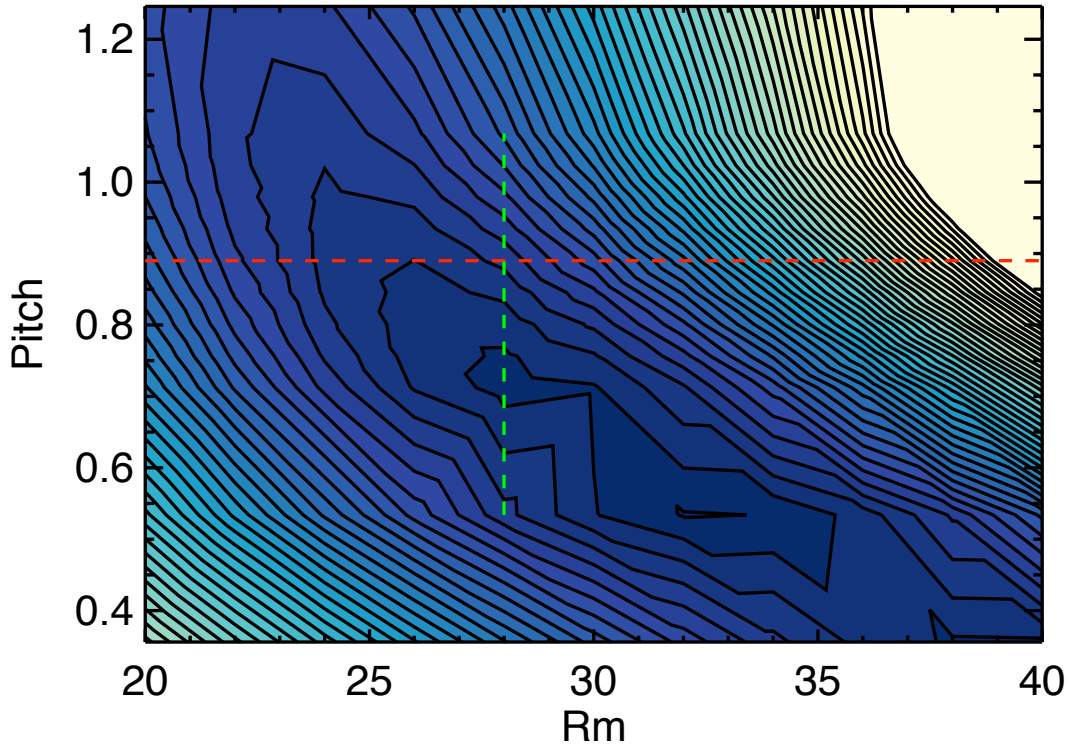

(a) χ^2 with No Cost Function

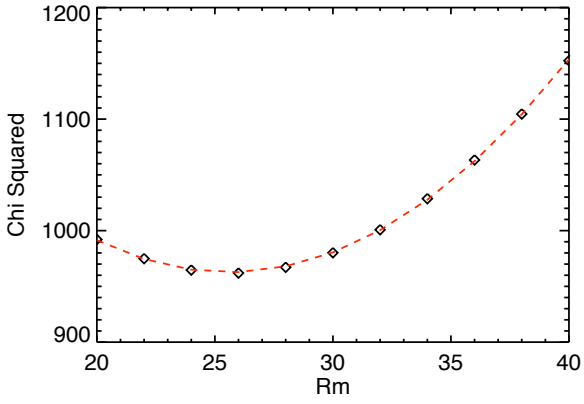

(b) χ^2 vs Rm

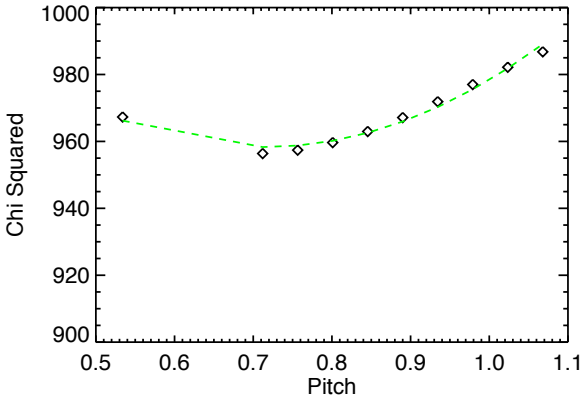

(c) χ^2 vs Pitch

Figure 6.7 (a) A contour plot of χ^2 evaluated without the extra weighting and cost function near the minimum. The uncertainty in the fit parameters Rm and pitch can be determine by evaluating the curvature of χ^2 near the minimum. (b) A parabola is fit to χ^2 vs Rm for a fixed value of pitch. (c) A parabola is fit to χ^2 vs pitch for a fixed value of Rm.

RPM	Rm_{eff}	Energy [J]	Pitch
200	9	106	1.6
400	18	303	0.1
600	24	948	1.5
800	28	919	1.0
1000	29	1229	0.9
1200	34	1584	1.0
1600	41	1735	0.6

Table 6.1 The results of the velocity inversion routine with multiple data sets. All of these datasets were with the equatorial baffle, center disk, and poloidal vanes installed. The vanes were oriented at 45 degrees. This was the best performing flow configuration.

6.5 Implications for a Dynamo

The more constraints added to the flow, the larger turbulent eddies were suppressed and better flux amplification was observed. The internal response magnetic field is best fit with only two spherical harmonics and approximately matches the predicted field. The t2s2 flow at moderate rotation rates, measured through the inversion process, has a near optimum pitch and has an effective magnetic Reynolds number that was approximately 1/3Rm_{tip}. A significant increase Rm is needed. However, it appears that turbulent fluctuations re-emerge at higher rotation rates and modify the pitch of the flow. Simply increasing the impeller rotation rate would not be enough to observe a dynamo in the experiment. Additional constraints must be added to the flow or changing the experiment's size to a larger volume would be needed.

Chapter 7

Conclusions

Many modifications to the Madison Dynamo Experiment have been made. These modifications have reduced the amount of turbulence in the experiment and improved the field amplification. One prevailing question throughout these experiments has been: How close are we to achieving a dynamo? The most definitive way to answer that question is to look at the velocity inversion results. The velocity inversion produces an effective velocity field that is predicted to generate a magnetic response field that matches the experimental measurements. Figure 7.1 shows the sobering reality: The velocity fields from the inversion are predicted to self-excite with $Rm \sim 80$ while they have a current effective $Rm = 28 \pm 1$.

The pitch of the flow is near optimal. To observe a MHD dynamo in a two-vortex flow experiment, the effective magnetic Reynolds number needs to be approximately tripled from what is currently achieved in the Madison Dynamo Experiment without modifying the optimized pitch of the flow.

7.1 Important Results

Although self-excitation has not been observed in the Madison Dynamo Experiment, there have been several important discoveries.

1. A large-scale and diamagnetic current is generated by turbulent EMF in the unconstrained experiment.

2. Constraints added to the flow reduced the detrimental turbulence which was experimentally verified by analyzing response mode energies and motor power requirements.

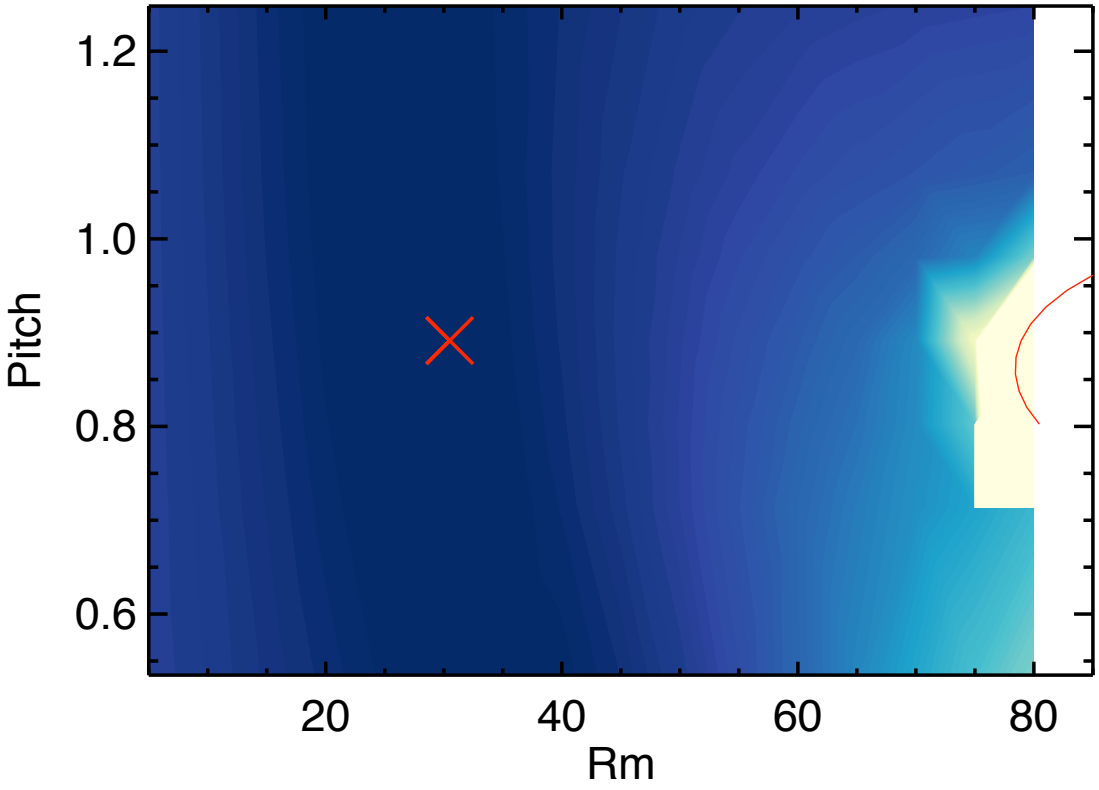

Figure 7.1 χ^2_{fit} is created by keeping the shapes of the profiles (obtained by the inversion routine) fixed while scanning Rm and pitch. The parameters of the flow obtained from the velocity inversion is marked with the X. Also plotted in red is the line of Rm_{crit}. Flows to the right of the red line dynamo.

3. The $\mathbf{V} \times \mathbf{B}$ probe was able to make a direct local measurement of the turbulent EMF and characterize it as mainly a β-effect.

4. The internal induced field generated by constrained flows was measured with 3D probes and was fit to spherical harmonics. The fit approximates laminar predictions.

5. The velocity inversion technique provides an electrodynamic model to explain the induced fields measured in the experiment.

6. The velocity inversion also provides one of the most robust methods for determining the proximity of a subcritical flow to self-excitation. The MDE still requires a significant increase in Rm for a dynamo to be observed.

7.2 Feasibility of Observing a Dynamo in the MDE

The velocity inversion technique in the previous chapter indicates that the effective magnetic Reynolds number of the flows in the experiment are roughly 1/3 of the magnetic Reynolds number computed from the speed of the impeller tip (Rm_{tip}). The experiment is currently producing a mean flow profile that could self-excite if Rm were increased. Below is a discussion of different methods that might be implemented in order to achieve a dynamo in the experiment:

1. Spin it faster: The flow in the experiment is generated with two 75 kW motors with a maximum rotation rate of 1800 RPM. The motors are essentially using maximum power to rotate the the sodium at 1800 RPM. According to the inversion results from data sets near the maximum rotation rate, the effective magnetic Reynolds number of the flow is $Rm_{\text{eff}} = 44$. This flow from the inversion results dynamos with $Rm_{\text{eff}} = 80$. That means that $Rm_{\text{tip}} \sim 3Rm_{\text{eff}} = 240$. However, as mentioned in Section 5.1, the motor power scales as rotation rate cubed. For the impellers to rotate at 2400 RPM ($Rm_{\text{tip}} = 240$), it would require approximately 300 kW of power. This is also making the assumption that Rm_{eff} scales linearly with RPM. It seems from the inversion results that turbulence re-emerges and plays a large role and lowers the effective magnetic Reynolds number at the higher rotation

rates and also might modify the pitch so that a dynamo would not be possible regardless of how fast the impellers were spun.

2. Make it bigger: Similar to the first method, if you cannot make the fluid more conductive or spin it faster, the Rm of the flow can be improved by increasing the scale of the flow. It would require the same amount of power (300 kW) as method 1 to generate a larger, slower flow with $Rm_{\text{eff}} = 240$. However, turbulence would play a smaller role, and the same amount of power would be dissipated into a much larger volume, giving this method a higher success rate. However, increasing the size of the experiment that much would require the entire experiment and all parts to be rebuilt from scratch.

3. Keep adding more constraints to the flow: The performance of the flow, as measured by the transverse dipole gain, significantly improved with the addition of constraints to the flow. With the addition of each new constraint, a larger gain was observed. However, with each new baffle, the amount of improvement decreased. This is due to the fact that the first baffles removed the largest and most detrimental eddies. As more constraints are added, the turbulence is moved to smaller and smaller scales. Adding more constrains would probably improve the performance of the machine, but without more speed or size, a dynamo probably would not be possible.

4. Use ferromagnetic materials: The VKS experiment in Cadarache, France was able to get a two-vortex flow of liquid sodium flow to dynamo, but only after replacing the stainless steel disks with ferromagnetic ones. The magnetic field produced by this experiment was not a transverse dipole but an axial dipole oriented along the rotation axis. Soft iron disks were constructed to be identical to the ones in VKS and were implemented in the Madison Dynamo Experiment. No dynamo was observed in the MDE when the iron disks were spun at 900 rpm, the rotation rate required to observe self-excitation in VKS. However, decay measurements showed an elongation of the decay time, indicating that the experiment was approaching the dynamo threshold. The differences between the geometries of the experiment could explain the differences in the threshold. Unfortunately, the iron disks generate

a much more turbulent and energy intensive flow, so the motors could not rotate faster than 900 RPM. Replacing the current motors with more powerful ones may result in a dynamo. See Appendix B.

One or perhaps a combination of these methods has a decent chance of creating an experiment that will self-excite. To ensure success, the size and power used in the experiment would have to be significantly increased.

7.3 Future of Two-Vortex Dynamo Experiments

Nearly all of the recent experiments constructed to study MHD dynamos in the laboratory have used liquid metals, mainly liquid sodium. There are many benefits to using liquid sodium. First, it is relatively easy to confine in a vessel and to mechanically force to generate a flow. The assumptions of being in the kinematic regime and incompressibility are both extremely valid due to sodium's high density and incompressibility. However, there are also some drawbacks to using liquid sodium. The Prandtl number for liquid sodium is small ($P_m \sim 10^{-4}$) and unchangeable. The fluid Reynolds number is also enormous ($R_e \sim 10^7$). For these reasons, turbulence will always be significant in the flow unless it is in an extremely confined experiment, such as Riga or Karlsruhe.

The Madison Plasma Dynamo Experiment (MPDX) has been constructed to observe a MHD dynamo generated by a two-vortex flow. The experiment is a 3-meter diameter sphere with a hot, unmagnetized plasma. The plasma is confined in the sphere with a multicusp field produced by permanent magnets aligned on the vessel wall. The plasma is spun using biased electrodes located in between the permanent magnets on the wall, creating a torque on the edge of the flow.

By simply changing the ion species, the Prandtl number of the plasma can be changed dramatically. The spinning technique has measured flows at the edge with speeds up to 8 km/s. With the large vessel size, conductive plasma, and fast plasma flow, achieving an Rm_{eff} ten times that of the sodium experiment is easily attainable. The challenge of the plasma dynamo experiment is not in trying to push Rm into the supercritical regime; it is in creating a flow profile conducive to generating a self-excited field.

One aspect of the MDE that set it apart from other liquid metal dynamo experiments was the huge array of internal hall probes and the grid of external probes on the surface. The large amount of diagnostic coverage enabled us to experimentally verify that turbulent eddies had been reduced and allowed for the reconstruction of the effective velocity field in the experiment. This velocity inversion method could be implemented on the Madison Plasma Dynamo Experiment to determine how optimal the flows are and how close it is to self-excitation. The induced magnetic field in the plasma could be measured with hall probes (if thermally protected and not too hot) and pick-up coils. This measured magnetic field could be used in concert with direct local measurements of velocity from methods such as laser induced fluorescence (LIF) and mach probes to determine the effective flow profile. This knowledge could help in tailoring the forcing at the plasma edge to get a more optimum flow.

References

E.N. Parker. Hydromagnetic dynamo models. *Astrophys. J.*, 122:293, 1955.

A. Gailitis, O. Lielausis, S. Dement'ev, E. Platacis, A. Cifersons, G. Gerbeth, T. Gundrum, F. Stefani, M. Christen, H. Hänel, and G. Will. Detection of a flow induced magnetic field eigenmode in the riga dynamo facility. 84(19):4365–4368, 2000. doi: 10.1103/PhysRevLett.84.4365.

A. Gailitis, O. Lielausis, E. Platacis, S. Dement'ev, A. Cifersons, G. Gerbeth, T. Gundrum, F. Stefani, M. Christen, and G. Will. Magnetic field saturation in the riga dynamo experiment. *Phys. Rev. Lett.*, 86:3024, 2001.

R. Stieglitz and U. Mueller. Experimental demonstration of a homogeneous two-scale dynamo. *Phys. Fluids*, 13:561, 2000.

G. O. Roberts. Spatially periodic dynamos. 266(1179):535–558, 1970. URL `http://www.jstor.org/view/00804614/ap000403/00a00010/0?frame=noframe&userID=80683286@wisc.edu/01cc9933961923109e07138f6&dpi=3&config=jstor`.

A. Gailitis, O. Lielausis, E. Platacis, G. Gerbeth, and F. Stefani. Riga dynamo experiment and its theoretical background. 11(5):2838–2843, 2004. doi: 10.1063/1.1666361.

A. Tilgner. Numerical simulation of the onset of dynamo action in an experimental two-scale dynamo. 14(11):4092–4094, 2002. URL `http://link.aip.org/link/?PHF/14/4092/1`.

A. Gailitis, O. Lielausis, E. Platacis, G Gerbeth, and F. Stefani. Colloquium: Laborator experiments on hydromagnetic dynamos. *Reviews of Modern Physics*, 74:973, 2002.

M.L. Dudley and R.W. James. Time-dependent kinematic dynamos with stationary flows. *Proceedings of the Royal Society of London. Series A*, 425:407–429, 1989.

M. D. Nornberg, E. J. Spence, R. D. Kendrick, C. M. Jacobson, and C. B. Forest. Measurements of the magnetic field induced by a turbulent flow of liquid metal. *pp*, 13:055901, 2006a. doi: 10.1063/1.2173614.

D. P. Lathrop, W. L. Shew, and D. R. Sisan. Laboratory experiments on the transition to mhd dynamos. 43(12A):A151–A160, 2001. doi: 10.1088/0741-3335/43/12A/311.

N. L. Peffley, A. B. Cawthorne, and D. P. Lathrop. Toward a self-generating dynamo: The role of turbulence. 61(5):5287–5294, 2000. doi: 10.1103/PhysRevE.61.5287.

P. Odier, J.-F. Pinton, and S. Fauve. Advection of a magnetic field by a turbulent swirling flow. 58 (6):7397–7401, Dec 1998. doi: 10.1103/PhysRevE.58.7397.

R. Monchaux, M. Berhanu, M. Bourgoin, M. Moulin, P. Odier, J.F. Pinton, R. Volk, S. Fauve, N. Mordant, F. Petrelis, A. Chiffaudel, F. Daviund, B. Dubrulle, C. Gasquet, L. Marie, and F. Ravelet. Generation of a magnetic field by dynamo action in a turbulent flow of liquid sodium. *Phys. Rev. Lett.*, 98:044502, 2007.

M. Berhanu, R. Monchaux, S. Fauve, N. Mordant, F. Petrelis, A. Chiffaudel, F. Daviund, M. Bourgoin, M. Moulin, P. Odier, J.F. Pinton, R. Volk, S. Fauve, N. Mordant, F. Petrelis, A. Chiffaudel, F. Daviund, B. Dubrulle, C. Gasquet, L. Marie, and F. Ravelet. Magnetic field reversals in an experimental turbulent dynamo. *Europhysics Letters*, 77:59001, 2007.

A. Giesecke, Nore C., F. Plunian, R. Laguerre, A. Ribeiro, F. Stefani, G. Gerbeth, J. Leorat, and J.L. Guermond. Generation of axisymmetric modes in cylindrical kinematic mean-field dynamos of vks type. *Geophys Astro Fluid Dynamics*, 104:249–271, 2010.

M. D. Nornberg, E. J. Spence, R. D. Kendrick, C. M. Jacobson, and C. B. Forest. Intermittent excitation of a magnetic eigenmode in a turbulent flow of liquid sodium. *prl*, 2006b. (in press).

E. J. Spence, M. D. Nornberg, C. M. Jacobson, R. D. Kendrick, and C. B. Forest. Observation of a turbulence-induced large scale magnetic field. *prl*, 96(5):055002, 2006. doi: 10.1103/PhysRevLett.96.055002.

T. G. Cowling. The magnetic field of sunspots. *mnras*, 94:39–48, nov 1933. URL http://adsabs.harvard.edu/cgi-bin/nph-bib_query?bibcode=1933MNRAS..94...39C&db_key=AST.

E.J. Spence, M.D. Nornberg, C.M. Jacobson, C.A. Parada, N.Z. Taylor, R.D. Kendrick, and C.B. Forest. Turbulent diamagnetism in flowing liquid sodium. *Phys. Rev. Lett.*, 98:164503, 2007.

E.J. Kaplan, M.M. Clark, M.D. Nornberg, K. Rahbarnia, A.M. Rasmus, N.Z. Taylor, , C.B. Forest, and E.J. Spence. Reducing global turbulent resistivity by eliminating large eddies in a spherical liquid-sodium experiment. *Phys. Rev. Lett.*, 106:254502, 2011.

K. Rahbarnia. Direct observation of the turbulent emf and transport of magnetic field in a liquid sodium experiment. *Astrophys. J.*, 759:80, 2012.

E. Bullard and H. Gellman. Homogeneous dynamos and terrerstrial magnetism. *Philosophical Transactions of the Royal Society of London. Series A*, 247:213–278, 1954.

J. A. Gaunt. The triplets of helium. 122(790):513–532, 1929.

W. Elsasser. Induction effects in terrestrial magnetism Part I. theory. 69(3–4):106–116, 1946. URL http://link.aps.org/abstract/PR/v69/p106.

C. B. Forest, R. A. Bayliss, R. D. Kendrick, M. D. Nornberg, R. O'Connell, and E. J. Spence. Hydrodynamic and numerical modeling of a spherical homogeneous dynamo experiment. *mhd*, 38 (1/2):107–120, 2002. URL http://mhd.sal.lv/contents/2002/1/MG.38.1.9.R.html?his=0ac539656864c4f0960dafabc98b4e69.

R. O'Connell, R. Kendrick, M. Nornberg, E. Spence, A. Bayliss, and C. Forest. On the possibility of an homogeneous MHD dynamo in the laboratory. In P. Chossat, D. Ambruster, and I. Oprea,

editors, *Dynamo and Dynamics, a Mathematical Challenge*, volume 26 of *NATO Science Series II, Mathematics, Physics and Chemistry*, pages 59–66, Dordrecht, 2000. NATO Science Programme, Kluwer Academic Publishers.

K. Krause and K. H. Rädler. *Mean-field Magnetohydrodynamics and Dynamo Theory*. Pergammon Press, New York, 1980.

M. D. Nornberg. *The role of MHD turbulence in magnetic self-excitation: a study of the Madison Dynamo Experiment*. PhD thesis, University of Wisconsin-Madison, 2006.

E. J. Spence. *Experimental observation of fluctuation-driven mean magnetic fields in the Madison Dynamo Experiment*. PhD thesis, University of Wisconsin-Madison, 2006.

E. J. Kaplan. *The role lof large eddy fluctuations in the magnetic dynamics of the madison dynamo experiment*. PhD thesis, University of Wisconsin-Madison, 2012.

Robert C. Weast. *CRC Handbook of Chemistry and Physics*. CRC Press, Inc., Boca Raton, FL, sixty-sixth edition, 1986.

E. Shpil'rain, K. A. Yakimovich, V. A. Fomin, S. N. Skovorodjko, and A. G. Mozgovoi. *Dynamic and Kinematic Viscosity of Liquid Alkali Metals*. International Union of Pure and Applied Chemistry Chemical Data Series. Blackwell Science Publications, Oxford, 1985.

J. Baumgartl, A. Hubert, and G. Müller. The use of magnetohydrodynamic effects to investigate fluid flow in electrically conducting melts. 5(12):3280–3289, 1993.

F. Stefani and G. Gerbeth. Velocity reconstruction in conducting fluids from magnetic field and electric potential measurements. 15(3):771–786, 1999.

J.A. Nelder and R. Mead. A simplex method for function minimization. *The computer Journal*, 7 (4):308–313, 1965.

W.H. Press. *Numerical Recipes in C: The Art of Scientific Computing*. Cambridge University Press, 2 edition, 1992.

F. Stefani and G. Gerbeth. On the uniqueness of velocity reconstruction in conducting fluids from measurements of induced electromagnetic fields. 16(1):1–9, 2000.

P.R. Bevington and D.K. Robinson. *Data Reduction and Error Analysis for the Physical Sciences*. McGraw-Hill, 3 edition, 2003.

APPENDIX
Simple velocity inversion technique

In an attempt to infer what the velocity profiles are in the sodium a simple inversion technique was developed. This technique does not try to fit a velocity profile and run it through the linear predictive code like what was described in 6.2. Instead this technique takes the structure of the largest modes measured on the experiment (ℓ=1,m=0) and truncates the the magnetic induction equations (2.13) and (2.14) so that the $s_2^0(r)$ and $t_s^0(r)$ flow profiles can be solved for analytically.

Recall from chapter 2: The time dependence of response modes is affected by a dissipation term plus an infinite set of coupled advection terms:

$$\frac{\partial S_\gamma}{\partial t} = \nabla_{l_\gamma}^2 S_\gamma + \frac{Rm}{r^2}\sum_{\alpha,\beta}[(s_\alpha S_\beta S_\gamma) + (t_\alpha S_\beta S_\gamma) + (s_\alpha T_\beta S_\gamma) + (t_\alpha T_\beta S_\gamma)] \tag{A.1}$$

$$\frac{\partial T_\gamma}{\partial t} = \nabla_{l_\gamma}^2 T_\gamma + \frac{Rm}{r^2}\sum_{\alpha,\beta}[(s_\alpha S_\beta T_\gamma) + (t_\alpha S_\beta T_\gamma) + (s_\alpha T_\beta T_\gamma) + (t_\alpha T_\beta T_\gamma)] \tag{A.2}$$

where: $\nabla_{\ell_\gamma}^2 = \frac{\partial^2}{\partial r^2} - \frac{\ell_\gamma(\ell_\gamma+1)}{r^2}$

The two important interaction terms are given below:

$$(s_\alpha S_\beta S_\gamma) = \frac{K_{\alpha\beta\gamma}}{N_\gamma}\left[p_\alpha c_\alpha s_\alpha \frac{\partial S_\beta}{\partial r} - p_\beta c_\beta \frac{\partial s_\alpha}{\partial r} S_\beta\right]$$

$$(t_\alpha S_\beta T_\gamma) = -\frac{K_{\alpha\beta\gamma}}{N_\gamma}\left[(p_\gamma c_\gamma + p_\beta c_\beta) t_\alpha \frac{\partial S_\beta}{\partial r} + p_\beta c_\beta \left(\frac{\partial t_\alpha}{\partial r} - \frac{2t_\alpha}{r}\right) S_\beta\right]$$

Where:

$$K_{\alpha\beta\gamma} = \int_0^{2\pi}\int_0^{\pi} Y_\alpha(\theta,\phi) Y_\beta(\theta,\phi) Y_\gamma(\theta,\phi) \sin\theta \mathrm{d}\theta \mathrm{d}\phi$$

and $c_\alpha = (p_\alpha - p_\beta - p_\gamma)/2$ and $N_\alpha = p_\alpha = \ell_\alpha(\ell_\alpha + 1)$

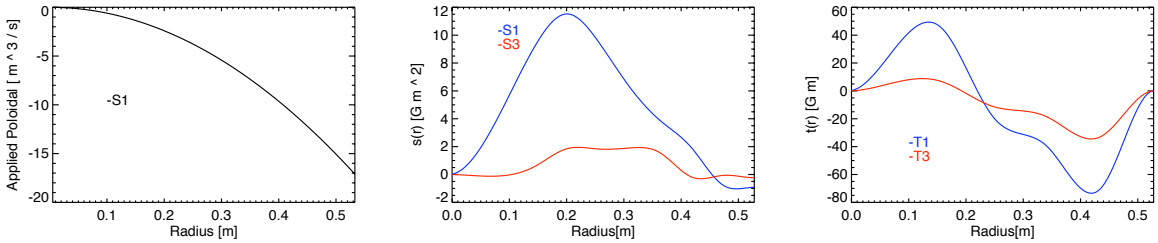

(a) Applied poloidal mode (b) Poloidal response modes (c) Toroidal response modes

Figure A.1 (a)The radial profile of the applied S_1^1 mode. (b) the poloidal radial profiles fit to the data in the experiment. (c) the toroidal radial profiles fit to the data in the experiment

By eliminating all but the ℓ_γ=1 mode in the interaction terms the radial profiles for the poloidal and toridal field can be solved for

$$Rms_2'(r') = \frac{\sqrt{5\pi}}{3S_1^{0\prime}(r')} \int_0^{r'} \left(2S_1^{0\prime}(r') - r'^2 \frac{\partial^2 S_1^{0\prime}(r')}{\partial r'^2} \right) \mathrm{d}r' \tag{A.3}$$

$$Rmt_2'(r') = \frac{r'^2}{S_1^{0\prime}(r')^2} \int_0^{r'} S_1^{0\prime}(r') \left[\frac{\sqrt{5\pi}}{3} \left(\frac{2T_1^{0\prime}(r')}{r'^2} - \frac{\partial^2 T_1^{0\prime}(r')}{\partial r'^2} \right) - Rms_2'(r') \frac{\partial}{\partial r'} \left(\frac{T_1^{0\prime}(r')}{r'^2} \right) \right] \mathrm{d}r' \tag{A.4}$$

By taking the largest and lowest order (S_1^0 and T_1^0) measured applied and response modes from Figure A.1 and plugging them into the equations above you can solve for the radial flow profiles shown in figure A.2.

Unfortunately this technique results in a velocity field that approximates the actual field but does not reproduced known test flows. Ignoring the measured ℓ=3 modes removes necessary information in determining the velocity profile. However, this method does give a good approximation for the magnitude of the flows.

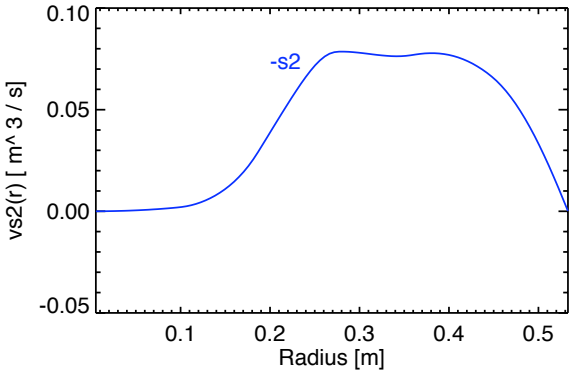

(a) Poloidal Radial Profile

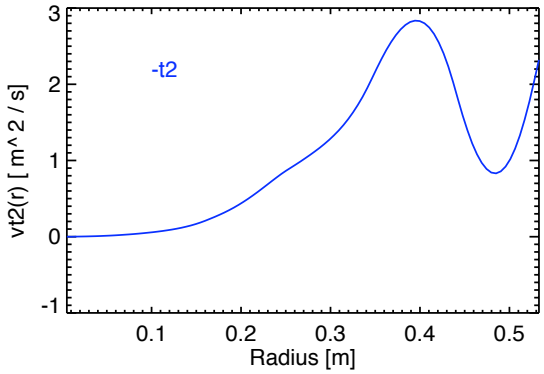

(b) Toroidal Radial Profile

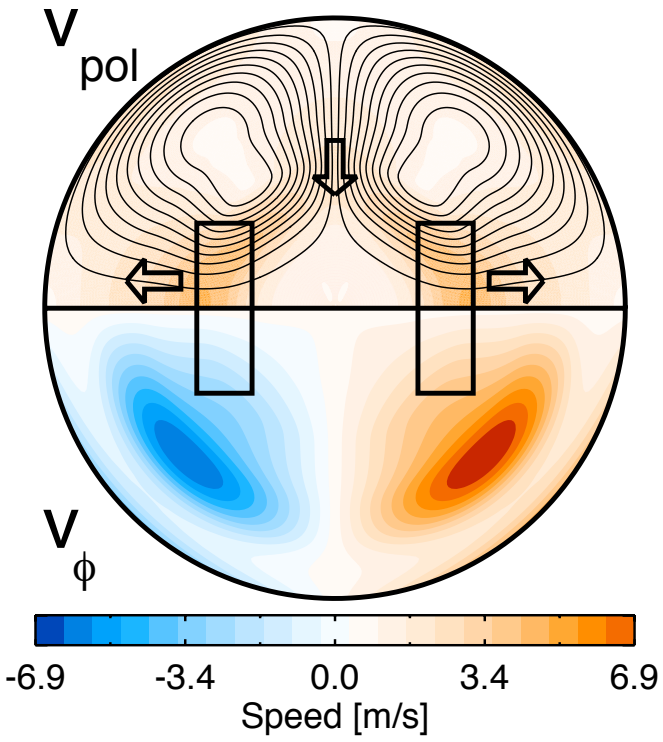

(c) Velocity Contour

Figure A.2 a) The poloidal and (b) toroidal radial profiles obtained from the simplified velocity inversion routine. (c) The corresponding contour plot of the velocity field.

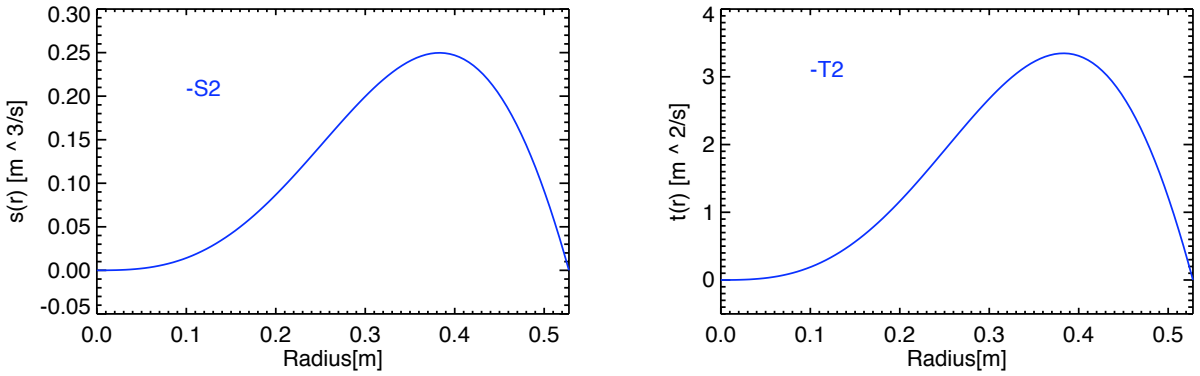

(a) Poloidal Radial Profile

(b) Toroidal Radial Profile

Figure A.3 a) The poloidal and (b) toroidal radial profiles that describe the ideal Dudley and James flow.

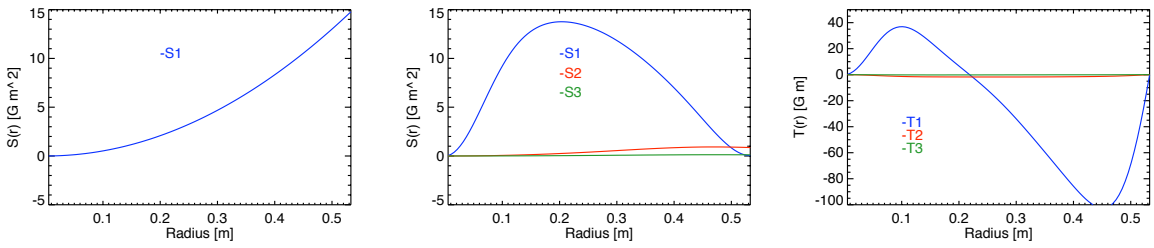

(a) Applied Field poloidal Radial Profile

(b) Response Field Poloidal Radial Profile

(c) Response Field Toroidal Radial Profile

Figure A.4 a) The poloidal and (b) toroidal radial profiles that describe the ideal Dudley and James flow.

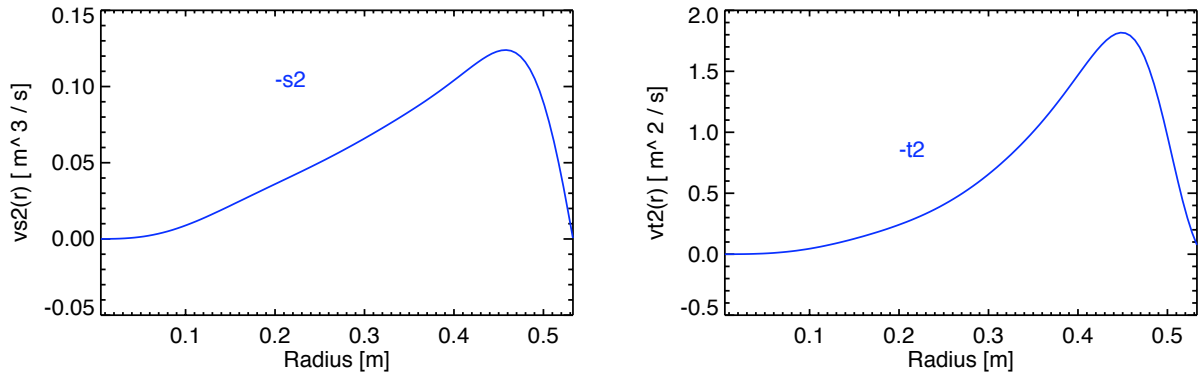

(a) Poloidal Radial Profile

(b) Toroidal Radial Profile

Figure A.5 a) The poloidal and (b) toroidal radial profiles that are solved for by taking the magnetic profiles produced by the test case: the ideal Dudley and James flow.

APPENDIX
Use of Ferromagnetic Material in the Madison Dynamo Experiment

The Von Karman Sodium Experiment (VKS) in Cadarache, France is a cylindrical vessel that drives a turbulent flow with two disks located at each end of the cylinder. This section will describe efforts to measure the effect of placing iron close to the experiment and Installing soft iron disks, identical to those used in VKS, in MDE.

B.1 Iron mass in proximity to sphere

One experimental campaign done in the Madison Dynamo Experiment (MDE) was to observe the effect of a having a large ferromagnetic mass close to the vessel when it was in operation. A large iron plate was placed as close as possible to to the midplane of the vessel. The reasoning behind this experiment was that the desired transverse-dipole response mode produced by the flow would lock on and be amplified by the mass of iron. The iron, with its higher magnetic permeability should work as a passive amplifier of the transverse applied and response mode.

Figure B.1 shows how the iron plate installed next to the vessel. Lifting eyes were placed in the iron plate and it was hoisted to hang next to one of the transverse coils. Another lifting strap tightened the plate to be centered exactly in the center of the transverse coil. The presence of the multiple oiling cooling lines for the sphere heating/cooling system prevented the iron from being placed any closer.

In Section 5.3 the gain in the transverse dipole was used as a major indicator of the performance of the flow. A higher gain was measured as more constraints were added to the flow. One of the observations was the gain in the transverse dipole gain improved with rotation rate. It was also

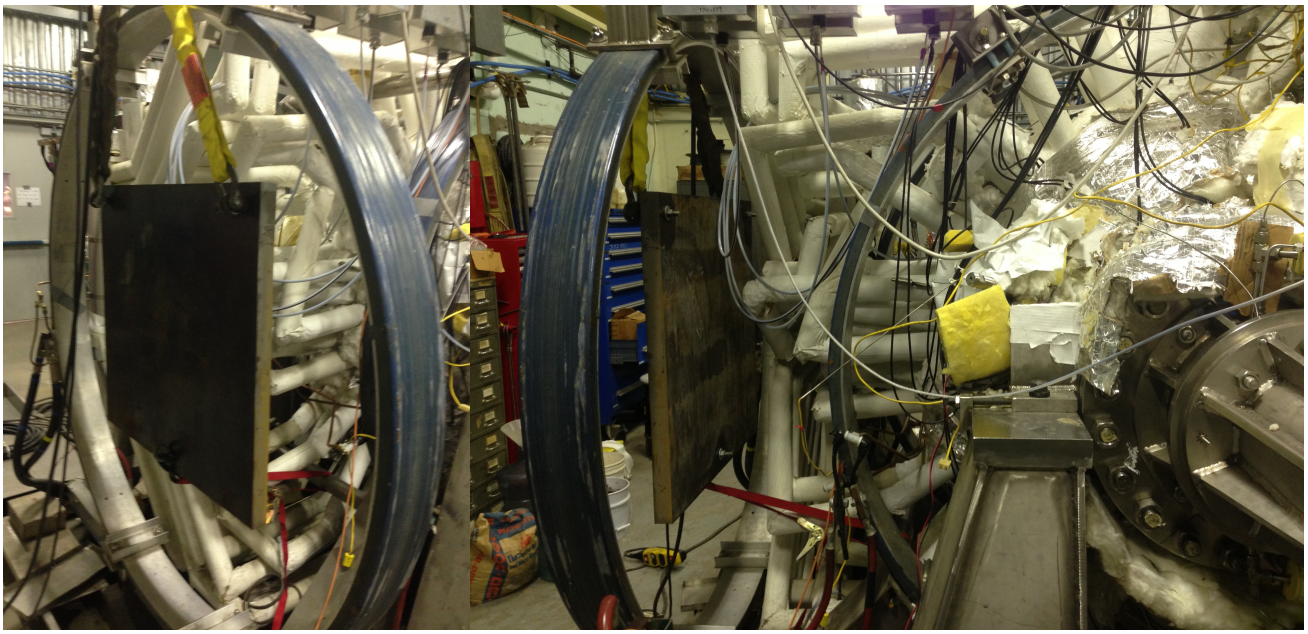

Figure B.1 Pictures of the large ferromagnetic iron plate that was temporarily installed next to the experiment. The large iron mass was oriented to align with the transverse dipole applied mode to amplify the response

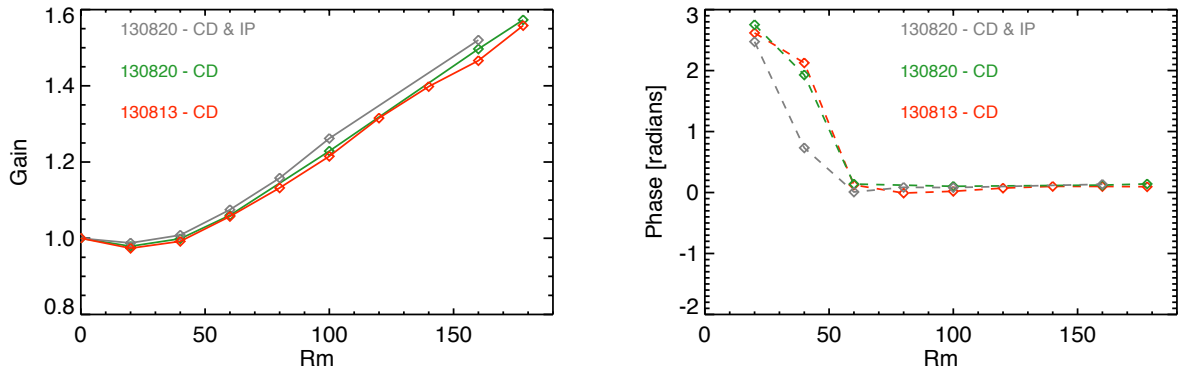

(a) S_1^{1c} mode gain

(b) S_1^{1c} phase

Figure B.2 (a)The gain of the S_1^{1c} mode vs Rm for three different experimental runs: 130813=eq baffle, vanes at 45 degrees and center disk, 130820=eq baffle, vanes at 45 degrees and center disk with two different Rm scans; one without the iron plate, one with the iron plate. (b) the corresponding phase ($\Delta\phi$)of the response S_1^1 with the applied mode.

found that the response transverse dipole mode was originally misaligned with the applied field and then rotated and co-aligned with the applied mode at higher RPM.

In figure B.2 we illustrate the effect of the iron plate by showing the gain and the phase of the transverse mode plotted vs rotation rate compared to an experimental campaign with the same baffle configuration without the plate. The transverse response mode at low RPM was initially not aligned with the applied field. The addition of the iron plate caused the mode to ”lock-in” to the applied field at lower RPM. The gain was also improved slightly with the iron plate. This experimental campaign was the largest gain measured in the Madison Dynamo Experiment. Although the results were not spectacular, they do indicated that the performance of the experiment could be improved upon if a large iron ”yoke” were oriented around the experiment close to the vessel wall to help lock-in and amplify the desired transverse dipole response mode.

B.2 Use of Iron Disks to Drive the Flow

Iron disks of the same geometry as those used in the VKS experiment were installed in the Madison Dynamo Experiment. Figure B.3 shows the geometry of the disks before being installed

in the MDE. Extra spacers were placed on the drive shafts so that the spacing between the two disks was comparable to the spacing in the VKS experiment. In the section B.4 it was shown that for different baffle configurations the amount of power required to rotate the impellers at a fixed speed was correlated to the amount of turbulent energy in the flow. Figure B.4 shows that the flow driven with the disks requires a lot more power than the flow with the impellers. Figures B.5 and B.6 shows the response mode energies for the flows produced with the iron disks and flows produced with the impellers. All three of these plots indicate that the flows driven with the iron disks are much more turbulent than those driven with the impellers.

Figure B.3 Pictures of the ferromagnetic iron disks, identical to the ones that were used in the VSK experiment, installed in the madison dynamo experiment.

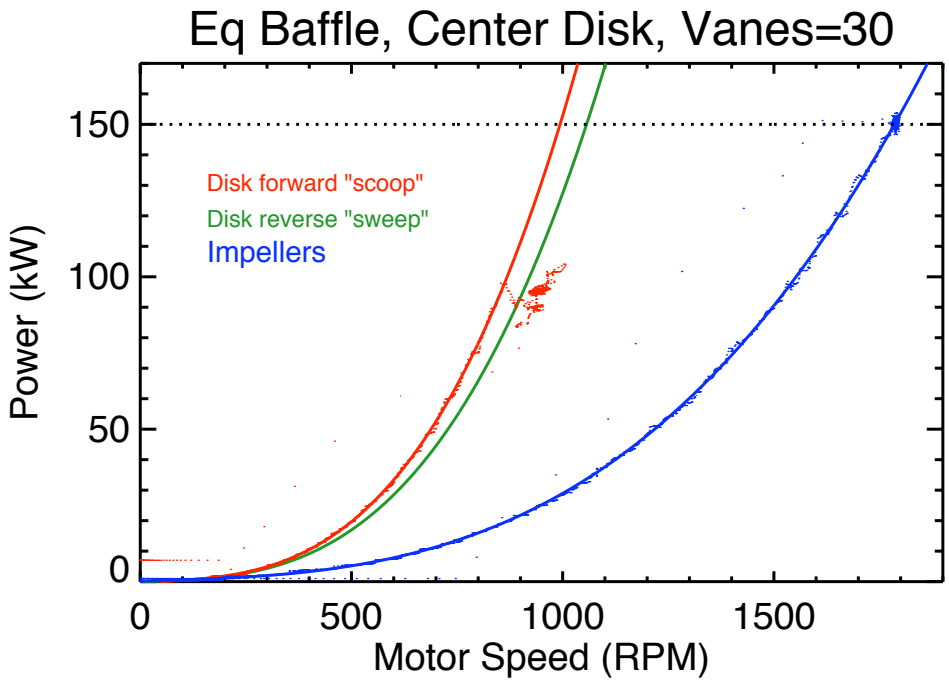

Figure B.4 The total power required to rotate the impeller and disks at a certain speeds. The curved vanes on the disk either scoop or sweep the flow depending on the rotation direction.

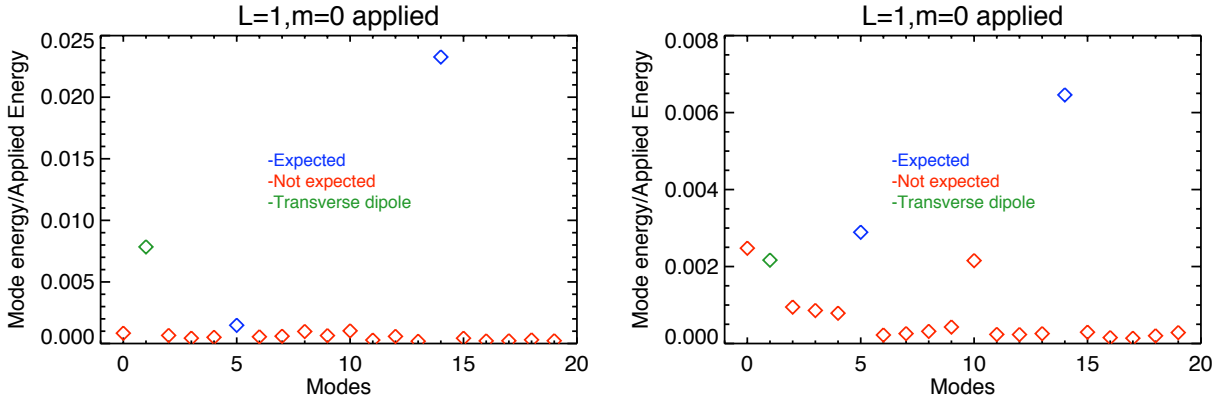

(a) 1000 rpm impeller flow, all constraints

(b) 500 rpm disk flow(sweeping), all constraints

Figure B.5 The energy in the response modes partitioned into expected(blue), unexpected(red), and unexplained S_1^1(green) for a two-vortex flow with an axial dipole applied field. (a) 1000 rpm flow generated with the impellers with the equatorial baffle, center disk, and poloidal vanes at 30 degrees (b) 500 rpm flow generated with the iron disks in the sweeping direction with the equatorial baffle, center disk, and poloidal vanes at 30 degrees

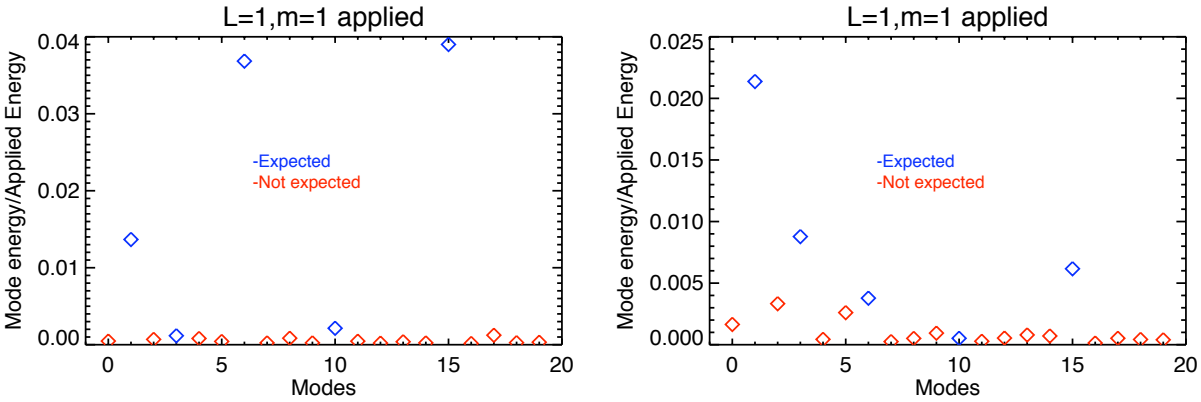

(a) 1000 rpm impeller flow, all constraints

(b) 500 rpm disk flow(sweeping), all constraints

Figure B.6 The energy in the response modes partitioned into expected(blue), unexpected(red) for a two-vortex flow with a transverse dipole applied field (a) 1000 rpm flow generated with the impellers with the equatorial baffle, center disk, and poloidal vanes at 30 degrees (b) 500 rpm flow generated with the iron disks in the sweeping direction with the equatorial baffle, center disk, and poloidal vanes at 30 degrees